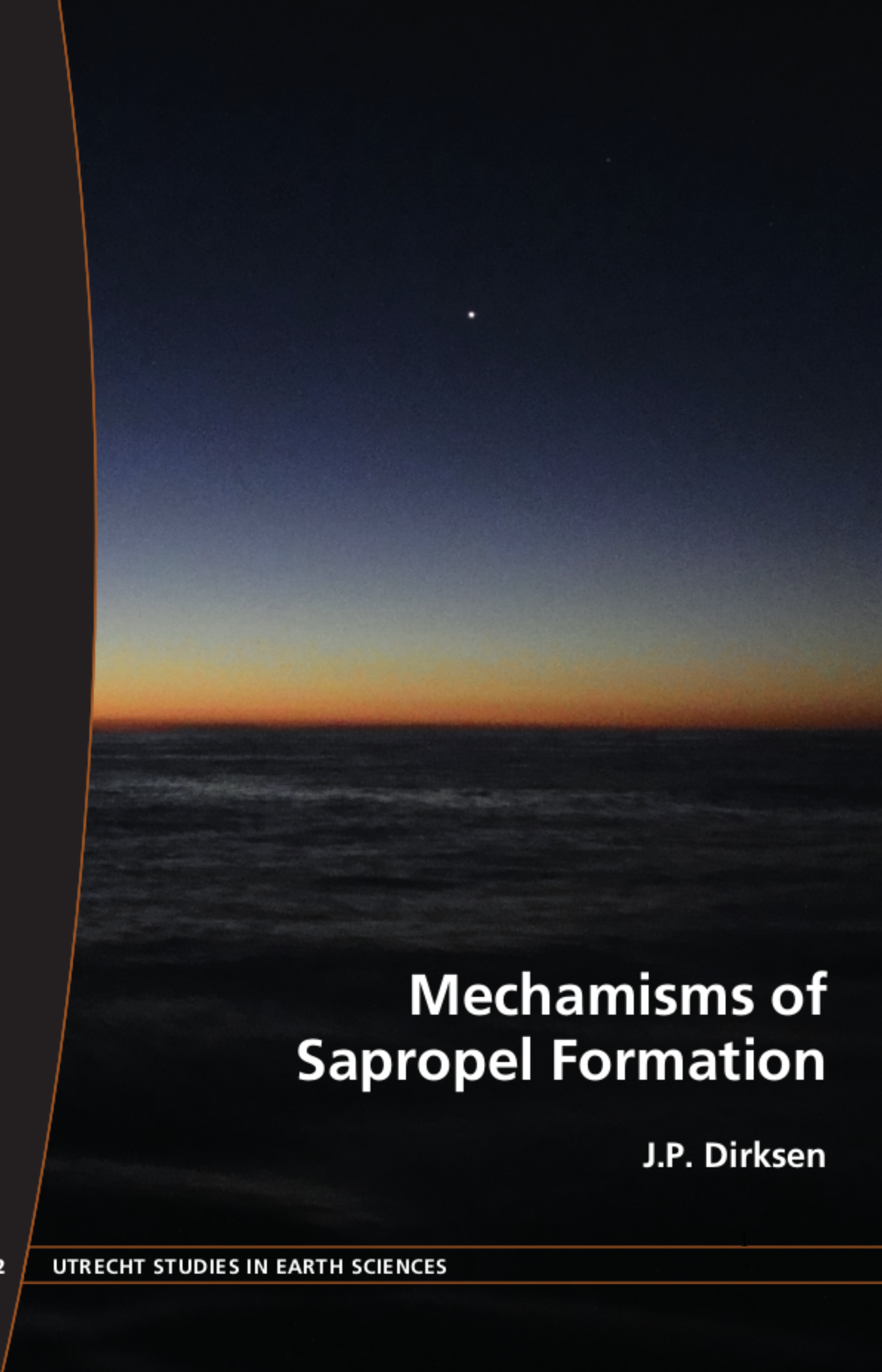

Mechamisms of Sapropel Formation

J.P. Dirksen

282 UTRECHT STUDIES IN EARTH SCIENCES

Cover: Sunrise on the Eastern Mediterranean Sea, near Cyprus, taken from the RV Pelagia in early 2016, at the location where the sediment core used in this thesis was collected. Venus, clearly visible in the centre, affects Earth's precession cycle and thereby sapropel formation.

Mechanisms of Sapropel Formation
ISBN 978-90-6266-652-2
USES 282
DOI https://doi.org/10.33540/1805
Cover and thesis layout: Margot Stoete and Jan Pieter Dirksen
Printed by: Ipskamp Printing, Enschede
All photos: Jan Pieter Dirksen

Mechanisms of Sapropel Formation

Mechanismen van Sapropelvorming
(Met een samenvatting in het Nederlands)

Proefschrift

ter verkrijging van de graad van doctor aan de
Universiteit Utrecht
op gezag van de
rector magnificus, prof.dr. H.R.B.M. Kummeling,
ingevolge het besluit van het college voor promoties
in het openbaar te verdedigen op

donderdag 6 juli 2023 des middags te 12.15 uur

door

Jan Pieter Dirksen

geboren op 18 februari 1993
te Valkenswaard

Promotor
Prof. dr. W. Krijgsman

Copromotor
Dr. P.T. Meijer

Beoordelingscommissie
Dr. ir. D.V. Palcu
Prof. dr. G.J. Reichart
Prof. dr. E.J. Rohling
Prof. F.J. Sierro
Prof. dr. ir. C.P. Slomp

Dit proefschrift werd (mede) mogelijk gemaakt met financiële steun van The Netherlands Research Centre for Integrated Solid Earth Science (ISES 2017-UU-23), the Netherlands Earth System Science Centre (NESSC), met financiële steun van het Ministerie van Onderwijs, Cultuur en Wetenschap (OCW) (Grant number 024.002.001) en het SCANALOGUE-project (ALWOP.2015.113) door de Nederlandse Organisatie voor Wetenschappelijk Onderzoek (NWO).

Imagine that you are those waves. Now nothing can disturb you.

Contents

Samenvatting

De geologische geschiedenis van de Middellandse Zee kent drastische wendingen waarbij het zeeleven in het diepe water massaal sterft, om pas duizenden jaren later weer op te bloeien. Deze cyclus laat zijn sporen na op de zeebodem. Op de zeebodem verzamelt zich langzaam sediment. Als je hierin boort en het omhoog haalt, kun je dus terug in de tijd kijken. De periodes zonder bodemleven zijn terug te vinden als zwarte lagen die rijk zijn in organisch materiaal, zogenaamde **sapropelen**. Deze lagen komen op regelmatige afstand voor. In deze thesis bestuderen we de natuurkundige en chemische processen die hiervoor verantwoordelijk zijn.

Als er vandaag de dag een vis, of ander organisme, sterft en op de oceaanbodem beland, dan zul je daar al heel snel niks meer van terugvinden: het wordt ontbonden en soms opgegeten. Waarom was dit in het verleden soms anders en werden er sapropelen gevormd? Dit komt doordat er in deze periodes een heel bijzondere omstandigheid was: er was *geen zuurstof in het bodemwater*. Met andere woorden: al het organisch materiaal dat op de bodem viel bleef bewaard. Dit verklaart de zwarte kleur. Het valt op dat de zwarte lagen door scherpe overgangen begrensd zijn. Dit duidt erop dat er grote veranderingen heel snel hebben plaatsgevonden. Dit soort overgangen zijn bij uitstek interessant, niet alleen voor de Middellandse Zee, maar ook omdat ze inzicht geven in wereldwijde oceaan- en klimaatmechanismes die ook vandaag de dag spelen.

De zuurstof in het diepe water wordt aangevoerd vanaf het oppervlak. Er zijn drie processen die het zuurstoftransport aansturen: ten eerste neemt door verdamping het zoutgehalte van het oppervlaktewater toe en, ten tweede, koelt het water tijdens winterstormen af. Beide processen zorgen ervoor dat de dichtheid van het water toeneemt, waardoor het naar de bodem zinkt. Ten slotte leveren rivieren zoet water, met een lage dichtheid, aan. Dit vertraagd de circulatie juist. Deze drie processen zorgden er tijdens sapropel vorming samen voor dat er geen zuurstof meer naar het diepe water werd getransporteerd. Maar wat veroorzaakt het cyclische gedrag van sapropel vorming?

De Middellandse Zee is bijna helemaal geïsoleerd, er is alleen uitwisseling met de oceaan door de smalle straat van Gibraltar. Hierdoor is de zee extra gevoelig voor regionale klimaatverandering. De rivieruitstroom, van met name de Nijl, maakt constant een cyclus door van 21 duizend jaar. Dit hangt samen met de stand van de aardas en wordt gezien als de belangrijkste factor in sapropelvorming. Ook binnen de sapropel zijn meerdere scherpe overgangen te vinden en het einde abrupt kan zijn. Het is opmerkelijk dat deze snelle overgangen, van enkele jaren, door de trage variatie van de stand van de aardas veroorzaakt zijn.

De Middellandse Zee laat veel van de processen zien die ook van groot belang zijn voor de wereldwijde oceaancirculatie, zoals diepwatervorming. Dit maakt de Middellandse Zee een ideaal modelsysteem om het effect van klimaatverandering op oceaancirculatie te bestuderen. Sapropel formatie is al veel bestudeerd, maar wat er precies tijdens de snelle overgangen gebeurt en hoe de circulatie nou echt verandert, is onduidelijk. Het is ons gelukt om een wiskundig model te bouwen dat processen die hierboven zijn beschreven ondervangt en een verklaring geeft voor sapropel vorming en hun scherpe begrenzing. Het unieke van ons model is dat het de processen gedurende de hele cyclus van 21 duizend jaar beschrijft, in fijne tijdstappen van een jaar. Daar bovenop is de rekentijd kort, minder dan een seconde. Het model verklaart hoe relatief langzame klimaatverandering een abrupte en drastische verandering in de oceaancirculatie kan veroorzaken. Ons model is, met andere parameters, ook toe te passen op andere zeeën. In het laatste hoofdstuk van dit proefschrift passen we het toe op de Zwarte Zee, waar we er ook een biologisch en chemisch model toevoegen. Onze bevindingen zijn gepubliceerd in drie artikelen en in dit proefschrift.

Summary

In paleoceanography, physical and chemical processes of the oceans are studied throughout geological history. The sediments that constantly accumulate on the sea floor reflect the oceanographic conditions at the time of deposition. These geological records can be collected using sediment cores, providing a window into the past. In January 2016, sediment core 64PE406-E1 was collected in the eastern Mediterranean Sea, near Cyprus. This core not only provided an excellent archive of oceanographic changes over the past two hundred thousand years, it also inspired the research presented in this thesis on the Mediterranean and Black Sea. The geological record of the Mediterranean sea contains alternating dark organic rich layers, so-called **sapropels**, and gray mud layers. We study the oceanographic mechanisms that cause sapropel formation in the Mediterranean Sea, as well as organic rich deposits in the Black Sea. The key to sapropel formation is water circulation and organic matter. When the circulation slows down and sufficient organic matter is produced, the bottom water becomes anoxic, i.e. lacking oxygen. Any organic matter that sinks to the sea floor is preserved, hence the dark colour. Due to the lack of oxygen, life does not disturb the sediments on the sea floor. Consequently, these sediments provide a remarkably fine structure of layers and a high resolution record of past oceanographic conditions.

In the Mediterranean Sea, sapropels are found at a regular time interval of typically 21 thousand years, equal to the period of Earth's precession. Indeed, Earth's motion is an important drivers of climate change on geological timescales. In particular, Earth's precession impacts the monsoon intensity, which in turn determines the Nile discharge. Earth's precession therefore affects sapropel formation. Venus, seen in the center of the front cover, as well as other planets, impact precession.

The Black Sea was cut-off from the Mediterranean during the last ice age, since the sea level was not high enough for water to pass the shallow Bosporus strait. At the end of the ice age, the sea level increased, allowing inflow from the Mediterranean Sea. The in-flowing water sank to the deep parts of the basin, supplying extra nutrients into the Black Sea. Consequently, production of organic matter increased, causing the formation of an organic rich layer.

Previous studies on geological records mostly consider a steady state system, in equilibrium with an external forcing. Such models cannot describe transient behaviour, with varying boundary conditions. In contrast, we consider the Mediterranean and the Black Sea as dynamic systems. The mechanisms responsible for this variability are described by a transient box model that captures oceanic circulation. In such a model the Mediterranean and Black Sea are divided in a number of boxes, having uniform properties. A box represents an important water mass, such as the deep water of the Black Sea. The atmosphere and the rivers are also represented as boxes. Boxes may interact by exchanging salt, heat, oxygen and nutrients. We find that it is possible to describe the formation of organic rich deposits in the Mediterranean and Black Sea using only a small number of boxes. The great advantage of

this approach is that it gives insight into the fundamental processes. The dynamic range is unique to this model: it simultaneously describes short term (1 year) and long term (> 100 kyr) processes, while requiring less than a second to run on a regular computer. When studying transient mechanisms, the interactions between the different features of the system are of prime importance. A famous Zen Koan exemplifies this: “Is it the wind that waves the flag, or the flag that waves the wind?” The distinction between ”flag” and ”wind” as subject and object is purely conceptual; in reality the waving of the flag and wind is a single process. Without the flag, the wind would not be disrupted and without the wind, the flag would not wave. Similarly, the properties in our model drive the exchange between the boxes, while the exchange determines the properties of the boxes.

We conclude that sapropel formation in the Mediterranean Sea is an inherently transient process. In the Black Sea, a steady state is reached with a high organic carbon burial rate, resulting in a single organic rich deposit. A monotonic sea-level curve shows the best match with the geological data of the Black Sea. We find that our model captures the main trends found in geological records of both the Mediterranean Sea and Black Sea.


nditions, latest version, which are lodged at the Chambers of
General Conditions can be sent free of charge on your request.
Bulgaria
Montenegro
Prishtina
Sofia
Podgorica
Skopje
Harbour Istanbul
Adriatic Sea
Tirana
Sea of Marmara
Ankara
Albania
ocida
Turke
Kerkyra
Greece
Station 9 / extra
Station 8
Athens
Ionian Sea
Kos
Nicosia
Harbour
Leb
Kriti (Crete)
Station 5
Station 3
Station 2
Statio
station 6
Station 4
Mediterranean Sea
US Dept of State Geographer
© 2015 Google
© 2015 Basarsoft
© 2015 ORION-ME
Google
Gaza Strip
Imagery Date: 12/14/2015
37°43'18.14" N 25°38'14.20" E
403
405
406
407
408
409
414

1 Introduction

1.1 Physical and chemical processes in semi-enclosed basins

Understanding the interaction between oceanic circulation and climate forcing is of great importance, as today's global circulation is being affected by rapid climate change and vice versa; a large change in circulation would also have a significant impact on climate. In this thesis we investigate the interaction of these two components of the climate system. As, in general, these interactions are very complex, we choose to limit our study to a relatively simple system: a semi-enclosed basin. In contrast to the world's ocean, modeling of this relatively small and isolated system is feasible on both human and geological time scales. The Mediterranean Sea is a good example of a semi-enclosed basin, where the sea is mostly surrounded by land, with only a narrow connection, the Strait of Gibraltar, to the ocean (Figure 1.1). Such basins provide a largely isolated marine system, in which the water circulation is more sensitive to climatic perturbations (Rossignol-Strick, 1985; Hilgen, 1991; Lourens et al., 1996; Cramp and O'Sullivan, 1999). Below we describe the physical processes in semi-enclosed basins relevant for this thesis.

In semi-enclosed basins like the Mediterranean Sea, **strait exchange** is the only direct exchange with the outside, i.e. the Atlantic ocean and the Black Sea. As the contribution of various processes depend on the geometry of the strait, we focus on theory relevant to the Mediterranean and Black Sea. In the Mediterranean Sea, the total annual evaporation exceeds the precipitation and river discharge into the basin (Romanou et al., 2010), meaning that the basin has a negative freshwater budget. In addition, the basin has a net annual heat loss to the atmosphere (Song and Yu, 2017). Both of the aforementioned processes cause an increase in density at the surface. When the density of the surface water exceeds that of the underlying water mass, **convection occurs**: the water masses fully mix. In the ocean, convection occurs locally, causing the two water masses to mix instantaneously, in less than one year, resulting in a single, uniform, water mass. At the level of the sill at the Strait of Gibraltar the water thus has a higher density than the Atlantic water, causing a density-driven outflow and a compensating inflow. As the volume of the Mediterranean is constant, there is a surface current that compensates for both the density-driven current and the net freshwater budget of the basin. This is called an anti-estuarine circulation. In contrast, in the Black Sea the annual river outflow

---

Picture left: A photo taken on the RV Pelagia during cruise 64PE-406-E (January 2016), showing the route: from Cyprus, across the Levantine basin and Ionian Sea to Italy, through the Corinth Channel of Greece, into the Aegean Sea and through the Sea of Marmara to the final destination: Istanbul. At each station data was collected.

and precipitation exceed the evaporation, causing a density-driven inflow from the Mediterranean Sea and a compensating outflow at the surface; an estuarine circulation.

Deep water formation is the process where water descends to the deepest levels of the basin. In the Mediterranean Sea it occurs in the Gulf of Lion through convection (Hayes et al., 2019; Wu and Haines, 1996). In the eastern basin (figure 1.1) deep water formation occurs through a more complex process: winter storms cause a rapid cooling at the surface and hence strong convection in parts of the Adriatic and Aegean Sea, the marginal basins. These basins are separated from the Mediterranean proper by straits, the concept of strait transport therefore applies. The high density marginal water will flow to the Mediterranean proper, where its high density will cause it to sink to the sea floor (Schroeder et al., 2012; Malanotte-Rizzoli, 1991; Gertman et al., 2006; Roether et al., 1996; Marshall and Schott, 1999; Bensi et al., 2013). The water with the highest density in the Black Sea is the Mediterranean inflow water. In the Black Sea, the Mediterranean inflow water directly sinks when it flows into the basin, similar to how the water from the marginal basins sinks when it reaches the main basin of the eastern Mediterranean Sea.

Regardless of the mechanism, deep water formation brings oxygen from the surface - where the oxygen concentration is in equilibrium with the atmosphere - to the deep water. This process is therefore crucial for most life in these water masses, as well as for the break down of organic matter. Besides oxygen, life also needs nutrients, which are supplied to the surface water by the rivers and, to a lesser extent, wind blown dust. As the currents distribute the nutrients and oxygen throughout the ocean, both horizontally and vertically, the chemical processes are closely coupled to the physical processes. Some of the organic matter produced in the surface water reaches the deep water, e.g. through sinking and mixing. The amount of organic matter that is transported to the deep water is called export productivity. When organic matter is decomposed, oxygen is consumed. When the oxygen consumption in the deep water exceeds the supply from the surface, the deep water eventually becomes anoxic. Consequently, most life in the deep water water will die and organic matter, largely produced in the surface and intermediate water, is preserved. An increase in nutrient input can therefore cause increased productivity, which in turn increases oxygen consumption when the organic matter is broken down.

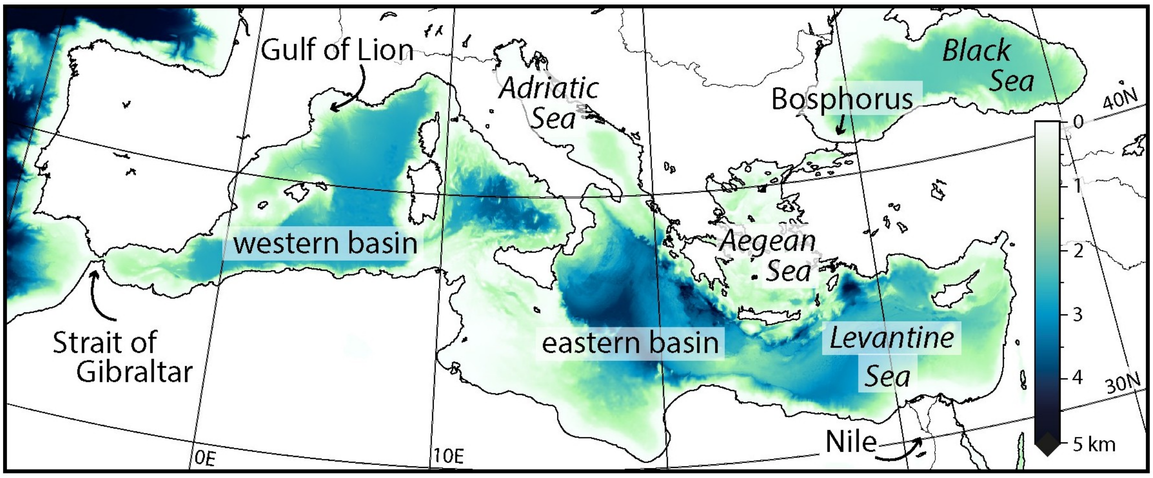

Figure 1.1 A map of the Mediterranean and Black sea, showing the main sub basins and sea straits.

1.2 Sapropel formation in the Mediterranean Sea

Studying the geological past is a powerful way to gain insight into the interaction of atmosphere and ocean. Reconstructing oceanic processes in the past gives a better understanding of how the system responds to perturbations in the present and future, this area of research is called paleoceanography. It is possible to study oceanic processes throughout geological history because water properties and circulation are, to some extent, registered in the sediments that are continuously being deposited on the sea floor. These sediments can either be studied on land, when they were uplifted, or by collecting sediment cores from the deposits on the sea floor. Sediments of the Mediterranean sea show alternating grey mud and laminated dark, organic rich, layers. In the eastern basin (Figure 1.1), these characteristic dark layers, called sapropels, are found at regular time intervals throughout most of the history of the Mediterranean Sea. They are thought to form when a peak in the Nile outflow causes the circulation to slow down and export productivity to increase (e.g. Rossignol-Strick et al., 1982; Rohling, 1994; Higgs et al., 1994; Jorissen, 1999; Thomson et al., 1999; Mercone et al., 2001; Abu-Zied et al., 2008). This limits the oxygen supply to the deep water, which, as discussed above, can result in anoxia and consequently the preservation of organic matter. A sapropel is formed when sufficient organic matter is deposited. The Nile outflow is affected by the monsoon intensity, which is in turn modulated by climatic precession. Hence sapropels are found at 21 kyr intervals. During precession minima, the summer monsoon falls in the Nile catchment, causing a significant increase in discharge (e.g Rossignol-Strick et al., 1982; Rohling, 1999; Rohling et al., 2002; Scrivner et al., 2004; Bianchi et al., 2006; Marino et al., 2007). Amies et al. (2019) suggests that during sapropel S5 the Nile outflow may have been nine times higher than present.

The sediments at the sea floor record past oceanographic and climatic conditions in so called proxies. For example, the trace metals barium and molybdenum are indicators for productivity and bottom water oxygenation respectively. The concentration of these trace metals can be determined by means of an X-Ray Fluorescence (XRF) scanner. In addition micro fossils, such as foraminifera and dinoflagellates, are often used to reconstruct oceanographic conditions.

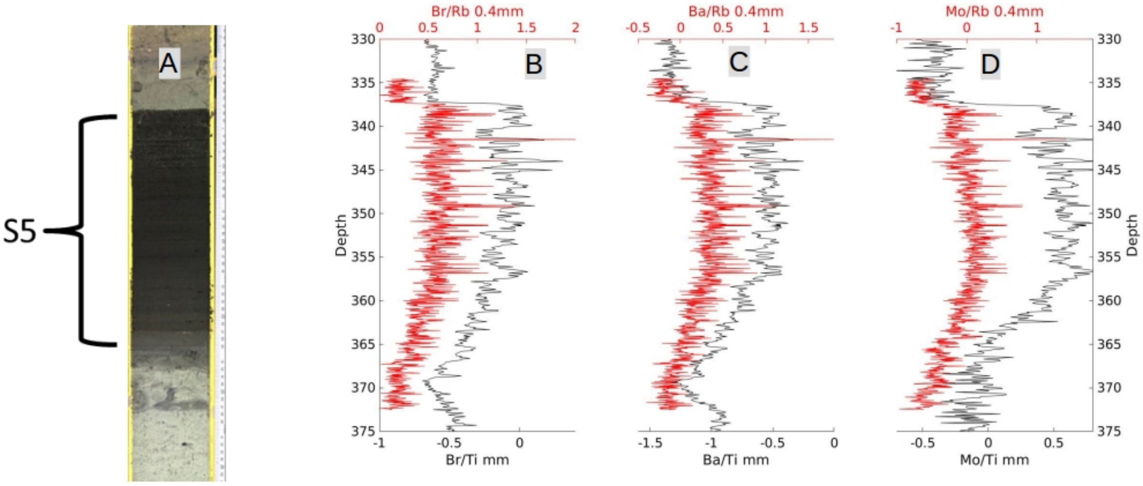

Figure 1.2 Panel A: The piston core used in this thesis. Piston cores are collected by pushing a roughly 15 cm diameter, 14 meter long tube into the sediment driven by a heavy weight. The core was cut in meter long sections for transportation to the lab at the Royal Netherlands Institute for Sea Research (NIOZ) on Texel, the Netherlands. Next, the core sections are opened by cutting them in half, for further investigation. The black layer shows the sediments of saporpel S5. Panels B-D show the corresponding graphs of the trace metals bromium, rubidium and molybdenum respectively, as determined with an XRF core scanner. The element counts are normalized to either titanium or rubidium counts. The red lines represent measurements with a 0.4 *mm* resolution, normalized to rubidium and the black lines 1 *mm* resolution measurements normalized to titanium. These results are further discussed in Chapter 3.

1.3 Scope and framework of this thesis

Figure 1.2 shows something remarkable: a *very* sharp transition from dark gray to light gray. The picture suggests that the mechanisms of sapropel formation involve an abrupt transition in oceanic circulation. So how is it possible that a slow varying process like the precession cycle causes such a sharp transition? Fast transitions in oceanographic conditions are of particular interest for today's climate, as a sudden change in the global oceanic circulation would have drastic consequences for all living beings on Earth. More generally, this study contributes to the knowledge of the Mediterranean sea. Sapropels provide unique high resolution records of past oceanographic variability with fast transitions and are therefore ideal for our goals. The Mediterranean Sea has been studied extensively. An abundant amount of observational studies and well-dated sediment cores allow us to calibrate our model to both present and past oceanographic conditions. In addition to geological data, modeling studies can be used to gain insight into parameters that are not recorded in the sedimentary record or would require an unreasonable number of sediment cores. Moreover, hypotheses derived from core data can be validated by models: models can give insight into whether the conditions derived from the sedimentary record allow for certain physical or chemical processes to occur. We use time-frequency analysis of a sediment core record in combination with a transient model to understand and describe the underlying mechanisms of sapropel formation in the Mediterranean Sea.

The formation of sapropels encompasses five orders of magnitude in timescales, ranging from the seasonal and annual processes that control the main features of the current circulation of the Mediterranean Sea, to the variability of Earth's orbit and orientation relative to the sun, which acts on timescales of $10 - 10^5\ yrs$ and beyond. Consequently, our model must be capable of runs of tens of thousands of years, while also having a resolution in the order of a year. Existing modeling studies are limited to time short slice experiments and equilibrium runs (e.g. Bigg, 1994; Myers, 2002; Meijer and Dijkstra, 2009; Mikolajewicz, 2011; Grimm et al., 2015), thereby describing equilibrium conditions. Indeed, there are intervals during which the oceans were in equilibrium on millennial timescales, but such an approach would not give insight into the high frequency variability or rapid transitions found in sapropels. Oceanic general circulation models use a high spatial resolution of bathymetry and hydrodynamic parameters. However, these computationally intensive calculations, limit their use to time slice experiments of at most a few thousand years. Running such a model for an entire precession cycle takes months on a cluster and is therefore impractical. Moreover, the output contains so much detail that it becomes problematic to identify the key processes.

In contrast, box models have a low spatial resolution, i.e. a low number of boxes, resulting in a very short run time of seconds on a simple computer. Such models are ideal for sensitivity and trend analyses and for understanding the various oceanographic processes: the relatively low complexity reveals the main driving mechanisms. We therefore use a box model. So far, most paleoceanographic box models use constant water fluxes between the boxes and are essential steady state models. Moreover, the previous box models for the Mediterranean Sea, Matthiesen and Haines (2003); Amies et al. (2019), do not include the deep water as a separate box and are therefore not suitable for studying deep water formation.

We present a novel transient box model, which includes deep water formation, that calculates a full precession cycle of 20 kyr runs, with a high temporal resolution of one year. Each box represents a uniform water mass with constant volume or the atmosphere, which interacts with the surrounding boxes by water flow, heat exchange and diffusive mixing. The boundary conditions, such as the atmospheric conditions and those in the Atlantic ocean, are represented by static boxes: they either have constant or predefined properties, but their properties are not affected by other boxes. The exchange of properties and water flow between boxes is described by differential equations. The new properties of all non-static boxes are calculated at each time step, based on the exchange of properties between the boxes. The model set up is described in more detail in chapters 3 and 5.

This thesis is organized as follows: **Chapter 2** describes the high frequency oceanographic variability found in sapropel S5 in core 64PE406-E1, collected with the RV Pelagia in the Levantine basin. The trace metal concentration in the core is measured with an XRF core scanner, which provides a high spatial resolution with an excellent signal-to-noise ratio, allowing to study high frequency oceanographic variability. Although the concentration of many trace metal is measured, especially the trace metals barium (Ba), bromium (Br), manganese (Mn) and molybdenum (Mo) are of interest. These trace metal are proxies for productivity, marine organic carbon, burn down and anoxia respectively. They are normalized to either titanium or rubidium to prevent a closed sum effect. Upon closer examination, the core and XRF record shown in figure 1.2 reveals a complex, periodic and layered structure. A time-frequency analysis, i.e. a so-called wavelet analysis, is applied to the XRF core scanner data, to calculate the frequency content along the core. Several characteristic periods are found, in the range of $50 - 1000\ yrs$. These periodicities are a direct result of external forcing (e.g. solar variability), or introduced by a non-linear response of the Mediterranean Sea to both external forcing and internal feedback mechanisms. The sapropel appears to be terminated abruptly. The absence of a Mn peak indicates that there is no burn down. This suggests that an almost instant transition (in a few millimeter in the sediment core) from the sapropel state to a state with oxygenated bottom water occurred.

Chapter 3 describes the fundamentals of a transient box model for semi-enclosed basins, applied to sapropel formation in the Mediterranean sea. The model uses three dynamic boxes. The first box represents the deep water formation sites, the second box the surface and intermediate water of the open basins and the third box the deep water. Each of the boxes exchanges properties with the surrounding boxes. Furthermore, static boxes are included that represent the atmosphere, rivers and the Atlantic ocean. It is found that sapropel formation is an inherently transient process, underlining the value of a coupled dynamic model. Furthermore, the model matches the data best when the freshwater budget of part of the basin temporarily becomes positive during sapropel formation, which is disputed in previous literature. Although this model captures the fundamental mechanisms of sapropel formation, it cannot explain most of the high frequency variability.

In **Chapter 4**, a dynamic nutrient model is added, demonstrating the flexibility of our box model framework. The nutrient model describes the production, breakdown and burial of organic matter, and therefore also the oxygen consumption. The model is applied to the Black Sea, to study the effects of the opening and closing of the Bosphorus strait. We find that the model can capture the main trends found in geological records. This study highlights the value of a combined dynamic model.

Next, in **Chapter 5**, separate intermediate water boxes are included in the same framework. Now the high frequency variability *is* reproduced. In the above we introduced the question “So how is it possible that a slow varying process like the precession causes such a sharp transition?”. The model results suggest that this variability originates from transitions to new equilibrium states, caused by precession variability, i.e. the high frequency content in the core data largely represents internal variability. In other words, slow processes can trigger fast transitions. Moreover, it is shown that sapropels only form as they do in the geological record when the freshwater budget briefly becomes positive, but not long enough to reverse the density gradient at the strait. Previous literature concluded that the currents at the strait did not reverse, which is in agreement with our results.

2 A Novel Approach Using Time-Depth Distortions to Assess Multicentennial Variability in Deep-Sea Oxygen Deficiency in the Eastern Mediterranean Sea During Sapropel S5

Based on: Dirksen, J. P., Hennekam, R., Geerken, E.,& Reichart, G. J. (2019). A novel approach using time-depth distortions to assess multicentennial variability in deep-sea oxygen deficiency in the Eastern Mediterranean Sea during sapropel S5. *Paleoceanography and Paleoclimatology*, 34(5), 774-786.

Abstract

Reconstructing millennial- to centennial-scale climate variability for the Eemian-an interval with estimated sea surface temperatures $\sim 0.5\deg C$ warmer than "preindustrial"-requires records with high temporal resolution. Sapropel S5 sediments, deposited under anoxic conditions in the Eastern Mediterranean Sea, offer the rare opportunity to assess multicentennial climate variability during this time. Here we present high-resolution S5 piston core data from the Nile delta region. Specifically, we focus on Ba/Ti, Br/Ti, and Mo/Ti, as they are proxies for paleo-productivity, marine organic carbon, and sediment anoxia, respectively. A high correlation between our Ba/Ti values in core 64PE-406-E1 and well-dated Ba records of nearby cores (LC21 and ODP967) was found. We, therefore, tuned our data to these cores obtaining an initial age model. A time-frequency analyses indicated significant frequency content in the multicentennial band, although the frequency components drifted over time. Assuming spectral simplicity, we corrected for sedimentation rate changes on a multicentennial time scale. This novel approach grants a higher-resolution age model. The resulting variability in sedimentation rate is similar to records of monsoon variability, indicating a possible link between sedimentation at the core location and low-latitude monsoon variability, linked via the River Nile. Moreover, the periodicities found in the sapropel time series are similar to the frequency content of total solar irradiance

---

Picture left: a close up of core 64-PE406-E1, showing part of sapropel S5 (black) at the bottom and clay (grey) at the top. Note the sharp transition and the fine laminations in the sapropel. The vertical scale is aprroximately 15 *cm*.

and sunspot records known for the Holocene, at least at high frequencies ($\sim$ 50-150 years). Hence, our data suggest cyclic intrasapropel variability, at least during the deposition of sapropel S5, may be linked to solar cycles.

2.1 Introduction

During the Quaternary period, climate has fluctuated between glacial and interglacial states, paced by astronomically driven changes in insolation, on time scales of 10^4 to 10^5 years (e.g. Tzedakis et al., 2017). Millennial-scale oscillations were first identified by (Heinrich, 1988), who found periodically occurring ice rafted detritus in the North Atlantic. Later, climate oscillations on time scales of 10^2 to 10^3 years were first recognized in the ice cores from Greenland Dansgaard et al. (1993) and by Grootes et al. (1993) in the same year. At the same time, it was reported that during the last interglacial (Eemian), climate was more unstable than during the present interglacial, at least in Greenland (Anklin et al., 1993; Dahl-Jensen et al., 2013), and suborbital climate variability during this time interval was later also shown in Atlantic sediment records (Oppo et al., 2001, 2006). The discovery of the high-frequency climate oscillations resulted in a quest for similar frequency changes in other records, in both the continental (Blaga et al., 2013; Wang et al., 2001) and the marine realm (Altabet et al., 2002; Haug et al., 2001). Some studies suggest that these high-frequency climate oscillations are linked to glacial conditions or that the glacial boundary conditions at least enhance the impact of some unknown inherent oscillation of the climate system (e.g. Bond et al., 1993, 1997), although they have also been found in nonglacial conditions (for example Barker et al., 2011). We further investigate this suborbital climate variability in a relatively warm climate. These results can therefore also be used to assess the importance of multicentennial climate variability for near future climate change.

Of particular interest is Marine Isotope Stage 5e (MIS-5e; $\sim 129 - 116\ ka$), where global sea surface temperatures may have been $\sim 0.5 \deg C$ warmer than preindustrial levels (Hoffman et al., 2017). MIS-5e may not be a perfect analogue for future global warming, as anthropogenic forcing differs significantly from natural forcing (and due to the different orbital parameters), but still this interval can give valuable information on mechanisms and feedbacks that operate in a comparable warmer climate (e.g. Capron et al., 2017). Although this time interval has been studied extensively, very few studies achieved a sufficient resolution to investigate multicentennial climate variability. Most continental records lack sufficient time control, whereas marine records mostly lack resolution due to bioturbation.

The Mediterranean Sea is one of the few basins that allow studying high-resolution climate change at the lower latitudes during warm intervals. Limited water exchange with the open ocean makes the Mediterranean Sea, with its antiestuarine overturning circulation, extremely vulnerable to climatic perturbations. This is exemplified by the repeated deposition of organic-rich layers in the Eastern Mediterranean Sea, that is, sapropels, linked to precession minima (Cramp and O'Sullivan, 1999; Hilgen, 1991;

Lourens et al., 1996; Rohling et al., 2015; Rossignol-Strick, 1985; Rossignol-Strick et al., 1982). Sapropels are thought to reflect changes in the Northeast African monsoon intensity, which affect mainly Nile outflow (Rohling et al., 2015; Rossignol-Strick, 1985), reducing deep sea ventilation. Concomitantly increasing eastern Mediterranean productivity due to the development of a deep chlorophyll maximum, additional nutrients from the Nile River, and/or phosphorus regeneration from anoxic sediments, as well as related remineralization at depth, is suggested to result in bottom water anoxia and enhanced preservation of organic matter (Lange et al., 2008; Kemp et al., 1999; Krom et al., 2002; Rohling and Gieskes, 1989; Rohling et al., 2015; Slomp et al., 2002; Van Santvoort et al., 1996, 1997). The lack of bioturbation during these anoxic periods produces perfectly preserved sedimentary archives, allowing high-resolution climate reconstructions.

Sapropel deposition is thought to occur time-synchronous (within age uncertainties) in the entire Mediterranean Sea basin, at least during sapropel S1 (Lange et al., 2008), and therefore, age constraints from different sites can be used to cross-tune Eastern Mediterranean records. Grant et al. (2012, 2016) transferred the ages of the well-dated Soreq cave speleothem record to eastern Mediterranean Sea core LC21 using common $\delta^{18}O$ variability in these two records. Core ODP967, taken close to our core 64PE406-E1, has been synchronized to the LC21 record using both Ba (export-productivity proxy) and $\delta^{18}O$ variability (Rodríguez-Sanz et al., 2017a). Hence, to obtain a robust initial age model, our 64PE406-E1 record is cross-correlated to cores LC21 and ODP967 (see Figure 1 for core locations) using common Ba signals.

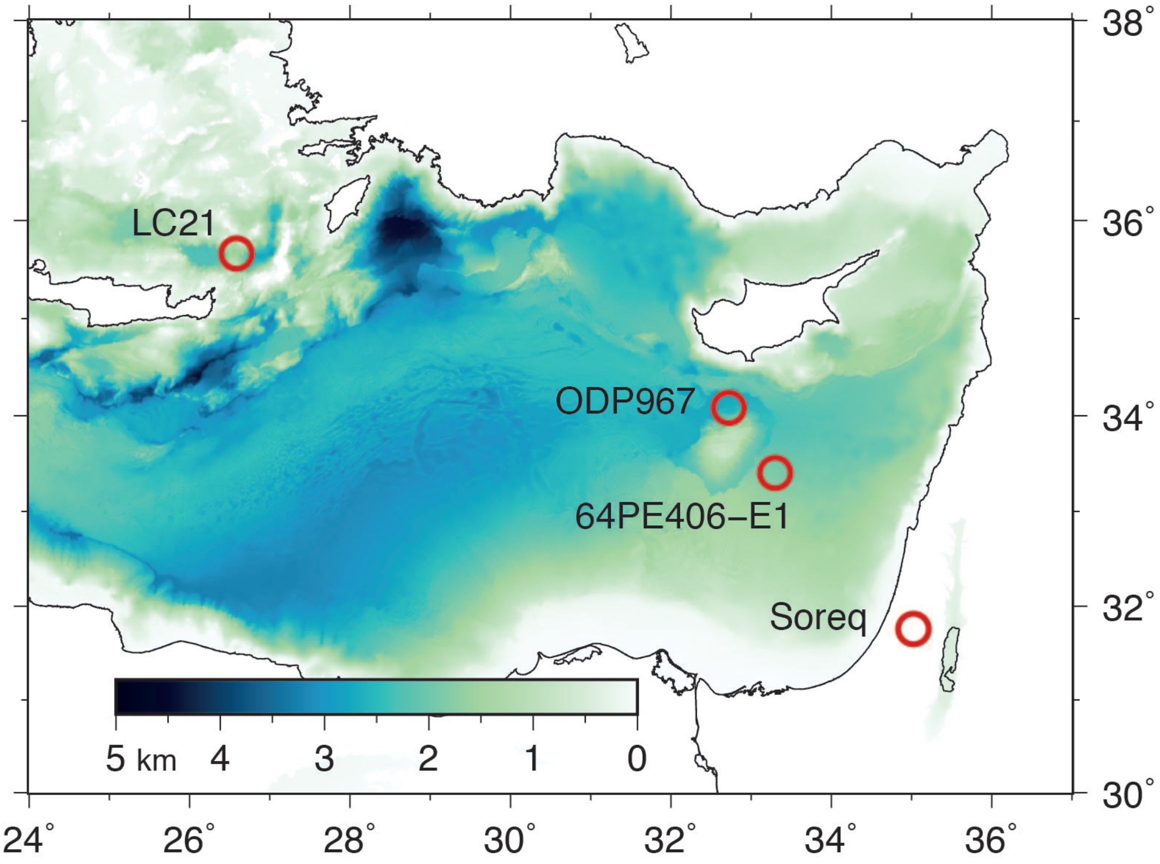

Figure 2.1 Bathymetric map of the Eastern Mediterranean Sea, indicating the locations of cores 64PE406-E1 (this study), LC21, and ODP967, as well as the location of Soreq cave.

Here we study a well-preserved sapropel deposited during MIS-5e, recovered close to the Nile delta, to investigate millennial to centennial time scale climate variability in the Mediterranean Sea. The laminated sediments of the sapropel were analyzed using an X-ray fluorescence (XRF) core scanner. These high-resolution time series were subsequently evaluated in the depth and time domains to establish a new internally independent chronology for the sapropel. For this we use “spectral simplicity” (Schiffelbein and Dorman, 1986), which assumes a more or less constant frequency content on a millennial to centennial time scale to establish an independent depth-to-age calibration. Similar methods have also been used by Park and Herbert (1987) and Herbert (1994) to assess the effects of variations in sedimentation rate records of paleoclimatic variability on orbital time scales. After correcting this way for time-depth distortions, the spectral content of the signal is compared to known frequencies of climate variability. Ultimately, this is used to study in detail the sedimentation in the Nile delta and to study centennial to millennial climate signals in the Mediterranean Sea during the Eemian.

2.2 Material and Methods

2.2.1 Sediment Material

Core 64PE406-E1 (33 18.14898'N, 33 23.71998'E, water depth 1,760 m) was collected during the Netherlands Earth System Science Center research cruise in the Eastern Mediterranean Sea conducted with R/V Pelagia in January 2016 (Figure 1). This 9.2-m-long piston core shows an alternation of brown/gray clays with black laminated sapropel sediments. We observe at least four sapropels, which we relate to S1, S3, S4, and S5, at following depth intervals: S1 is partially present in the top of the piston core and complete in an accompanying multicore; S3 (1.7-2.0 m), S4 (2.5-2.8 m), and S5 (3.3-3.7 m).

2.2.2 XRF Measurements

The core was analyzed for its geochemical composition using an XRF core scanner (Avaatech) at the Royal Netherlands Institute for Sea Research (NIOZ) in The Netherlands. We used three different voltage settings (10, 30, and 50 kV) to measure all relevant elements from Al to Ba (Richter et al., 2006), and we specifically focus on Ti, Br, Rb, Mo, Mn, and Ba for this study. First, the entire core was scanned at a 1-cm resolution on the "work half" core section (results shown in Figure 3). Second, the interval surrounding sapropel S5 was XRF scanned at a higher 1-mm resolution, again on the "work half" core section (figure 2). Lastly, we measured sapropel S5 in an even higher 400-μm resolution on the "reference half" core section (Figure 4). As the signal-to-noise ratios for the XRF intensities of the elements change with the used resolutions, we assessed the signal-to-noise per element per resolution in order to end up with the highest resolution proxy signal with acceptable signal-to-noise ratio as possible. These tests showed robust signal-to-noise ratios for Ti, Br, Rb, Mo, Mn, and Ba at centimeter and millimeter resolutions, whereas signal-to-noise ratios at 400 μm were sufficient for Br, Rb, Mo, and Ba. The XRF data for sapropel S5 of all presented elements at all measured resolutions is available in the supporting information. image

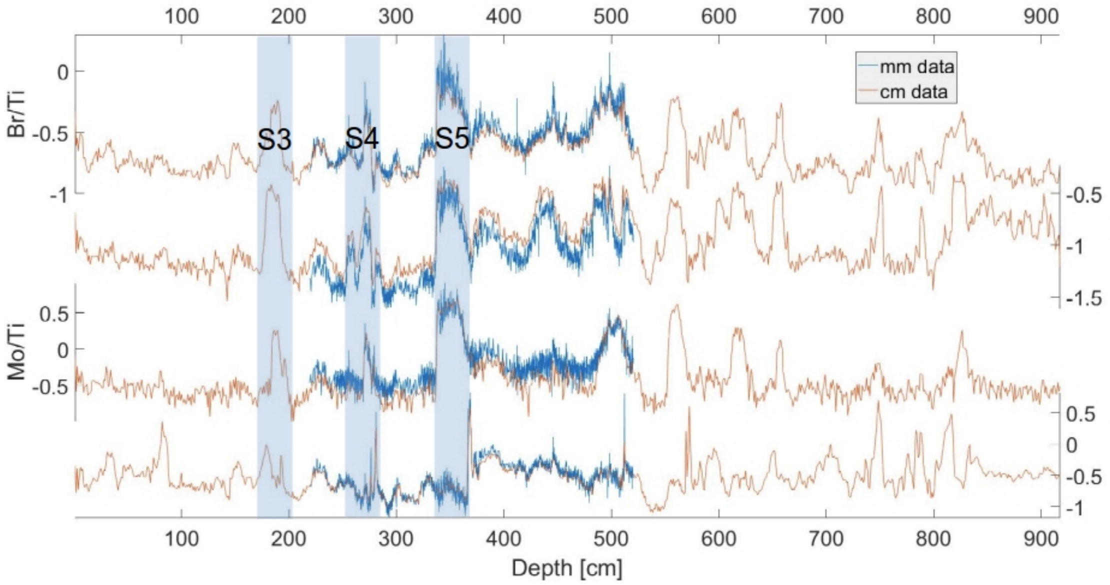

Figure 2.2 An overview of the centimeter- and millimeter-resolution XRF data of core 64PE406-E1. The blue lines show the millimeter resolution data of each element, and the orange lines the centimeter-resolution data. Various sapropels can be identified; the approximate locations of sapropels S3, S4, and S5 are indicated by the shaded area's.

Element ratios, rather than individual elements, are used to prevent closed-sum effects, and log ratios are favored because of asymmetry in normal ratios (Weltje et al., 2015; Weltje & Tjallingii, 2008). Although Al is generally used in geochemical studies for normalization, for XRF core scanning often other elements are used (mainly Ti) as the effect of water absorption is relatively large for a light element as Al (Weltje and Tjallingii, 2008; Hennekam and de Lange, 2012). As the signal-to-noise ratio for Ti was insufficient at the highest (400-μm) resolution, we also used Rb as an element for detrital normalization, which has previously been reported as a good alternative for Mediterranean Sea sediments (Thomson et al., 2006).

2.2.3 Statistical Approach

When correlating two element-to-element ratios, such as Br/Ti and Ba/Ti, with the same independent variable, correlation may be spurious (Pearson, 1897; Simon, 1954). Pearson (1897) already wrote that such spurious correlations can be recognized by varying the numerator/denominator randomly. Hence, we performed Monte Carlo simulations on the XRF data sets to validate the significance of correlations. Specifically, the XRF data of the numerator variable (e.g., exemplified by Ba in Figure 5) was replaced by a pseudo random variable, having the same statistical distribution and relative range of values as the replaced variable over the selected interval. We subsequently calculated correlation between this pseudo random ratio (random/Ti) and the second element ratio (e.g., exemplified for Mo/Ti in Figure 5). The here used Monte Carlo simulation applied 10^4 draws. From this, an artificial distribution was obtained, showing the correlation based on the spurious correlation only (blue bars in Figures 5C and 5F), representing noise in the numerator only. When the actual correlation (red lines in Figures 5C and 5F) is much higher than the simulated correlations, this confirms statistical significance of the correlation between the actual ratios.

2.2.4 Frequency Analyses

Time series of the XRF proxy records were analyzed in the time-frequency domain using wavelet transforms (Kirby and Swain, 2013; Torrence and Compo, 1998). Like a windowed Fourier analyses, it uses multiple Fourier transforms to calculate the spectral content of a signal but without the limitation of a uniform time window. A Morlet wavelet with 500 scales and zero padding was used, which is suitable for studying oscillatory signals (Grossmann and Morlet, 1984). In order to focus on sub-Milankovitch cycles, we first removed the offset and trend by subtracting a fitted third-order polynomial, before the actual wavelet analyses. Applying a filter to remove frequency content in which we are not interested would be superfluous, as for each scale of the wavelet the signal is already bandpass filtered at the appropriate frequencies. In a Morlet, a sine curve is multiplied with a Gaussian, with the central wave number setting the width of the Gaussian relative to the frequency. Hence, a higher central wave number increases the width of the sampled interval. Various central wave numbers in the range of 6-12 were used, covering a range of trade-offs between time and frequency resolution (Kirby and Swain, 2013). When higher-frequency resolution is required, a larger central wave number is used, up to 12. For shorter signals however, a low central wave number increases bandwidth, allowing the detection of lower frequencies (Kirby and Swain, 2013). Additionally, a low central wave number increases time resolution. An integral over the time axis of the wavelet transform was used to calculate a global wavelet. Similar to a frequency power spectrum, a global wavelet shows dominant frequencies and their relative power. When calculating global wavelets, power outside the cone of influence or above the Nyquist frequency is excluded. The Nyquist frequency was calculated by combining our highest XRF resolution of 400 μm with the first-order age model (see below), resulting in a typical Nyquist period of 12-60 years. As these frequency analyses require a constant sampling interval, the XRF data were resampled at an interval of 4 years, prior to analysis, which is shorter than the shortest time interval between two measurement points in any of the age models used (see below), thereby preventing aliasing.

2.2.5 2.5 Age Model and Time-Depth Distortion Removal

The sapropel periods are well expressed through the Ba/Al (or in this case Ba/Ti and/or Ba/Rb) ratio, which approximates the original total organic carbon concentrations (Van Santvoort et al., 1996, 1997; Lange et al., 2008). We transformed the age model of core LC21 (Aegean Sea, Grant et al., 2012, 2016), which was aligned to the excellently dated Soreq cave record, to our 64PE406-E1 core (see Introduction) by tuning the sedimentary Ba/Ti variability (Figure 3). Moreover, we verify this crosscorrelation of Ba signals by also comparison of our record to nearby core ODP967, which was also aligned to LC21 using Ba and $\delta^{18}O$ variability (Rodríguez-Sanz et al., 2017). Variability observed in the Ba/Ti record of core 64PE406-E1 and the Ba intensities of core LC21 and Ba/Ti of core ODP967 are very similar (see Figure 3). Hence, we use the same sapropel S5 boundaries as found by Grant et al. (2016) at 121.5-128.3 kyr BP to constrain our initial age model, which we subsequently improve by removal of time-depth distortions (see below). Note that this approach would not be suitable outside of sapropels, due to a lack of a clear signal.

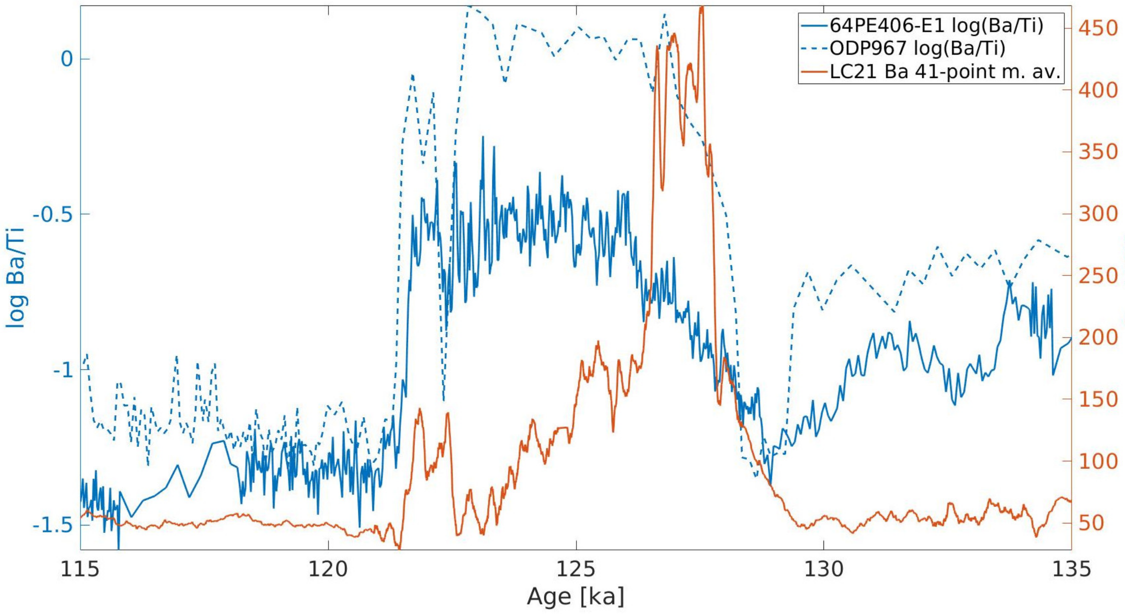

Figure 2.3 The element log ratios of Ba/Ti sapropel S5 is shown in blue (left axis), compared to the ODP967 Ba/Ti data (left axis) and the LC21 Ba data (right axis).

To study multicentennial variability within S5, we assessed whether the sedimentation rate remains constant throughout the sapropel using a time-frequency analyses. Time-depth distortions are removed by assuming constant frequency content, thereby correcting for sedimentation rate changes within the sapropel. We here follow the same reasoning proposed by Herbert (1994) to remove time-depth distortions for orbital time scales. Time-depth distortions were removed by assuming a constant frequency content on the millennial to centennial time scale by correcting for sedimentation rate changes within the sapropel. To this end, we added pointers to the initial age model at those depths where the frequency content appeared not constant. These pointers were subsequently moved in both time and depth to achieve a more constant frequency content.

2.3 Results

The centimeter- and millimeter-resolution XRF measurements show good correlations between all ratios (Figure 2). The 0.4-mm-resolution data show much higher-frequency variability, but the same trend as the millimeter-resolution data, with no difference between data normalized to Ti or Rb (Figure 4).

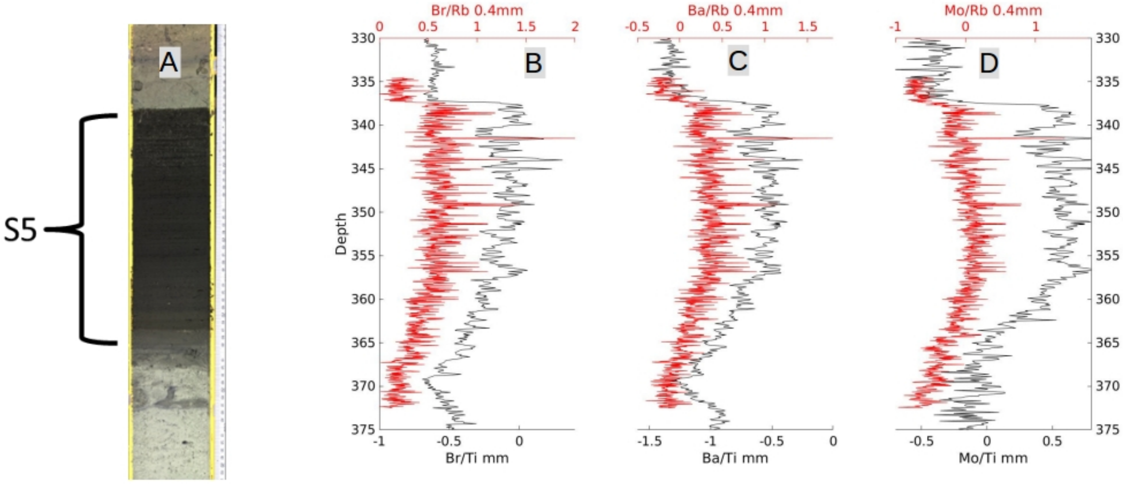

Figure 2.4 Panel A shows a line scan image of the core interval containing S5, which contains dark organic-rich sediment. Panels B-D show the corresponding graphs of the trace metals Bromium, Rubidium and Molydenum respectively, as determined with an XRF core scanner. The elements are normalized to either Titanium or Rubidium. Note an increase in all element ratios during the sapropel.

In the sapropel Ba/Ti, Mo/Ti and Br/Ti element ratios are elevated relative to presapropel and postsapropel values. In the XRF data millimeter-scale variability is observed, corresponding to multicentennial time scales (Figure 4). The three element log ratios shown in Figure 4 covariate, even on this millimeter scale. To validate whether this correlation is significant and not spurious, a Monte Carlo simulation has been performed, which randomly varies the numerator of the ratio (Figure 5; see also section 2.3). The correlation between Ba/Ti and Mo/Ti in S5 (see Figure 5) is significant ($R^2 = 0.894$ and $p < 10^{-4}$), while outside the sapropel, we find no correlation ($R^2 < 10^{-2}$ and $p = 0.4859$). This indicates that the data in the sapropel can be used for further analyses of multicentennial climate variability, while the variability outside the sapropel behaves as noise.

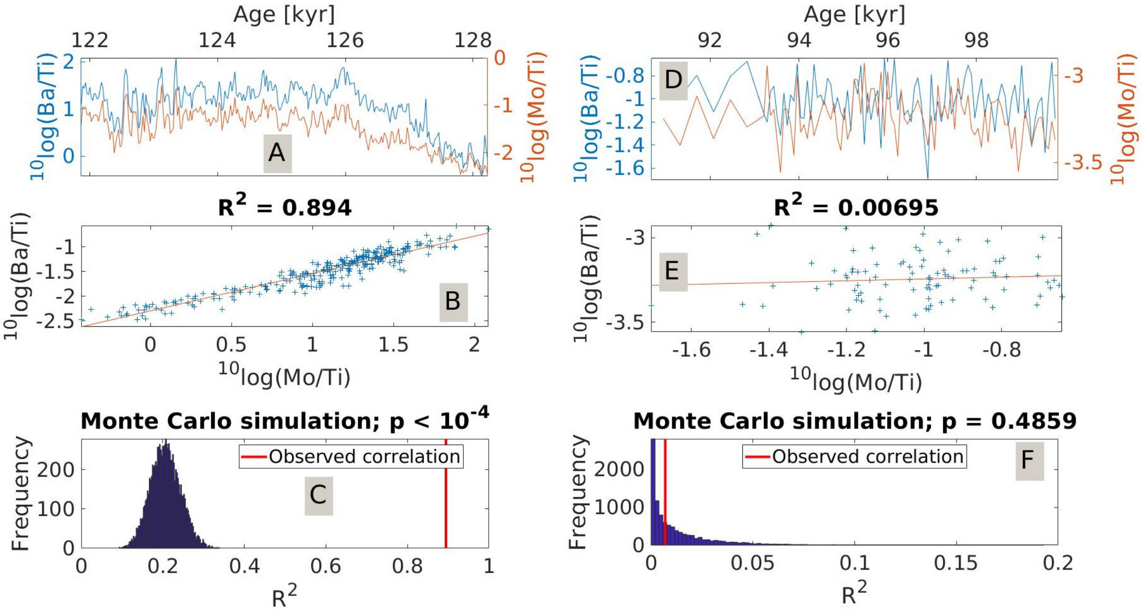

Figure 2.5 (A, D) A zoom in over the selected interval. (B, E) A correlation plot of these element ratios over the selection interval. (C, F) The results of a Monte Carlo simulation, performed on the selection interval. The distribution (in blue) is the correlation between the two ratios, if Mo, one of the two dependent variables, is replaced by a pseudo random variable, with the same distribution as Mo. The p value indicates the likelihood that a random draw has a better correlation with the second ratio than the measured data, the null hypothesis.

The wavelet transformation shows the frequency content in the time domain, based on our initial age model (Figure 2.6A). Although the global wavelet shows distinct frequency peaks, the variability relative to the mean value is very low, as shown in Figure 2.6C. This relatively low contrast is in line with the drifting frequencies observed in the wavelet transform in Figure 2.6A. The wavelet transform shows several frequency peaks, which seem to drift over time. At 127 $kyrBP$, a sudden shift in frequency can be seen in the $400-$ to $600-year$ period band (Figure 2.6A), with the main peak jumping from about 500 to 380 years. From $127-123$ ka, the spectral peak in this band slowly appears to increase again to a period of approximately 600 years. After 123 ka, the pattern does not allow to unequivocally distinguish between the different spectral peaks.

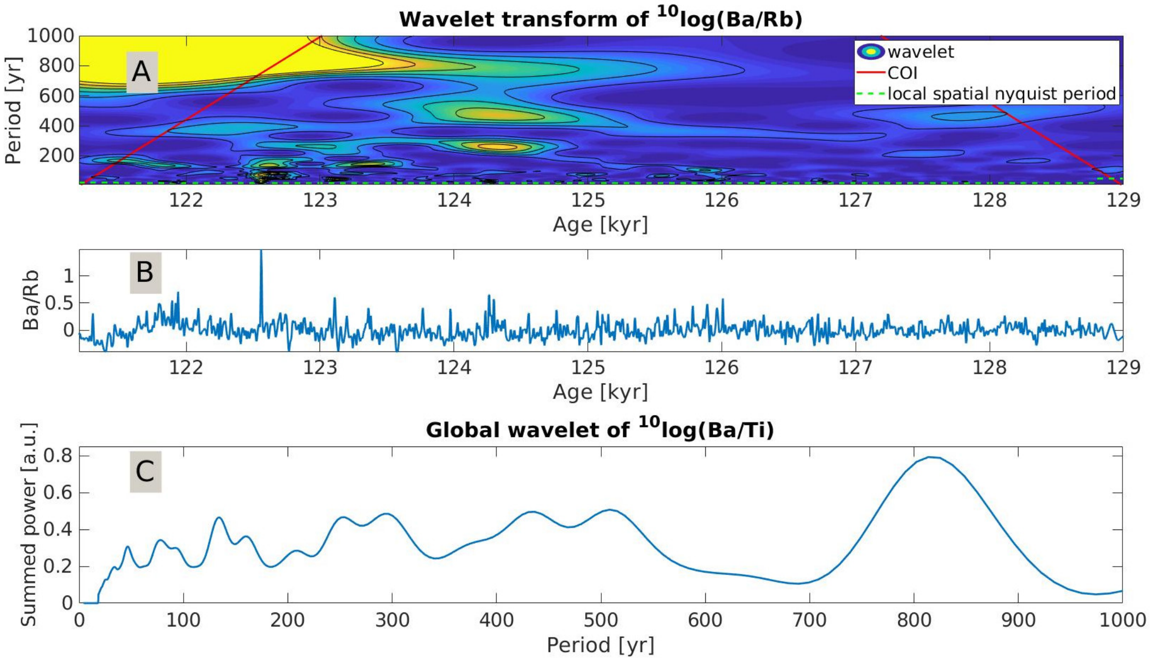

Figure 2.6 (A) The wavelet transform of the element log ratio of Ba/Rb with a central wave number of 8, when assuming a constant sedimentation rate in sapropel S5. Several frequency components can be observed in the multicentennial band, although the frequencies are not constant. The dashed green line indicates the local spatial Nyquist period, corresponding to the minimal observable period when time-depth distortions are present (Herbert, 1994). The solid red line indicates the cone of influence (COI) of the wavelet transform. (B) The analyzed signal: the element log ratio of Ba/Rb from which the dominant precession signal was removed (see section 2). (C) The integrated power of the wavelet transform over the time axis, a global wavelet. The global wavelet represents a frequency power spectrum.

2.4 Discussion

2.4.1 Elemental ratios in sapropel S5

Even at the highest-frequency variability is found to correlate significantly between the studied element ratios in sapropel S5 (see Figure 2.5). We can, therefore, use these XRF records to investigate multicentennial climate variability within sapropel S5. Normalizing the XRF measurements to Ti may in some settings result in an influence of aeolian dust on the signal, as Saharan dust is enriched in Ti Lourens et al. (2001). However, we also normalize to Rb, which similarly to Al, is related to the fluvial aluminosilicate component (Thomson et al., 2006). As we find no notable difference between the element/Ti and element/Rb ratios, we conclude that any influence of aeolian dust is very small. Ba/Ti is regarded an indicator of paleoproductivity (e.g. Bishop, 1988; Dymond et al., 1992), while Br/Ti correlates well with marine organic carbon in the Mediterranean Sea (Ziegler et al., 2008). Mo/Ti is a proxy for bottom water anoxia (e.g. Scott and Lyons, 2012; Tribovillard et al., 2006). Nile outflow provides nutrients and fresh water, which is widely assumed to mechanistically underlie sapropel formation (Rohling et al., 2015, and references therein). Moreover, nutricline rise into the lower photic zone (Rohling and Gieskes, 1989) and enhanced regeneration of phosphorus (Slomp et al., 2002) due to anoxic bottom water might have played a major role in the productivity increase during sapropels as well. Consequently, paleo-productivity, sediment organic carbon concentrations, and anoxia are probably all interrelated and controlled by monsoon intensity variability, linked through the River Nile (Lange et al., 2008; Hennekam et al., 2014; Rohling et al., 2015). In contrast to Mo, Mn precipitates as MnO2 within the sediment when the bottom waters get oxygenated. Pore-water Mn2+, formed during sapropel formation, diffuses upward and reacts with O2, diffusing downward from the oxygen-rich bottom waters, forming Mn oxides. Peak concentrations in Mn can hence be used to indicate burn down (Van Santvoort et al., 1996). Consequently, when a peak in Mn/Ti is found within a sapropel, this indicates that burn down proceeded into the sapropel. Such a Mn/Ti peak is observed within sapropel S3 (see Figure 2.2) but absent from the top of sapropel S5. This implies that burn down did not appreciably affect the record of S5. Sapropel S5 is hence preserved completely and well suited to assess multicentennial variability in trace elements and fine tuning of the record based on this variability.

2.4.2 Productivity and ventilation during sapropel S5

The covariance of Ba/Rb, Mo/Rb, and Br/Rb during sapropel S5 on multicentennial time scales suggests that the processes causing the fluctuations in these element ratios are also linked. A link between productivity and sediment anoxia has been shown before in the Nile delta region for sapropel S1, also on centennial time scales (Hennekam et al., 2014; Jilbert et al., 2010). These factors are either linked directly (i.e., higher productivity increases oxygen draw down) or indirectly, both reflecting changes in the primary drivers (i.e., Nile outflow is affecting stratification and productivity). Even though these drivers are indistinguishable, the correlation between Ba/Rb and Mo/Rb suggests that surface water productivity and sediment anoxia are coupled in time and through time at the core site. The sapropel S5 record of core LC21 shows an interruption estimated at $\sim 122\ ka$ (Rohling et al., 2006, 2015, and further references therein), which we do not find, as exemplified by our Mo/Ti record. Core LC21 was recovered from the Aegean Sea, closer to a deep water formation site then core 64PE406-E1, potentially making the sediment at the site of core LC21 more sensitive to perturbations. Furthermore, core LC21 is shallower (at $1,520\ m$ depth) and therefore more susceptible to record reventilation events. Still, our data do not allow fully excluding such a weakening in core 64PE406-E1, as the drop in the Ba/Ti record does hint at a period with slightly lower productivity values toward the end of the record, with concurrently also a dip in Mo/Ti, which thus suggests less reducing conditions.

By aligning our Ba/Ti record with the LC21 Ba record, we assume synchronous productivity variability throughout the Mediterranean Sea, within uncertainties. Marino et al. (2007) suggest that anoxia at the site of LC21 developed ∼100-300 years earlier when compared to an open Mediterranean Sea core (OPD971). However, within age model uncertainties at the sapropel boundaries (2 kyr), the influence of this type of nonsynchronous developments are relatively insignificant, as this would imply an additional uncertainty of approximately 3% in the total length of the sapropel. Moreover, we aligned our record using the barium record, which is not assuming a synchronous development of anoxia but productivity during the same period. While it needs to be seen that such developments are absolutely synchronous, we conclude that there is no indication that this is an issue for our analysis.

2.4.3 Multicentennial paleo-environmental variability during sapropel S5 and removal of the time-depth distortion

The first-order age model (Figure 2.3 and section 4) assumes a constant sedimentation rate for sapropel S5, as no radiometric dates are available within sapropel S5 (and there is no evidence that intrasapropel variability occurs time-synchronous basin wide). Hence, there is need for an independent age model that removes time-depth distortions in the core at a sufficiently high resolution. The first-order age model showed several significant spectral peaks in the power spectrum, and the wavelet transform shows that these frequencies appear to vary through depth (Figure 6). Hence, we subsequently tuned the age model as to achieve constant frequencies throughout the sapropel, allowing deviations from a constant sedimentation rate. The minimum change in sedimentation rate needed to obtain constant frequencies corresponds to a maximum offset (in the middle of the sapropel) of 1.5 *kyr* from the original linear age model, which is within the uncertainty of the sapropel boundaries (Grant et al., 2016, report uncertainties 2σ of $2.0 \pm 0.9kyr$ for the 40- to 150-ka BP interval). The new age model results from the hypothesis that a significant, constant frequency spectrum exists in the time domain. Still, we here refrain from speculating on a specific driving mechanism, or linkages to specific frequencies present in the signal, but rather present the methods as such to allow using the internal changes in sedimentation rate, irrespective of the frequencies present.

By adding a single pointer to the age model within the sapropel, a low frequency peak of around 650 years becomes constant throughout the sapropel. However, with this age model, higher frequency components are not constant. By adding additional pointers, all observed spectral components can be made much more stable during sapropel S5 (Figure 7a). A spline interpolation is used between these pointers, to prevent abrupt changes in sedimentation rate. The amplitude of the spectral peaks in the global wavelet is a measure for the stability of the frequency components: When the frequencies are less constant through time, more power will accumulate between peaks. The global wavelet of the first age model (Figure 6c) shows much less contrast between the peaks compared to the global wavelet of the tuned age model (Figure 2.7C). This suggests that the tuned age model provides an appreciable improvement, when assuming spectral simplicity.

When a pointer in the tuned age model is shifted by more than 100 years, the frequency content becomes significantly less constant. This indicates that tuning errors

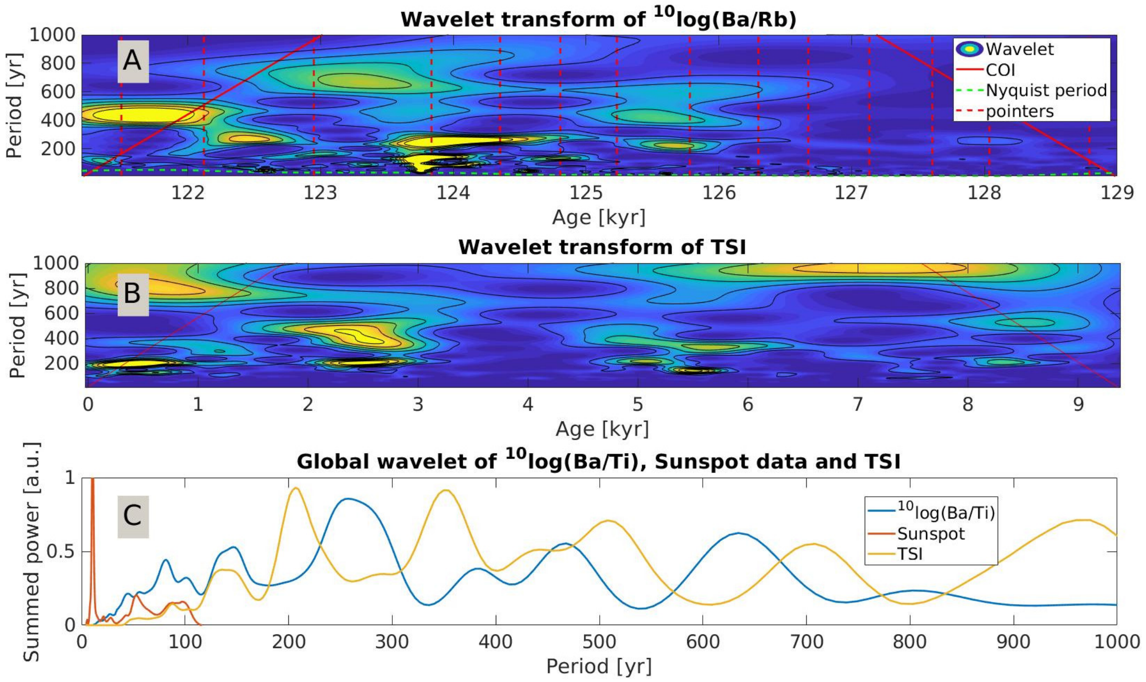

Figure 2.7 (A) The wavelet transform of the element log ratio of Ba/Rb with the tuned age model, with a central wave number of 8. The dashed green line indicates the local spatial Nyquist period, corresponding to the minimal observable period when time-depth distortions are present (Herbert, 1994). The solid red line indicates the cone of influence (COI) of the wavelet transform. (B) A wavelet transform of the total solar irradiance (TSI), using the same wavelet settings. Although the signals originate from different time intervals, their frequency-time behaviour has similarities as shown in the wavelet transforms. (C) The Br/Rb global wavelet using the tuned age model, compared to global wavelets of TSI (Steinhilber et al., 2012) and sunspot data (SILSO, 2018). Most peaks of the Br/Rb global wavelet have corresponding peaks in either the sunspot data or the TSI data. A central wave number of 12 was used for the TSI and XRF data (providing more frequency resolution), while a central wave number of 6 is used for the sunspot data.

are at most 100 years and do not significantly contribute to the overall error in the frequency content. The uncertainty in the time domain is related to the uncertainties of the dating of the core LC21 and, hence, are in the order of $2 \pm 0.9kyr$ over sapropel S5 (Grant et al., 2016). Each of the frequency components therefore also has an uncertainty proportional to the uncertainty in sapropel duration.

Possible forcing mechanisms for multicentennial climate variability include, but are not restricted to, solar variability, North Atlantic Oscillation, and the El Niño-Southern Oscillation. Solar variability is characterized by distinct spectral components, at least during the Holocene (i.e. Dykoski et al., 2005; Wang et al., 2005). The North Atlantic Oscillation has been considered as a driving mechanism but does not contain distinct frequency components and behaves as blue noise (i.e., noise with reduced high frequency components Cook et al., 2002). The El Niño-Southern Oscillation may also have affected sapropel formation through monsoon and in particular Nile outflow variability, since frequencies similar to those found in El Niño-Southern Oscillation records are recognized in the Nile high water anomaly record (Kondrashov et al., 2005). However, these frequencies are much higher than the Nyquist frequency of the sapropel S5 XRF record and can therefore not be detected. To validate potential impact of solar variability as a driving mechanism, we compare its frequency content to that of the sapropel S5 XRF record (section 5.4) We indeed observe an overall similar frequency content, although this does not necessarily imply causality. For instance, throughout the Holocene, it has been suggested that solar forcing affects the El Niño-Southern Oscillation (Marchitto et al., 2010), which in turn may affect the African monsoon.

2.4.4 High-frequency climate signals in the sapropel S5

The tuned age model removes time-depth distortion from the signal and therefore allows us to compare the spectral content of intrasapropel variability to other records. An important mechanism proposed for the variability within the most recent sapropel (S1) is solar activity (Hennekam et al., 2014; Jilbert et al., 2010). Rohling et al. (2002) already proposed solar activity as a driver for variability within sapropel S5, although no clear mechanism was given at that time. The $\sim 88 - year$ periodicity found here (in Ba/Rb) was also observed before in both a Nile high water anomaly record (Ruzmaikin et al., 2006) and total solar irradiance (TSI)/sunspot records (Steinhilber et al., 2012, and the Sunspot Index and Long-term Solar Observations (SILSO, 2018), respectively). Therefore, it seems that solar activity affects monsoon intensity, which in turn affects Nile discharge, also when overall Nile discharge is much higher. Even when increased Nile discharge due to precession variability causes an overall increase in productivity and oxygen drawdown in the Mediterranean, superimposed changes are still observed. Furthermore, Duan et al. (2014) showed how the Asian Monsoon activity is modulated by changes in solar activity, with monsoon variability most likely forced by the cosmic ray flux and associated changes in cloud cover. In addition, reduced solar output is thought to weaken the thermal contrast between ocean and continent or between hemispheres, reducing monsoon circulation and associated rainfall (Wang et al., 2017; Yan et al., 2015). The Nile river discharge may also be affected by Atlantic Meridional Overturning Circulation (AMOC) slowdown or shutdown, like during the last glacial stadials and Heinrich events (Broccoli et al., 2006; Wang et al., 2005), as millennial-scale AMOC variability has been found during MIS 5e (e.g. Oppo et al., 2001). However, clear spectral peaks in the frequency band relevant to this study (periods of 70-1,000 years) have not been reported in these records. We therefore conclude that while AMOC variability may have affected Nile outflow during sapropel S5, it cannot explain the variability observed in this study.

Several dominant frequencies have been observed in the reconstructed total solar irradiance over the past 9 kyr, such as 210 (the Suess cycle), 350 and 710 years (Steinhilber et al., 2012). However, similar solar cycles have not yet been identified as far back in time as sapropel S5. In order to explore solar cycles as a forcing mechanism for intrasapropel variability, we compare the frequency content of our XRF data to that of the TSI (Steinhilber et al., 2012) and the more recent sunspot number data (SILSO, 2018, which has yearly resolution). The same wavelet analysis has been performed on all data sets. A direct comparison between the wavelet transforms of Ba/Rb and TSI (Figure 2.7A and B) shows similar periodicities at high frequencies and similar patterns in relative intensity at lower frequencies. The sunspot data cover the last 300 $years$ and can therefore only be used for periods shorter than 200 $years$. The TSI has a length of $9,000$ $years$, comparable to the duration of sapropel S5, with a sampling interval of 22 $years$. The TSI can hence be used for periods longer than 44 $years$. The intensity of the dominant frequencies in the TSI data vary over time (Steinhilber et al., 2012) but not in frequency. Most frequencies correspond to TSI and sunspot periodicities within error (approximately 20%); however, we refrain from adjusting the age model based on this, as also other causes for high-frequency variability exist. The similarity of the frequencies observed, as well as the stability of the frequencies observed, supports our initial assumption of constant frequency components. Note that shorter quasi-cycles, such as those with ~ 11 (sunspot or Schwabe cycles) and ~ 22 (Hale cycles) $year$ periodicities cannot be observed in our record, as the temporal resolution is insufficient.

Relative power of the spectral peaks in the XRF, TSI and sunspot data differs significantly, which is expected since relative power is not constant through time in the TSI data either (Figures 2.7B and C). Moreover, it is highly unlikely that processes affecting the proxy records in the different frequency domains are linearly related to the driving forces. More importantly, the patterns of the intensity of the different frequencies in the wavelet plot (Figures 2.7A and B) are similar. We hence conclude that the time-frequency spectra of the records support the hypothesis that intra-sapropel S5 variability is related to solar cycles.

As consequence of the internal tuning of the age model, with the aim to remove time-depth distortions, sedimentation rates within the sapropel is constrained (Figure 2.8A). The derived sedimentation rates closely resemble the monsoon intensity reconstruction as derived from residual LC21 $\delta^{18}O$ (Grant et al., 2016). This record shows a steep increase toward maximum monsoon intensity, after which gradual decline of monsoon strength is observed. A link between climate and sedimentation rate has been proposed by Schiffelbein and Dorman (1986), who used a very similar criterion, "spectral simplicity." Still the pattern deviates from that found in the Nile delta for sapropel S1 (Hennekam, 2015). This difference may be due to the fact that the record used here is from a more distal location, whereas the Nile delta record is affected directly by the local sedimentary system, where magnitude response and phase response may be very different. Sea level might be an important factor to explain this difference, as it can have a large effect on sedimentation, especially during sapropel S1. Whereas a sea level change would decrease the local sedimentation rate (i.e., the site becomes more distal during sea level rise) during S1, sedimentation rate would go up during the early stage of S5 (monsoon only) as at the onset of sapropel S5 the peak in monsoon intensity was much higher than during S1 (Grant et al., 2016; Rohling et al., 2004).

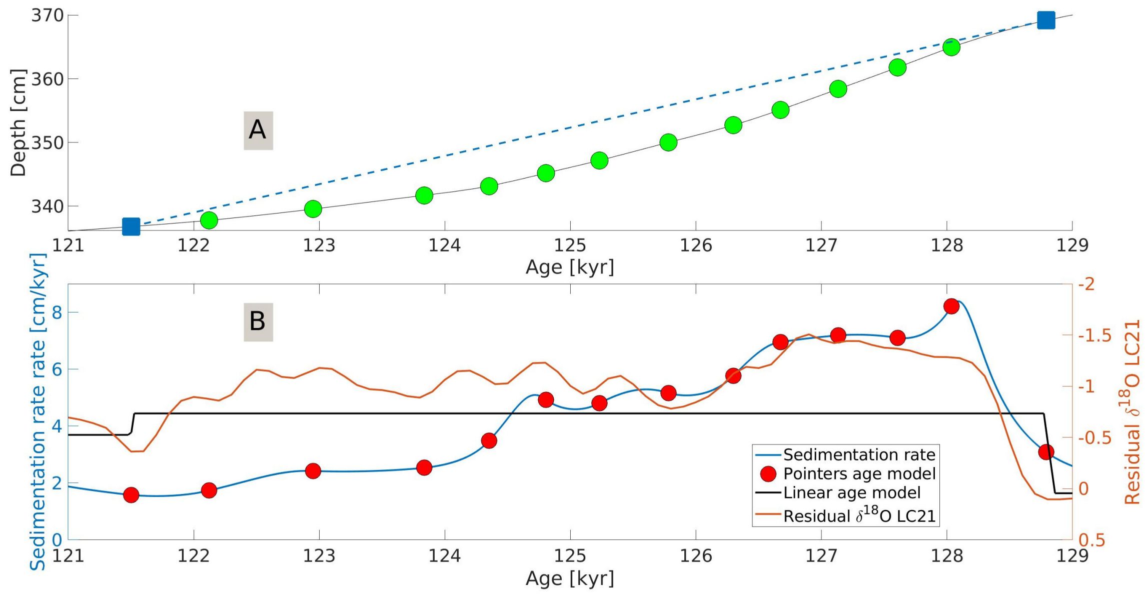

Figure 2.8 (A) The final age-depth relation (solid line, the dots represent the pointers), compared to the linear age model (dashed line). (B) The sedimentation rate in sapropel S5 (~129-121 ka) resulting from the tuned age model (blue line with the red dots), with the sedimentation rate from the untuned, linear age model for comparison (black line). Note the higher sedimentation rate at the start of the sapropel in the tuned age model. Due to the high number of control points in S5, a spline interpolation is more appropriate than a linear interpolation, which would result in abrupt steps in sedimentation rate at each pointer. Consequently, the sedimentation rate changes smoothly between the pointers. The orange line shows the residual $\delta^{18}O$, derived from core LC21 (Grant et al., 2012).

2.5 Conclusions

We propose a novel method to remove time-depth distortions on a multicentennial scale, by assuming so-called spectral simplicity, and apply this method to sediments from the Eastern Mediterranean Sea that record the anoxia event (sapropel S5) during the Eemian. A small shift in tuning ages (within age model uncertainty), and thus sedimentation rate, is sufficient to stabilize all spectral components during sapropel S5. This allows to assess the multicentennial climate variability in our proxy records for productivity and anoxia, related to sapropel S5 formation, with more certainty. The resulting signal showed similarity to several records of solar activity from the Holocene, both in frequency and amplitude variability. Hence, we conclude that intrasapropel variability, at least during sapropel S5, seems to be linked to solar variability through Nile outflow. Moreover, this suggests that multicentennial climate variability that affected sapropel formation during the Holocene and the "warmer-than-preindustrial" Eemian behaved in a similar way.

Our age model, which removes time-depth distortions, also allows us to study the sedimentation rate in unprecedented detail. The early phase of sapropel S5 was characterized by an intensified Nile outflow. The sedimentation rates during this phase, calculated from the age model are found to be higher. After this initial peak, the derived sedimentation rate gradually decreases again, similar to the reduction in Nile discharge that has been reconstructed. Hence, the monsoon intensity and sedimentation rate at the core location were probably linked during sapropel S5.

3 The mechanism of sapropel formation in the Mediterranean Sea: insight from long-duration box model experiments

Based on: Dirksen, J. P., & Meijer, P. (2020). The mechanism of sapropel formation in the Mediterranean Sea: insight from long-duration box model experiments. *Climate of the Past*, 16(3), 933-952.

Abstract

Periodic bottom water oxygen deficiency in the Mediterranean Sea has led to the deposition of organic rich sediments during geological history, so called sapropels. Although a mechanism linking the formation of these deposits to orbital variability has been derived from the geological record, physics-based proof is limited to snapshot and short time-slice experiments with (Oceanic) General Circulation Models. Specifically, previous modelling studies have investigated atmospheric and oceanographic equilibrium states during orbital extremes (minimum and maximum precession). In contrast, we use a conceptual box model that allows us to focus on the transient response of the Mediterranean Sea to orbital forcing and investigate the physical processes causing sapropel formation. The model is constrained by present day measurement data, while proxy data offers constraints on the timing of sapropels.

The results demonstrate that it is possible to describe the first order aspects of sapropel formation in a conceptual box model. A systematic model analysis provides new insights on features observed in the geological record, such as timing of sapropels, intra-sapropel intensity variations and interruptions. Moreover, given a scenario constrained by geological data, the model allows us to study the transient response of variables and processes that cannot be observed in the geological record. The results suggest that atmospheric temperature variability plays a key role in sapropel formation, and that the timing of the midpoint of a sapropel can shift significantly with a minor change in forcing due to nonlinearities in the system.

Picture left: Sunset in the Ionian basin, taken from the RV Pelagia on cruise 64PE-406-E in January 2016. This is the basin where most deep water is formed.

3.1 Introduction

3.1.1 Background

The response of ocean circulation to changes in atmospheric forcing is an important element of the climate system. Using computer models applied to the geological past we can exploit the sedimentary record of variation in circulation for mechanistic insight. The Mediterranean Sea is of particular interest, as abundant and exceptionally well dated proxy data and present-day measurement data is available and it is a basin that displays processes such as thermohaline circulation and gateway control that play a role on the global scale as well.

Presently, the Mediterranean Sea is an evaporative basin (Romanou et al., 2010) with a small annual mean heat loss to the atmosphere (Song and Yu, 2017). Water from the Atlantic flows in to the Mediterranean Sea at the Strait of Gibraltar and is then subjected to buoyancy loss due to evaporation and cooling (see Fig. 3.1 for a map of the Mediterranean Sea). This results in the formation of intermediate water in the Levantine basin which spreads throughout the basin (Hayes et al., 2019; Wu and Haines, 1996). During winter, in the northerly parts of the basin, situated at relatively high latitude, cold and dry winds induce a further density increase, which may lead to the formation of deep water (Schroeder et al., 2012). Specifically, deep water formation (DWF) occurs over the shallow northern Adriatic Sea (Malanotte-Rizzoli, 1991) and the Aegean Sea (Gertman et al., 2006; Roether et al., 1996) and in the form of open-ocean deep convection in the Gulf of Lion (Marshall and Schott, 1999) and the southern Adriatic Sea (Bensi et al., 2013). Dense water formed in the Adriatic and Aegean Seas, both marginal basins of the Mediterranean Sea, flows out over the seafloor into the deeper parts of the main basin.

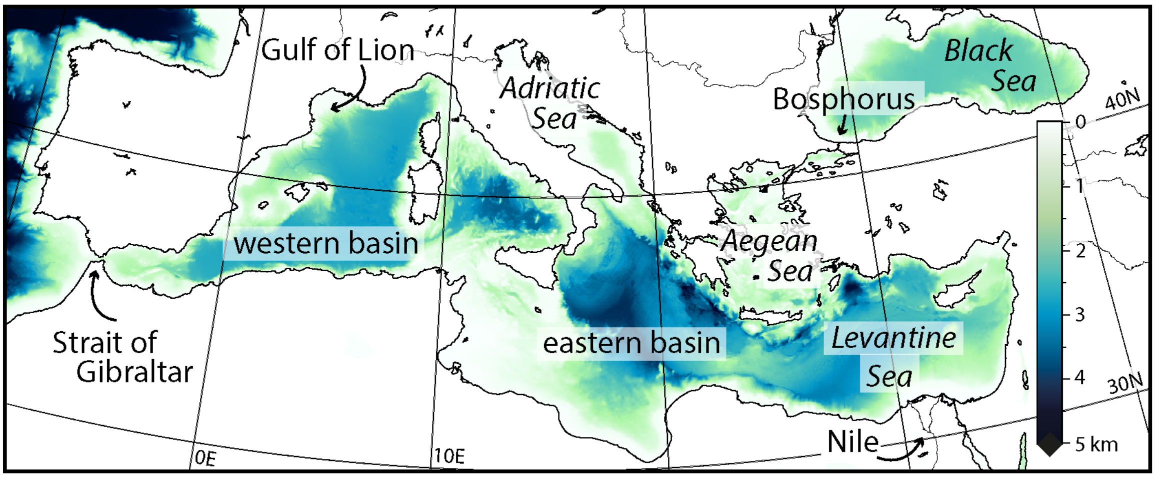

Figure 3.1 Map of the Mediterranean Sea. The bathymetry shown is part of the GEBCO 2014 Grid. The colours indicate water depth.

The basin's semi-enclosed nature causes the system to be very sensitive to climatic perturbations and the geological record holds an expression of this sensitivity in the form of the regular occurrence of organic rich deposits, known as sapropels (Rossignol-Strick, 1985; Rohling et al., 2015; Hilgen, 1991; Lourens et al., 1996; Cramp and O'Sullivan, 1999). Sapropels are thought to form when Nile discharge increases as a response to enhanced African summer monsoon activity during precession minima (Rossignol-Strick, 1985; Rohling et al., 2015). The low density fresh water then forms a lid at the surface, stopping or reducing the strength of the overturning circulation. This commonly accepted mechanism can be nuanced by noting that the Nile does not enter the basin at a DWF site, but rather close to the location where intermediate water forms. A large part of the DWF involves this intermediate water (Schroeder et al., 2012). Reducing the density of the intermediate water implies a decrease or absence of a (positive) vertical density gradient, also diminishing or stopping the formation of deep water. In contrast, runoff into the marginal basins directly affects the buoyancy at the DWF sites. For deep convection in for example the Levantine basin (which can happen with present day conditions, Gertmann et al., 1994) a decrease in surface water density directly decreases or stops DWF. With decreasing DWF, the supply of oxygen to the deep water diminishes, potentially causing anoxia and the preservation of organic matter in the Eastern Mediterranean Sea. Moreover, nutrient input increases with river outflow as well, thereby affecting primary production, export of organic carbon to the deep water and, consequently, oxygen consumption (Calvert et al., 1992; De Lange and Ten Haven, 1983; Thomson et al., 1999; van Helmond et al., 2015; Weldeab et al., 2003). Sea level rise may also trigger sapropel formation (see Rohling et al., 2015, for sapropel S1), although this does not exclude monsoon intensity variability as the main cause.

In this paper we present a simple three box model of the Mediterranean Sea, which includes most elements commonly invoked to explain sapropel formation as described above. With the model we study which processes determine when and why sapropels form the way they do. Our aim is to gain a new perspective on the timing of the sapropel, relative to the forcing, as a significant part of the geological time scale depends on this relation (Hilgen et al., 1995; Krijgsman et al., 1999) and views on the timing of the midpoint (the average of the top and bottom age) are contested in more recent publications (Channell et al., 2010; Westerhold et al., 2012, 2015). A low complexity model allows us to perform many long runs and explore the parameter space to a much greater extent than high complexity models. The runs described in this paper represent but a small fraction of the experiments that have been conducted and were chosen to give an overview of the behaviour of the model. Long runs are necessary to study the transient response of the system over a full precession cycle.

As described in modelling studies (such as Marzocchi et al., 2015) as well as in observational studies (for example Herbert et al., 2015), surface air temperatures have also been found to vary over a precession cycle, where precession minima are estimated to have been $1 - 3$ $°C$ warmer (annual average) than precession maxima. Since heat loss depends on the temperature difference between the water surface and atmosphere, this is another factor that decreases buoyancy loss during precession minima. We will examine the relative importance of this effect by running the model both with, and without atmospheric temperature variability.

3.1.2 Previous modelling studies

Just like the Last Glacial Maximum, the time of sapropel formation has been recognized early on in the application of OGCMs to Mediterranean circulation, as a configuration that makes for an interesting contrast to the present-day state (Bigg, 1994; Myers et al., 1998; Myers and Rohling, 2000; Myers, 2002; Meijer and Tuenter, 2007; Meijer and Dijkstra, 2009); and more recently, using a regional ocean model forced by output from a dedicated global climate model experiment, (Mikolajewicz, 2011; Adloff et al., 2011). Several studies have explored the coupling of circulation models to models of the biogeochemical cycling, first offline and then in truly combined fashion (Stratford et al., 2000; Bianchi et al., 2006; Grimm et al., 2015). All these studies have in common that they are limited to time spans much shorter than the precessional cycle. The only previous box models related to the sapropel problem are those by Matthiesen and Haines (2003) and Amies et al. (2019), but these models lacks a representation of the deep waters of the basin. The aforementioned studies offer support for the basic idea that freshening of the surface waters leads to reduction of the overturning circulation. The studies suggest that it is important to consider the full fresh water budget and that runoff may have varied significantly on orbital time scales (Bigg, 1994; Amies et al., 2019). Finally, nutrient supply is found be a significant factor in the formation of sapropels (Stratford et al., 2000; Bianchi et al., 2006).

3.2 Methods

3.2.1 Model set-up

The Mediterranean Sea is represented by three boxes in our model: the high latitude marginal basins (intermediate and surface water, box 1, representing the Adriatic and Aegean Seas and the Gulf of Lion), the open Mediterranean (surface and intermediate water, box 2) and the deep water (box 3) (see Fig. 3.2). Boxes 1 and 2 have fluvial input (sourced from boxes R_1 and R_2, see Fig. 3.2) and exchange with the atmosphere (represented by boxes A_1 and A_2, see Fig. 3.2). The surface forcing is further explained in subsection 3.2.2. Each box has its own temperature and salinity. Boxes 1 through 3 are dynamic: the temperature, salinity and density is calculated during each time step, based on the incoming and outgoing salt and heat. The Atlantic, both rivers and both parts of the atmosphere can be seen as static boxes: their salinity, temperature and density are constant.

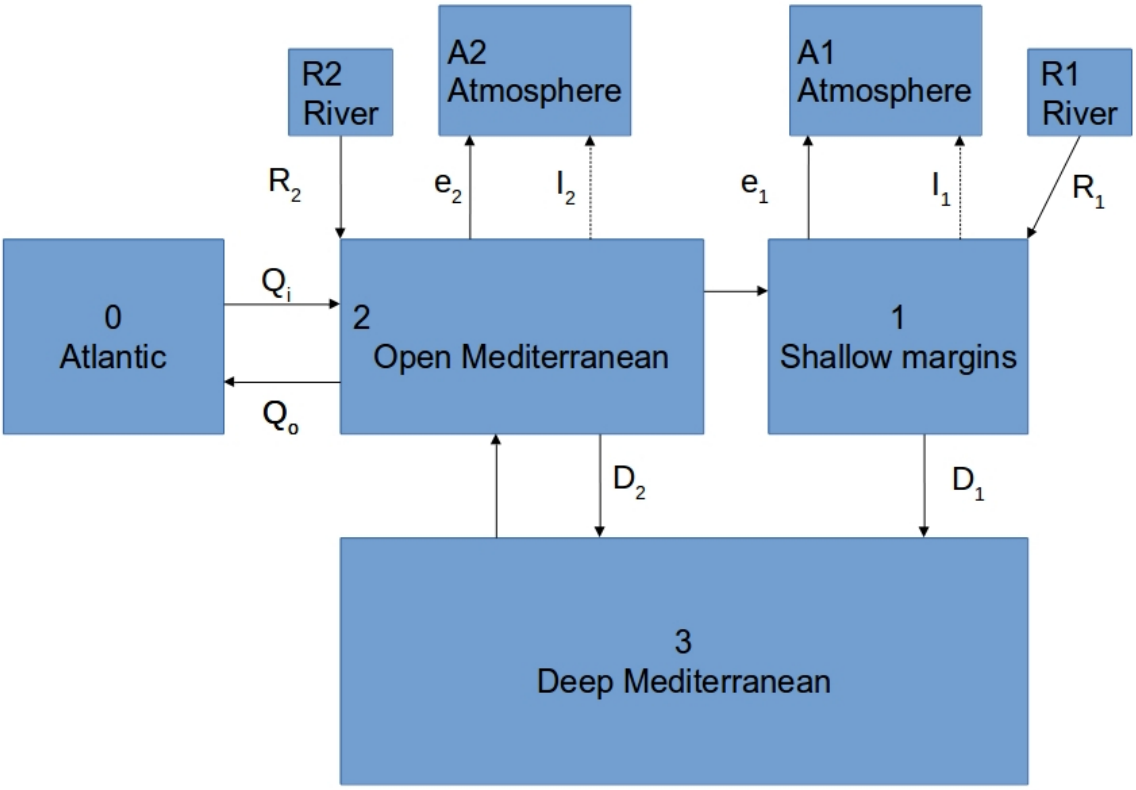

Figure 3.2 A schematic overview of the model set-up. The unlabelled fluxes are balancing fluxes, the equations for all fluxes are given in subsection 3.2.3. The direction of the arrows indicates the positive direction in the equations, all horizontal fluxes can change direction.

Circulation is modelled by including downward, vertical fluxes, of which the magnitude depends on the density difference between the surface/intermediate layer and the deep water (D_1 in box 1 and D_2 in box 2 in Fig. 3.2). This DWF is driven by buoyancy loss, due to net evaporation (E-P, where E is the evaporation and P precipitation, e_1 and e_2 in Fig. 3.2) and heat exchange with the atmosphere, which is modelled as a relaxation (i.e. the surface water temperature relaxes to the temperature of the associated atmosphere box, fluxes I_1 and I_2 in Fig. 3.2). Note that the DWF in box 1 captures the behaviour of the marginal basins of the Eastern Mediterranean sea, but is also an approximation of the open ocean convection in the Gulf of Lion (see subsection 3.1.1). In the typical situation that the Mediterranean surface/intermediate water at the Strait of Gibraltar is more dense than the Atlantic water and E-P-R (the fresh water budget, where R is the total runoff) is positive, it is the outflow to the Atlantic (Qo in Fig. 3.2) that depends on the density difference between the adjacent water masses. The inflow into the Mediterranean Sea is then the sum of the outflow to the Atlantic and the fresh water budget. The equations used in the model are further explained in subsection 3.2.3. In addition to the water fluxes, diffusive mixing is also included in the model. In contrast to the water fluxes, no net water transport occurs as a result of the mixing. Rather, properties are exchanged between adjacent boxes. The amount of horizontal mixing (between the upper boxes) is constant, while the vertical mixing is a function of the density difference between the boxes in question.

A first order approximation of deep water oxygen concentration is included in the model to get a better understanding of when oxygen deficiency occurs. The oxygen concentration of the upper boxes is assumed to be in equilibrium with the atmosphere and is therefore constant. The oxygen concentration of the deep water (box 3) depends on the deep water fluxes, mixing and oxygen consumption. Oxygen consumption is scaled with river outflow, as a first order approximation of the nutrient input, and oxygen concentration. The use of constant volume for the boxes implies (i) that we take there to always be a distinction between surface/intermediate and deep cell, and (ii) that the upper cell always extends to the same depth. The upper cell appears to be set up by the exchange with the ocean (see Meijer and Dijkstra, 2009, for the Mediterranean Sea and Finnigan et al., 2001, for a generic buoyancy-driven marginal sea) and is likely a persistent feature of Mediterranean circulation as long as there is an exchange flow. Moreover, starting from a state that does have DWF and a separate deep cell, OGCM experiments of reduced net evaporation show a halting of deep circulation while keeping the upper cell more or less in place (Meijer and Dijkstra, 2009).

In the present-day Mediterranean Sea DWF is the last step in a chain of processes (see the introduction). Our model does not include the intra-annual variability, and the basin geometry is only represented in abstract form. However, in the sense that the model does capture both the effect of salinity increase and temperature decrease on upper-water density it is expected to form a fair representation, qualitatively speaking, of the essence of the overturning circulation. To which extent this is true will have to follow from more advanced models. Note that the model of Matthiesen and Haines (2003) also neglects the seasonal cycle. During winter, convection occurs (Schroeder et al., 2012) and the depth of the intermediate water is relatively stable. We therefore abstract the circulation to an open surface/intermediate box, a marginal surface/intermediate box and a deep water box, all with constant volumes. While the formation of deep water itself is a seasonal process, we parametrize the seasonal variability by calculating an annually averaged DWF flux. We know that DWF occurs every year during present winters. However, deep water would not form with annual average conditions and therefore we assume perpetual winter conditions.

3.2.2 Surface forcing

The transient response of circulation and water properties to precession induced climate change is modelled by altering the evaporation and river outflow for each box at every time step. The analyses presented in this paper all use sine-waves to force the model, but any temporal variation could be used, such as that of the insolation curve. To be precise, the model forcing used in this paper is derived from a normalized sine-wave with a 20 kyr period, to reflect climatic precession. The amplitude and offset is then altered for evaporation and fluvial discharge in boxes 1 and 2. The phase of

Table 3.1 All model parameters, excluding the model forcing.

Name	Value	Units	Description
dt	1	yr	Time step
c_A	1.5	$W/(m^2 \cdot K)$	Sea to air heat transport efficiency
c_{13}	$1 \cdot 10^6$	$m^6 s^{-1} kg^{-1}$	Water transport efficiency between box 1 and 3
c_{23}	$4 \cdot 10^6$	$m^6 s^{-1} kg^{-1}$	Water transport efficiency between box 2 and 3
c_{20}	$3.9 \cdot 10^5$	$m^3/s/\sqrt{kg/m^3}$	Water transport efficiency at the Strait of Gibraltar
k_{12}	$1 \cdot 10^{-4}$	m^2/s	Horizontal mixing between box 1 and 2
L	1000	m	Length scale of horizontal diffusivity
k_{bg}	$4 \cdot 10^{-5}$	m^2/s	Background vertical mixing strength
k_{str}	$3.5 \cdot 10^{-4}$	$m^5/(kg \cdot s)$	Vertical mixing strength/rho grad.
A	$2.5 \cdot 10^{12}$	m^2	Surface area of the Mediterranean
f	0.2	$-$	Fraction of the surface area covered by box 1
d_1	500	m	Depth of box 1
d_2	500	m	Depth of box 2
d_3	1000	m	Depth of box 3
S_0	36.2	kg/m^3	Salinity of the Atlantic ocean
T_0	15	$°C$	Temperature of the Atlantic ocean
T_{R1}	16	$°C$	Temperature of R_1
T_{R2}	18	$°C$	Temperature of R_2
O_1	230	uM	Surface water O_2 concentration
Oc_O	$1.1 \cdot 10^{-3}$	s^{-1}	Oxygen consumption parameter
Oc_R	$1.8 \cdot 10^{-7}$	m^{-3}	Oxygen consumption due to river outflow
c_p	$4.187 \cdot 10^3$	$J/(K \cdot kg)$	Specific heat of water

evaporation relative to the precession forcing is uncertain (see subsection 3.3.4) and is therefore varied between runs, the phase of the river discharge is kept at 0 degrees.

The fluvial discharge in box 2 (R_2) is interpreted as the Nile outflow and other runoff from Africa. Prior to the construction of the Aswan High Dam in 1964, average Nile discharge was $2.7 \cdot 10^3$ m^3/s (Rohling et al., 2015). Present day runoff from Africa is approximately $1.4 \cdot 10^3$ m^3/s (Struglia et al., 2004). A recent modelling study (Amies et al., 2019) suggests that peak runoff from Africa may have been up to 8.8 times larger than present during sapropel S5. Note that their study does not consider changes in outflow from Europe. Fluvial discharge in to the high latitude marginal basins of the Mediterranean Sea (R_1 in the model) is presently approximately $6.7 \cdot 10^3$ m^3/s (Struglia et al., 2004) . Increased runoff from Europe into the eastern Mediterranean has been proposed as a possible source for extra fresh water during precession minima (Rossignol-Strick, 1985; Rohling et al., 2002; Scrivner et al., 2004) The current net evaporation (E-P) is approximately 0.9 m/yr (Romanou et al., 2010). During sapropel times, net evaporation is hypothesized to have decreased (Rohling, 1994), although this has not been quantified. We therefore test a broad range of net evaporation, from 0.2 to 2 m/yr to accommodate for these uncertainties.

3.2.3 Model equations and parameters

Here we first discuss the flux equations resulting from the model set-up and assumptions described above, followed by the equations used to integrate all flux-equations into a fully functioning model. All parameters are given in Table 3.1. We use a matrix vector representation to calculate the temperatures, salinities, densities, oxygen concentration of the next time step. The (water and heat) flux magnitudes and mixing intensities define the elements of the matrices used for these calculations. This same matrix-vector representation could be used for an arbitrary configuration (and number) of boxes, to represent different oceanographic settings. Observational and modelling studies (Herrmann et al., 2008; Schroeder et al., 2012) have shown that during colder winters, more deep water is formed. Hence, it makes sense that the magnitude of the vertical, downward fluxes (D_1 and D_2, see Eqs. 3.2 and 3.3) depends on oceanographic (and thereby indirectly also atmospheric) conditions. The most simple way of implementing this behaviour on a yearly resolution, is to assume a linear relationship between the density difference and flux magnitude (similar to Matthiesen and Haines, 2003). When the density of the overlying water mass is smaller than that of the deep water, the water column is stratified and no vertical flux exists. To clip negative components of a flux to 0, we use the form $F_{j,i} = max(0, a)$, where a is the flux in question. We therefore define the following mathematical operator:

$$max(a, b) = \begin{cases} a & \text{for} \quad b \leq a \\ b & \text{for} \quad b > a \end{cases} \tag{3.1}$$

The proportionality of DWF to surface to deep water density difference is determined by an efficiency constant, c_{13} and c_{23} for D_1 and D_2 respectively. The magnitude of these constants is chosen in such a way that a realistic deep water flux occurs at a present-day density difference. In the current circulation deep convection in the Levantine basin (represented by D2) does not occur every year (Gertman et al, 1994; Pinardi et al., 2015), making it difficult to determine c_{23} empirically. By assuming that the DWF process in box 2 is the same as in box 1 (i.e. linearly dependent on the vertical density difference), c_{23} can be taken as 4 times larger than c_{13}, proportional to the difference in surface area of boxes 1 and 2. We therefore define the DWF fluxes in Eqs. 3.2 and 3.3, where ρ_1, ρ_2 and ρ_3 are the densities of boxes 1 to 3 respectively.

$$D_1 = max(0, c_{13} \cdot (\rho_1 - \rho_3)) \tag{3.2}$$

$$D_2 = max(0, c_{23} \cdot (\rho_2 - \rho_3)) \tag{3.3}$$

At the Strait of Gibraltar, the exchange has two components from which the in- and outflow is calculated (see equations below): a density driven flux Q_o (Eq. 3.4) and a compensating flux Q_i (Eq. 3.5). The magnitude of Q_o has a square-root relation to the horizontal density difference at the strait (where ρ_0 is the density of the Atlantic ocean), in accordance with Bryden and Kinder (1991) . Theoretically, this flux should be able to change direction, when the density difference changes sign. We therefore multiply the square-root of the absolute value of the density difference with the sign of the density difference. Note that the direction of the fluxes (i.e. whether it goes in or out of the Mediterranean Sea) is determined in Eqs. 3.11 and 3.10. The strait efficiency c_{20} (the coefficient of proportionality between volume transport and density difference) is again calibrated on present-day conditions (Schroeder et al., 2012; Jordà et al., 2017; Hayes et al., 2019). The compensating flux Q_i can then be calculated as the difference of Q_o and the total freshwater budget of the Mediterranean Sea, to allow for conservation of volume.

$$Q_o = \begin{cases} -c_{20} \cdot \sqrt{|\rho_2 - \rho_0|} & \text{for} \quad \rho_2 \leq \rho_0 \\ c_{20} \cdot \sqrt{|\rho_2 - \rho_0|} & \text{for} \quad \rho_2 > \rho_0 \end{cases} \tag{3.4}$$

$$Q_i = Q_o - R_1 - R_2 + e_1 + e_2 \tag{3.5}$$

The equations above describe all fluxes driven by gradients. By combining these fluxes with the surface forcing, we can derive the other fluxes by assuming constant box volume. The next set of equations (Eq. 3.6-3.16) define elements of a matrix $\mathbf{F}$, representing all water fluxes.

$$F_{1,A1} = e_1 \tag{3.6}$$

$$F_{2,A2} = e_2 \tag{3.7}$$

$$F_{R1,1} = R_1 \tag{3.8}$$

$$F_{R2,2} = R_2 \tag{3.9}$$

$$F_{2,0} = max(0, -Q_i) + max(0, Q_o) \tag{3.10}$$

$$F_{0,2} = max(0, Q_i) + max(0, -Q_o) \tag{3.11}$$

$$F_{2,1} = max(0, F_{13} - F_{R11} + F_{1A1}) \tag{3.12}$$

$$F_{1,2} = max(0, -F_{13} + F_{R11} - F_{1A1}) \tag{3.13}$$

$$F_{1,3} = D_1 \tag{3.14}$$

$$F_{2,3} = D_2 \tag{3.15}$$

$$F_{3,2} = D_1 + D_2 \tag{3.16}$$

Mixing has a major impact on oceanic circulation, and must therefore be included in the model. Unlike the water fluxes described above, mixing does not cause a net water transport between boxes, but rather an exchange of properties (salt, heat and oxygen). In the model, we distinguish between horizontal and vertical mixing. Horizontal mixing, between boxes 1 and 2, depends on a fixed length scale over which mixing occurs and diffusivity (see Eq. 3.17). Vertical mixing (see Eq. 3.18 and 3.19) depends on the density difference between the boxes in question, where a larger density gradient causes more mixing. d_1, d_2 and d_3 in Eq 3.18 and 3.19 are the depths of boxes 1, 2 and 3 respectively and A_1 and A_2 the surface areas of boxes 1 and 2. Thereby the diffusivity of vertical mixing effectively depends on the density difference. When the water column is stratified, mixing does not stop completely, but rather decreases to a background level, representing the internal waves and other disturbances. In the model this is included by clipping the vertical mixing to a fixed level (k_{bg}) when the density gradient becomes very small or negative. Equations 3.17-3.19 define elements of a matrix **M**.

$$m_{1,2} = k_{12} \cdot L \tag{3.17}$$

$$m_{1,3} = max(k_{bg}, (\rho_1 - \rho_3) \cdot k_{str} + k_{bg}) \cdot \frac{2 \cdot A_1}{d_1 + d_3} \tag{3.18}$$

$$m_{2,3} = max(k_{bg}, (\rho_2 - \rho_3) \cdot k_{str} + k_{bg}) \cdot \frac{2 \cdot A_2}{d_2 + d_3} \tag{3.19}$$

In our model, heat exchange with the atmophere is represented by a relaxation to a prescribed air temperature (e.g. Ashkenazy et al., 2012). In a previous version of the model we used a constant flux (of 5 W/m^2), in general similar results are obtained. However, when the fresh water budget of the margins approaches zero and the circulation (almost) stops, the results are not realistic. In this situation the margins become almost completely isolated from the rest of the basin, causing a massive temperature drop that does not stop until the circulation starts again. In reality this temperature drop would be limited by the atmospheric temperature, something the relaxation representation does capture.

We thus multiply the temperature difference between the atmosphere and the water by a relaxation parameter c_A in $W/(m^2 \cdot K)$. The value of this parameter is chosen such that at present day temperatures, a heat loss to the atmosphere of approximately 5 W/m^2 occurs, in accordance with Song and Yu (2017) and Schroeder et al. (2012). In the matrix-vector representation the two relaxation boundary conditions correspond, upon the necessary conversion, to two elements of a matrix **H**.

$$H_{1,A1} = \frac{c_A \cdot A_1}{c_p \cdot \rho_1} \tag{3.20}$$

$$H_{2,A2} = \frac{c_A \cdot A_2}{c_p \cdot \rho_2} \tag{3.21}$$

Oxygen is supplied to the deep water from the surface by fluxes D_1 and D_2 (equations 3.2 and 3.3) as well as through mixing with boxes 1 and 2 ($m_{1,3}$ and $m_{2,3}$, equations 3.18 and 3.19). The oxygen concentration in boxes 1 and 2 is assumed to in equilibrium with the atmosphere and therefore constant. For the deep water, oxygen consumption depends on the oxygen concentration of the deep water and river outflow. River outflow increases oxygen consumption, while lower oxygen concentrations decrease oxygen consumption. When the deep water is completely anoxic, oxygen consumption stops as well. Other processes affecting sapropel formation, such as nutrient dynamics and increased productivity due to the development of a deep chlorophyll maximum (Rohling et al., 2015; Lange et al., 2008; Kemp et al., 1999; Rohling and Gieskes, 1989; Slomp et al., 2002; Van Santvoort et al., 1996, 1997) are not explicitly included in the model, but are to some extent parametrized by the dependence of oxygen consumption on the total river outflow (see equation 3.22). The total river outflow (R_{tot}) is defined as $R_1 + R_2$. Oxygen consumption increases linearly with river outflow as can be gleaned from Eq. 3.22 in combination with Table 3.1. Oc_R is the coefficient that, upon multiplication with the river discharge, gives the contribution to the amount of oxygen consumption related to river discharge. The constant Oc_O scales oxygen use with the oxygen concentration. Primarily, these oxygen consumption parameters are chosen to give present day deep water oxygen concentrations (close to the values found in Powley et al., 2016) under present day conditions of forcing. Furthermore, we assume that anoxic conditions can be reached in a few hundred years after stopping the circulation, in accordance with Bianchi et al. (2006). These two conditions constrain the two oxygen consumption parameters to their chosen values.

$$O_{consumption} = max(0, (Oc_O + R_{tot} \cdot Oc_R) \cdot O/dt) \tag{3.22}$$

The model parameters (excluding surface forcing) used in all runs are given in Table 3.1. Initial temperatures are set to 16 $°C$ and salinities to 37 for all dynamic boxes. They have no effect on the outcome of the model runs after spin-up. With the strait efficiency used in this paper, the model has a typical equilibrium time of less then 1000 years, while a spin-up of 20 kyr is removed from the output. The temperature in boxes 1 and 2 relaxes to both the Atlantic temperature and the air temperatures, T_0, T_{A1}, T_{A2} respectively. T_0, T_{A1}, T_{A2} therefore effectively set the temperature range of the dynamic boxes. The winter air temperatures are within the range given by the Naval Oceanography Command (1987): $10°C$ in the northwest to $15-16°C$ in the southeast. The river inflow also affects temperature, but has a much smaller impact due to the relatively small amount of water (2 orders of magnitude smaller than the Atlantic exchange). The air temperatures are chosen as winter values, since average air temperatures do not result in a realistic atmospheric heat loss and DWF. The temperature of the river water does not have a large influence on the model outcome.

The volumes of the boxes are calculated from the depth and surface area for all dynamic boxes, where $\vec{V}$, $\vec{A}$ and $\vec{d}$ are all vectors with three elements:

$$\vec{V} = \vec{A} \cdot \vec{d} \tag{3.23}$$

Except for the lack of a flux from box 3 to box 1, water can flow between all boxes in both directions. In the model, three types of fluxes exist: predefined fluxes, density driven fluxes and balancing fluxes. The predefined fluxes are used to force the model: evaporation and river discharge. The density driven fluxes are the DWF (unidirectional) and, depending on the sign of the density difference, Atlantic inflow or Mediterranean outflow. All other fluxes are of such magnitude that volume is preserved. During each time step in the model, the salinity, temperature and density for the next time step are calculated from the fluxes and mixing. In the model script, these equations are only defined for dynamic boxes, increasing the model efficiency significantly. Below the equations are given in matrix form. The volumes of static boxes are infinite, as their temperature and salinity do not change, regardless of in- and outgoing fluxes. Note that the atmosphere boxes are the last two boxes in matrix

F (boxes n and $n-1$). The matrix **G** describes the water fluxes for the calculation of the new temperature, where **I** is the identity matrix and $\vec{l}$ the unit vector.

$$\mathbf{G} = \mathbf{F} + \mathbf{I} \cdot \sum_j \mathbf{F}_{ij} \cdot \vec{l}_i \tag{3.24}$$

The matrix **P** describes the water fluxes for the calculation of the new salinity, where **J** is a matrix of ones. The only difference with **G** being that evaporation is excluded (since evaporated water does not contain salt).

$$\mathbf{P} = \mathbf{F} + \mathbf{I} \cdot (\mathbf{J}_{n,1} - (\vec{l}_n + \vec{l}_{n-1})) \cdot \sum_j \mathbf{F}_{ij} \cdot \vec{l}_i \tag{3.25}$$

The matrix **N** describes the mixing fluxes for the calculation of both the new temperature and salinity.

$$\mathbf{N} = \mathbf{M} + \mathbf{I} \cdot \sum_j \mathbf{M}_{ij} \cdot \vec{l}_i \tag{3.26}$$

$\vec{W}$ is a vector so that $W_i = \frac{1}{V_i}$. Similar to **F**, the heat fluxes (equations 3.20 and 3.21) are placed in **H**, which is of the same size as **F** and where all undefined elements are zero. We use a time step, dt, of 1 year, unless noted otherwise. Then the change in temperature for each time step equals:

$$\vec{T}(t+1) = \vec{T}(t) + (\mathbf{G} + \mathbf{N} + \mathbf{H}) \cdot \vec{T}(t) \cdot \vec{W} \cdot dt \tag{3.27}$$

and for salinity:

$$\vec{S}(t+1) = \vec{S}(t) + (\mathbf{P} + \mathbf{N}) \cdot \vec{S}(t) \cdot \vec{W} \cdot dt \tag{3.28}$$

The density for the next time step is calculated from the temperature and salinity using the EOS80 formula (on Oceanographic Tables, 1986). Note that vectors $\vec{V}, \vec{S}, \vec{T}$ and $\vec{\rho}$ include both static and dynamic boxes. The deep water oxygen concentration of the next time step is similarly:

$$\vec{O}(t+1) = max(0, \vec{O}(t) + (\mathbf{P} + \mathbf{N} - \vec{O}_{consumption}) \cdot \vec{O}(t) \cdot \vec{W}) \cdot dt \tag{3.29}$$

Note that the oxygen concentration is only calculated for the deep water (making $\vec{O}$ and $\vec{O}_{consumption}$ effectively scalars) and that the surface water boxes have a constant oxygen concentration. The equations are integrated numerically by the forward Euler method taking appropriately small time steps. The figures shown below are built up of the output at every time step.

3.2.4 Statistical analysis

One of the results of the model is that slight variations of forcing parameters can cause significantly different sapropel duration and timing. We therefore introduce a statistical test to determine the magnitude thereof, given the uncertainty of each of the forcing variables. With eleven forcing parameters (the phase of evaporation and minima and maxima of R_1, R_2, T_{A1}, T_{A2} and evaporation) it is not feasible to calculate all permutations at a meaningful resolution. We therefore randomly pick and run 200 permutations (fewer permutations would produce unreliable results), given the uncertainty of each parameter , and calculate the 1σ and minimum and maximum values of the resulting oxygen concentrations per time step (see Fig. 3.9 for an example). During testing, we can thereby visualize much more of the parameter space than when doing individual runs.

3.3 Analysis and results

3.3.1 Reference experiment

In the reference experiment the sine functions for the forcing are calibrated such that the precession maximum corresponds to present-day values—given that the orbital configuration is close to a precession maximum today. The curves are shown in Fig. 3.3A. All runs use a spin up of a full precession cycle, which is excluded from the figures and analyses; model run time T (horizontal axes) is set to 0 at the end of the spin up. All figures show an entire precession cycle, with the precession maxima falling at T=0 and T=20 kyr. The precession minimum sits at T=10 kyr. Nile outflow (R_2) increases from $5 \cdot 10^3$ to $3 \cdot 10^4$ m^3/s, while river outflow from Europe only increases from $5 \cdot 10^3$ to $1.2 \cdot 10^4$ m^3/s and evaporation decreases from 0.9 to 0.75 m/yr. While quantitative reconstructions of fluvial discharge and evaporation during sapropel formation are not available, these minimum and maximum values are in agreement with Marzocchi et al. (2015). Table 3.2 shows the ranges of the forcing parameters for all presented runs. As explained in the Introduction we choose these particular runs because they illustrate well the sensitivity of the model to the various controlling factors.

Table 3.2 The minima and maxima of the sine waves used as forcing parameters for the presented runs.

Run name	R_1	R_2	e	T_{A1}	T_{A2}
	m^3/s	m^3/s	m/yr	$\deg C$	$\deg C$
Reference	$5 \cdot 10^3 - 1.2 \cdot 10^4$	$3 \cdot 10^3 - 3 \cdot 10^4$	$0.75 - 0.9$	$10 - 10$	$12 - 12$
Temperature var.	$5 \cdot 10^3 - 1.2 \cdot 10^4$	$3 \cdot 10^3 - 3 \cdot 10^4$	$0.75 - 0.9$	$10 - 13$	$12 - 15$
fwb$_1$	$5 \cdot 10^3 - 1.4 \cdot 10^4$	$3 \cdot 10^3 - 3 \cdot 10^4$	$0.75 - 0.9$	$10 - 13$	$12 - 15$
fwb$_{tot}$	$5 \cdot 10^3 - 1.4 \cdot 10^4$	$3 \cdot 10^3 - 8 \cdot 10^4$	$0.74 - 0.9$	$10 - 13$	$12 - 15$

From Time=0 towards the precession minimum, the river outflow increases and, as a result, salinities decrease, as shown in Fig. 3.3B. After the precession minimum river outflow decreases again and salinities increase. The differences in salinity between the boxes decreases towards the precession minimum, and increases again after the precession minimum. The amplitude of the salinity variability is much smaller in the open Mediterranean box (Box 2), as it is connected to the Atlantic (Box 0), which has a constant salinity in this run. Deep water salinity (Box 3) lags the salinity of the upper boxes (this will be interpreted after describing the other graphs). As a result of this behaviour, the salinity of the marginal box (Box 1) briefly drops below the deep water salinity just prior to the precession minimum. The temperatures, shown in Fig. 3.3C, do not change drastically, except for a decrease in temperature at the margins in the interval surrounding the precession minimum (we will come back to this below). As temperature does not change much, density variability (Fig. 3.3D) is largely determined by changes in salinity. The dip in marginal temperature has an opposite effect on density compared to the salinity fluctuation, consequently the decrease in surface to deep density gradient is relatively small, and the marginal density does not drop below the deep water density.

Nevertheless, the decrease in the vertical density difference causes a decrease in DWF (D_1 Fig. 3.3E, also see equation 3.2). DWF in the open Mediterranean box (D_2) does not occur in this run, since the density in the upper open Mediterranean box never exceeds the density of the deep water box. The cause of the previously mentioned dip in marginal temperature, lies in the reduction of DWF which in turn decreases the inflow of water from the open Mediterranean to the margins (equation 3.12). The decrease in supply of relatively warm water to the margins causes the water temperature of the margins to approach the much lower atmospheric temperature. The outflow to the Atlantic (Qo, in Fig. 3.3D) depends on the density difference between the open Mediterranean and the Atlantic. Since the properties of the Atlantic water are kept constant in all presented model runs, the outflow only depends on the density of the open Mediterranean box. As expected then, the decrease in density of the open Mediterranean water in the interval surrounding the precession minimum causes a slight decrease in outflow to the Atlantic. The deep water oxygen concentration (Fig. 3.3D) depends on (i) oxygen consumption, and (ii) DWF and vertical mixing. The deep water oxygen concentration largely follows the same trend as DWF. From roughly 9-20 kyrs the deep water oxygen has a phase lead relative to DWF. Note that DWF does not have to stop completely to cause a decrease in the oxygen concentration; when the oxygen consumption combined with the out-flowing oxygen exceeds the supply of new oxygen, the deep water oxygen concentration decreases.

As we have seen in the description of Fig. 3.3D, the salinity decrease occurs in both the margins (where the deep water forms in this run) and the open Mediterranean (where the water that flows to the margins originates from). The deep water salinity depends on DWF and mixing with the overlying boxes. Consequently, the deep water salinity always lags the salinity of the upper boxes. The amount of lag between the deep and the surface boxes depends on the water and property exchange with the deep box and is therefore not constant throughout the run. At the precession minimum, the

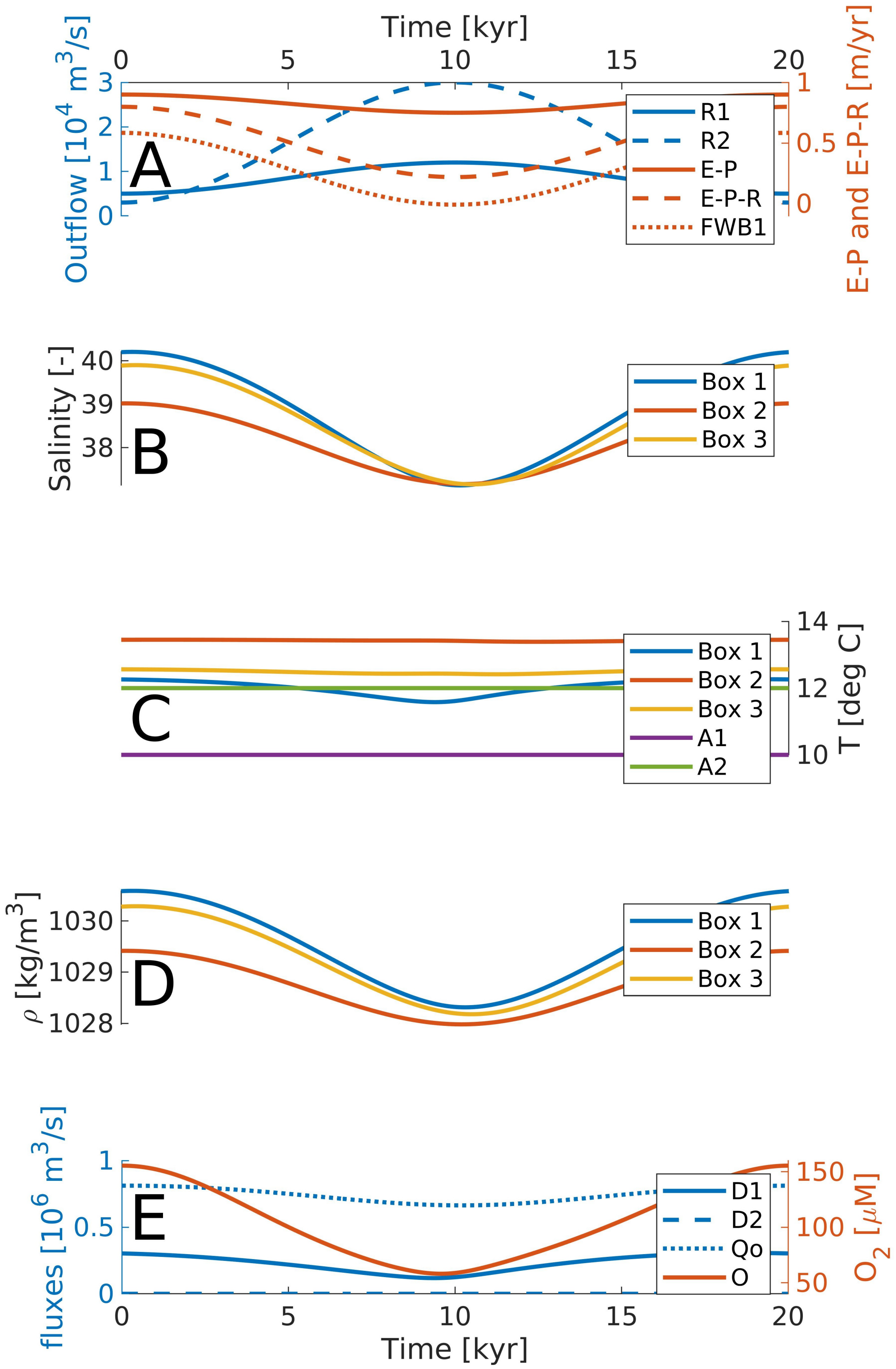

Figure 3.3 The forcing and results of the reference run. (A) The model forcing, with the river outflow on the left axis and the E-P, E-P-R and fresh water budget of box 1 on the right axis. (B)-(D) For each box respectively the salinity, temperatures, and densities. (E) The relevant fluxes (left axis) and the deep water oxygen concentration (right axis)

lag is in the order 200 years. As the increase in river outflow towards the precession minimum reduces DWF and mixing, the lag between deep and surface/intermediate water salinity also increases (too subtle to see in the graphs). As a result, there is a brief period, starting 1800 years before the precession minimum and ending 440 years after the precession minimum for the margins and 580 years for the open Mediterranean, where deep water salinity is higher than surface/intermediate water salinity. Because the changes in density largely depend on salinity in this run, and the dip in marginal temperature also slightly leads the precession minimum, it follows that the midpoint of this time interval of minimal DWF falls prior to the precession minimum. The DWF does not stop completely in this run (see Fig. 3.3E), because the relatively warm open Mediterranean surface/intermediate water keeps the deep water warmer (through mixing) than the marginal water, see 3.3. This reference run highlights why the sapropel state is inherently transient: the DWF is only slowed down when the density of the upper boxes is decreasing, and increases again when the density starts to return to precession maximum conditions. Since density cannot decrease indefinitely, a state with minimum circulation cannot be maintained.

The deep water flux at the precession maximum ($3 \cdot 10^5 m^3/s$) is somewhat lower than found in observational data ($1.6 \cdot 10^6\ m^3/s$, Pinardi et al., 2015), although comparable to the DWF of one of the Eastern sub-basins (Pinardi et al., 2015). Deep water oxygen at the precession maximum matches with observational data (155 μM in the model versus between 151 to 205 μM observed in the Western Mediterranean Sea and 160 to 219 μM Eastern Mediterranean Sea, Powley et al., 2016). Other conditions, such as temperature and salinity match closely to present day winter conditions (as reported in Hayes et al., 2019). DWF only occurs at the margins (box 1) in this run, the other deep water flux is only plotted for easy comparison to other runs (in which it does occur). None of the fluxes change direction in this run, resulting in relatively simple, although not entirely linear, behaviour: the phase relation between the salinities of the boxes is not constant and the temperature of the marginal box, as well as the deep water oxygen curve are clearly not sinusoidal. We consider the period with minimal deep water oxygen concentration, $60\mu M$, to be the model equivalent of sapropel conditions. Although we only find a very short sapropel (from $8.8 - 10.3kyr$) this run demonstrates that the model (i) is capable of approximating the present-day water properties and circulation when forced by present atmospheric conditions, and (ii) captures the reduction in DWF expected upon a change to wetter conditions.

3.3.2 Addition of atmospheric temperature variability

As described in the introduction, temperature variation due to precession likely also affected buoyancy loss. In order to examine this aspect, we run the model with a 3 $°C$ temperature increase at the precession minimum relative to the precession maximum. For atmospheric box A_1 the temperature increases from 12 to 15 $°C$, and for box A_1 the temperature increases from 10 to 13 $°C$. Both air temperature curves are described by sine waves, as shown in Fig. 3.4C. We decide to maintain a constant temperature difference between the two atmospheric boxes as there is insufficient evidence for other options. All other parameters are set as described in the reference run.

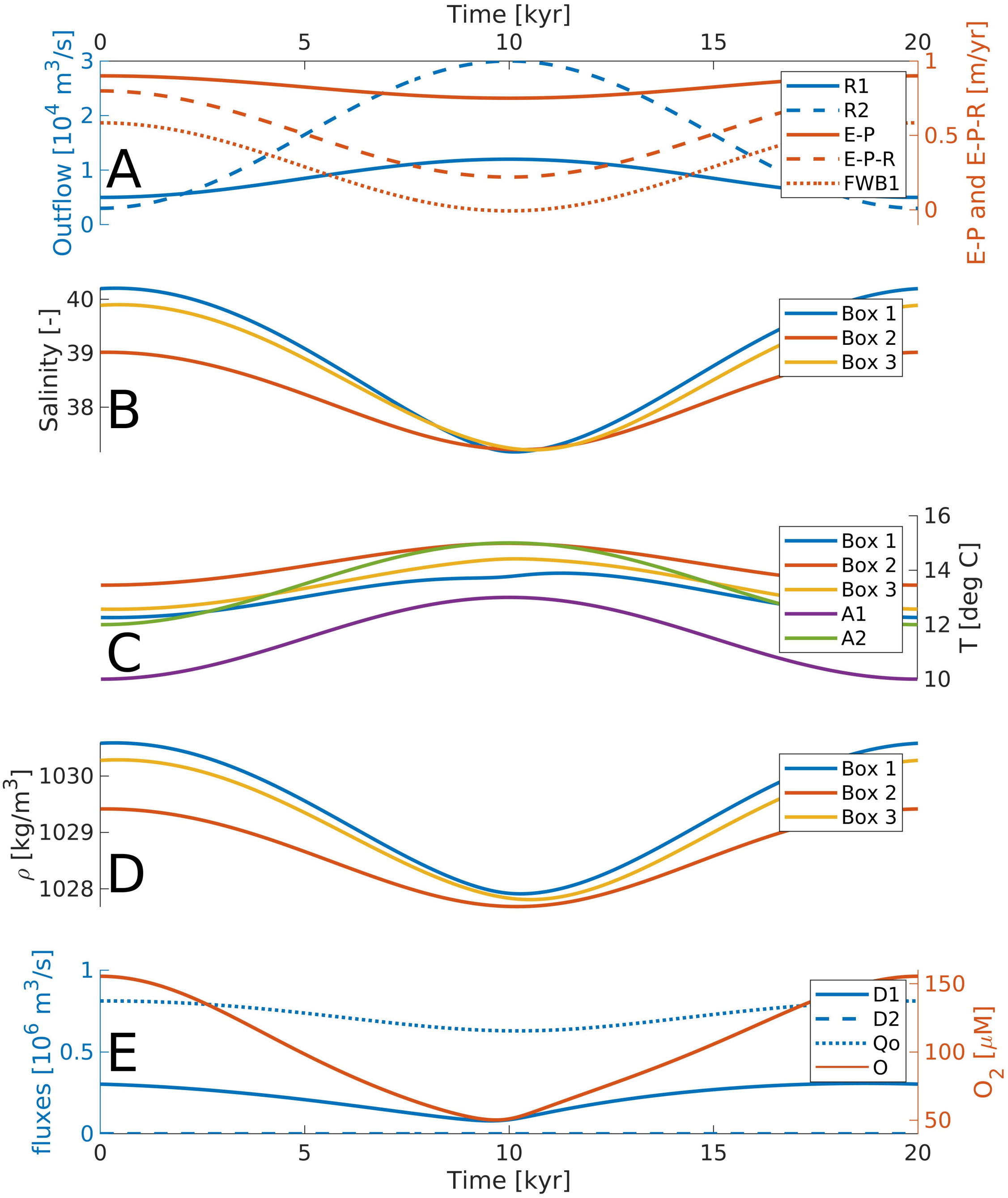

Figure 3.4 The forcing and results of the temperature-variability run. Layout of the panels is the same as in Fig. 3.3.

The overall behaviour of the model is similar to that in the reference run, except that the temperatures of all boxes are now higher during the interval surrounding the precession minimum (Fig. 3.4C). We still observe a minor decrease in marginal water temperatures at the precession minimum (cf. Fig. 3.3C), albeit much smaller than in the reference run, since it is now imposed on top of the trend caused by the changing atmospheric temperature. The net effect of a homogeneous basin wide temperature increase during the precession minimum is a further decrease in DWF during this time interval. We find a sapropel from t=8084 years to 10970 years, which therefore lasts 2013 years and the midpoint leads the precession minimum by 473 years (see Fig. 3.4E).

When testing the parameter space, we find that changes in marginal and open Mediterranean air temperature have an opposite effect on DWF: when the air over the margins becomes warmer, heat exchange with the marginal water directly increases the buoyancy of the water involved in DWF, slowing the circulation down. An increase in open Mediterranean air temperature, in contrast, primarily affects the open Mediterranean surface/intermediate water, which mixes with the deep water over a large area. The resulting rise in temperature of the deep water lowers its density, and thereby increases the marginal to deep water density gradient. Since this gradient controls DWF formation at the margin, an increase in open Mediterranean air temperature ultimately causes an increase in DWF. Since part of the open Mediterranean surface/intermediate water flows to, and mixes with, the marginal water, the effect of the open Mediterranean air temperature increase on the margin-deep water density gradient is relatively small. This run shows that an atmospheric temperature increase during the precession minimum significantly affects the duration of sapropel conditions in the model. Since both observational and modelling studies find this temperature variability (Marzocchi et al., 2015; Herbert et al., 2015), it will be included in all following model runs.

3.3.3 Nonlinear behaviour

Next, we explore the effect of a transition to and from a time interval with a positive freshwater budget. Whether or not the freshwater budget of the Mediterranean Sea becomes positive during sapropel formation has been widely debated (Rohling, 1994, and references therein). Although our model cannot directly prove whether or not this has happened, it does allow us to study what the implications for the water properties and circulation would be, which should help in recognising the expression of a budget switch in the geological record. First we consider a scenario where only the freshwater budget of the margins becomes positive, in a subsequent run we force the model in such a way that the freshwater budget of the entire basin changes sign.

To have the freshwater budget of the margins become positive, the maximum of R_1 is increased from $1.2 \cdot 10^3\ m^3/s$ to $1.4 \cdot 10^4\ m^3/s$ (Fig. 3.5A), all other parameters are kept the same as in the temperature variability run (Fig. 3.4), as shown in table 3.2 in the row of "fwb1 run".

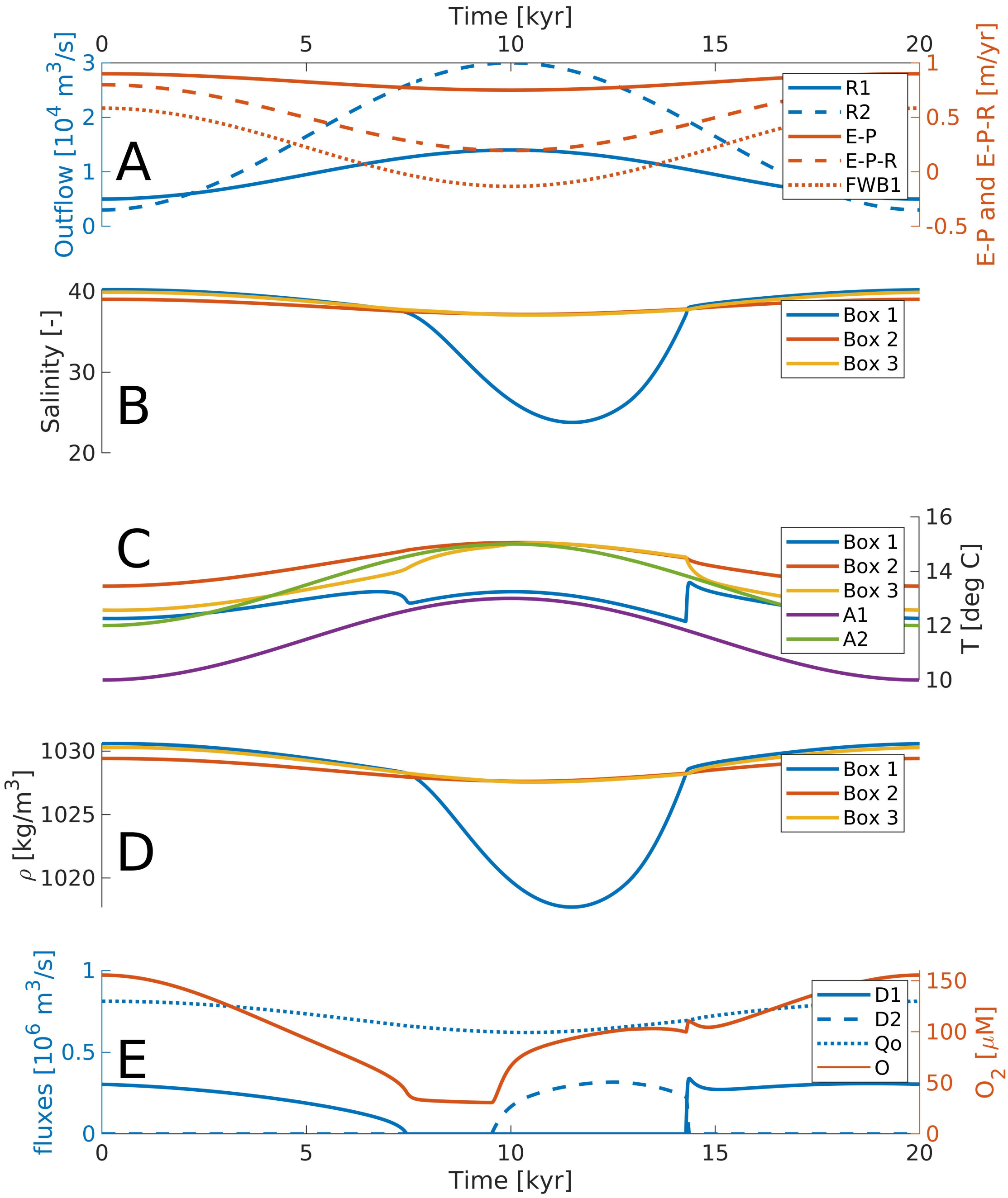

Figure 3.5 The forcing and results of the run where the freshwater budget of the margins becomes positive for a brief period. Layout of the panels is the same as in Fig. 3.3.

At a similar timing as the dip in temperature observed in the reference run, we now see a very large decrease in salinity at the margins from 9 to 13 kyr (see Fig. 3.5B). During this interval we observe that temperatures at the margins approach the temperature of the overlying atmospheric box, while deep water temperatures approach those found in the open Mediterranean (see Fig. 3.5C). All are an expression of the disappearance of DWF at the margin (see Fig. 3.5E; elaborated below) which effectively stops the exchange of the margins with the rest of the basin. Conditions at the margins are mainly determined by the river input (causing low salinity) and atmospheric temperature. The properties of the deep water are now only determined by mixing with the open Mediterranean surface/intermediate box, and DWF in the same box, explaining the similar temperatures. When the salinity at the margins reaches present day values again at 13 kyr, we observe a sudden subtle increase in deep water salinity, due to the abrupt increase in DWF at the margin at this moment (see Fig. 3.5D). Because the change in salinity is much larger than the change in temperature, the densities of each of the boxes (Fig. 3.5D) behave similarly to the observed salinities seen in Fig. 3.5B.

DWF at the margins is found to gradually decrease towards the precession minimum, then completely stop at around 8 kyr, and abruptly increase to normal circulation again at around 13 kyr. DWF in the open Mediterranean starts close to the precession minimum and ends abruptly when DWF at the margins starts again. Deep water oxygen largely correlates with the total DWF, although it reaches a minimum before DWF stops completely and begins to increase only shortly after DWF in the open Mediterranean starts. Similar to previous runs, outflow to the Atlantic (Fig. 3.5E) is slightly lower during the precession minimum, because (i) the density difference between the Atlantic and open Mediterranean surface/intermediate box is smaller, and (ii) the freshwater budget is closer to zero. We thus find that when the freshwater budget in the marginal box temporarily becomes positive, DWF occurs in the open Mediterranean at the end of the low deep water oxygen interval (conditions associated with sapropel deposition), thereby terminating this interval early (as shown in Fig. 3.5). Deep water mixing with the much less dense water at the margins decreases the density of the deep water, thereby causing DWF in the open Mediterranean box. The result of this is a phase lead of the sapropel midpoint (as a result of the earlier termination), instead of a phase lag commonly reported in literature (Grant et al., 2016).

In the next run we force the model in such a way that the freshwater budget of the entire basin becomes positive during the interval straddling the precession minimum. The maximum of R_2 is set to $8 \cdot 10^4$ m^3/s and the minimum evaporation to 0.74 m/yr (Fig. 3.6A), all other parameters are kept the same as in the temperature variability run. In the interval from approximately 9 to 13 kyr, the freshwater budget of the entire basin reverses. The changed forcing parameters are shown in table 3.2 in the row of "fwbtot run".

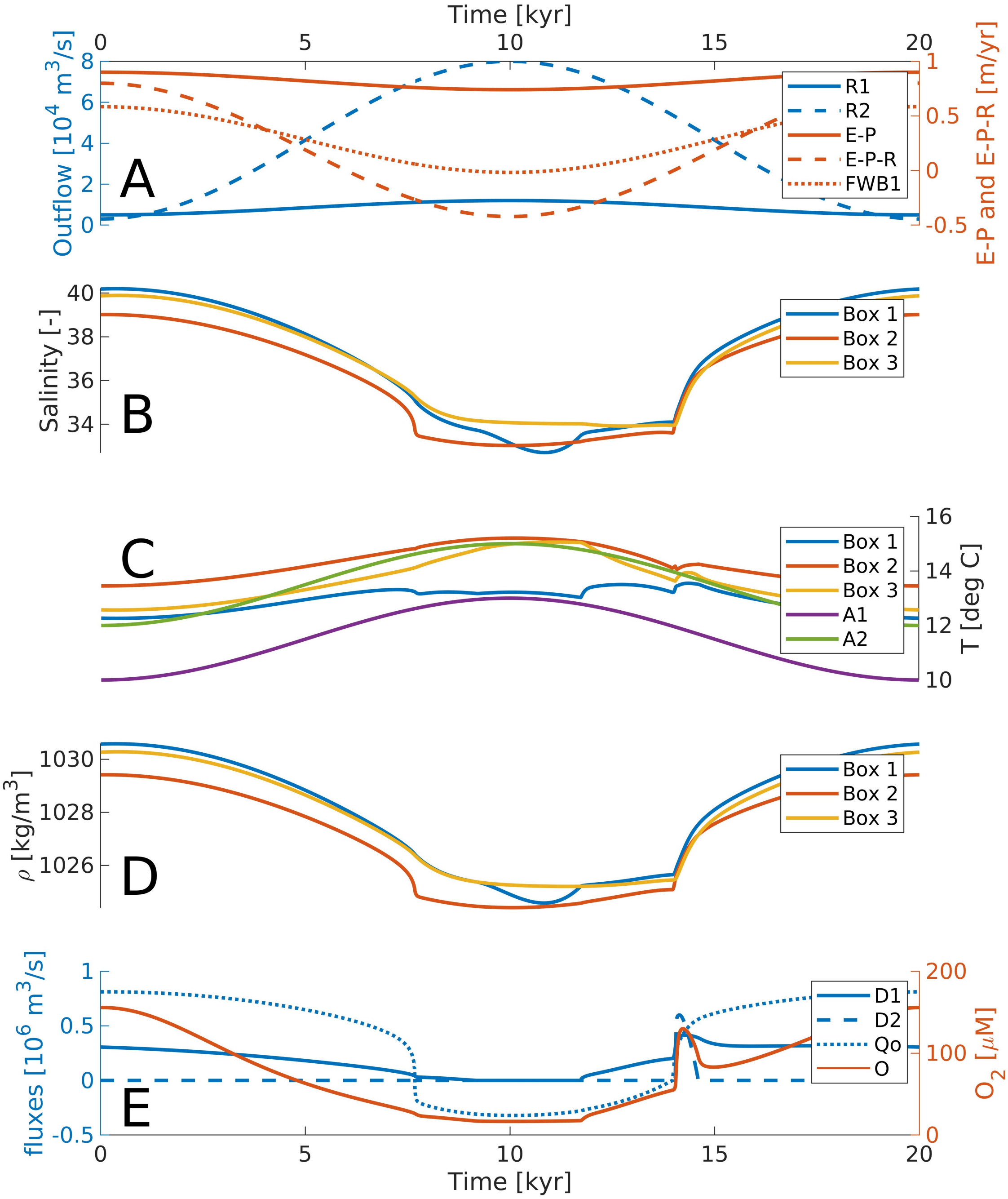

Figure 3.6 The forcing and results of the run where the freshwater budget of the whole basin becomes positive for a brief period. Layout of the panels is the same as in Fig. 3.3.

Salinities (Fig. 3.6B) decrease in response to the decrease in net evaporation. When the freshwater budget reverses, the exchange with the Atlantic decreases, causing less relatively saline water to flow into the upper boxes. Consequently, the salinity of the upper boxes further decreases. The deep water salinity only begins to decrease more when DWF at the margin starts again. When the freshwater budget becomes negative again, the salinities abruptly increase and then follow the freshwater budget more or less linearly. The main features of the temperature curves (Fig. 3.6C) are caused by the same events that are described above for the salinity variability, although temperature is also affected by heat loss to the atmosphere. Consequently, the same main features can be identified, with the difference that 1) the temperature of the upper boxes follows the air temperature curves, and 2) the amplitude is smaller, because the heat exchange with the atmosphere acts as negative feedback. The changes in densities are predominantly determined by salinity, as the changes in temperature are relatively small in this run.

Reversing the freshwater budget also causes the density difference between the Atlantic and open Mediterranean surface/intermediate box to change sign. Consequently, the density driven flow goes from the Atlantic to the Mediterranean, instead of the other way around. In Fig. 3.6E this is represented by the flux becoming negative. Note that this shift occurs almost instantaneously. In this run we find a very sharp termination of the sapropel, followed by a brief period with lower oxygen concentration (as shown in Fig. 3.6). This is caused by a peak in DWF in both the margin and open Mediterranean when the freshwater budget changes sign. Just prior to the reversal of the freshwater budget, the density of the open Mediterranean surface/intermediate water is much lower than that of the Atlantic water. The reversal of the freshwater budget then causes a rapid increase in surface/intermediate water throughout the basin, resulting in the peak in DWF. The irregularities observed in all runs (such as the occurrence of multiple local minima) where the freshwater budget of (part of) the basin reverses all strongly depend on the model set-up.

3.3.4 Phase of evaporation

Recent modelling studies (Marzocchi, 2016) have shown that while evaporation and river outflow are both forced by precession, they may have a different phase relation to their forcing. Runoff and evaporation are the only transient forcings in the presented model runs, therefore shifting runoff for example 2 kyrs forward in time gives the exact same wave shape as shifting evaporation 2 kyrs backwards in time. The only difference would be that the waveform would be shifted by 4 kyrs. Since we are primarily interested in the transient response rather than the absolute timing, we only investigate the effect of the phase of evaporation. To assess the effect of the phase of evaporation on sapropel formation, we calculate the sapropel midpoint and duration for a set of runs, with varying evaporation phase (all other parameters remaining unaltered between runs). Apart from the phase of the evaporation forcing, the model is forced exactly the same as in the atmospheric temperature variability experiment (as described in subsection 3.3.2).

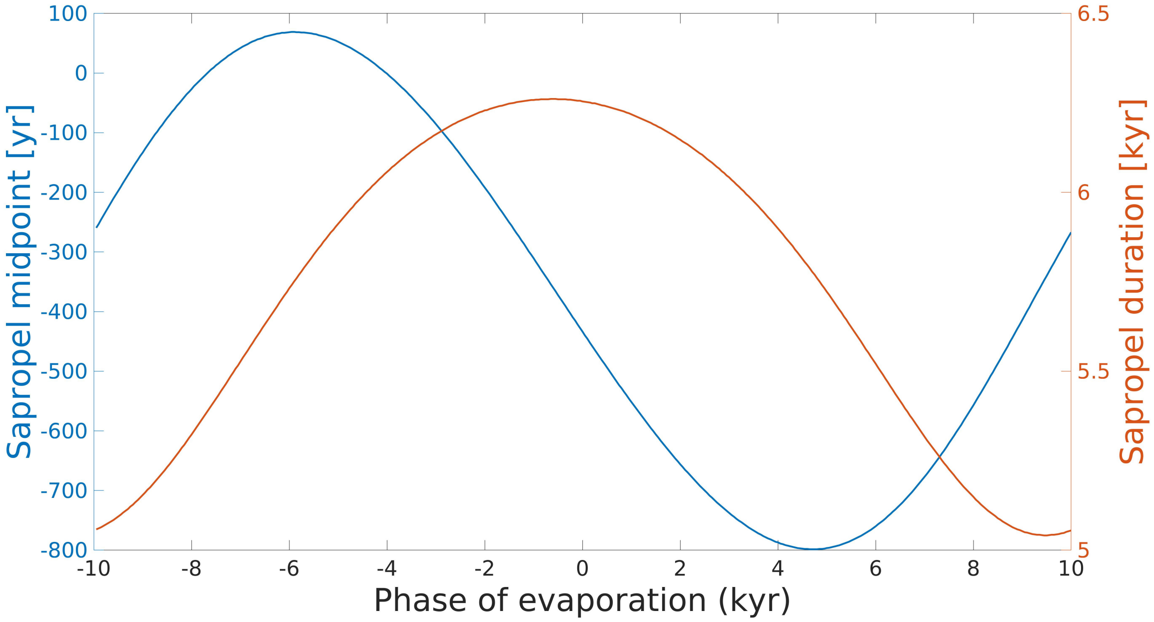

Figure 3.7 Sapropel duration (right axis) and timing of the midpoint relative to the precession minimum (on the left axis) as a function of the phase of evaporation. Apart from the phase of evaporation, the model forcing is the same as the run in subsection 3.3.2

As shown in Fig. 3.7, we find a maximum in sapropel duration when evaporation is almost in phase with precession. This is to be expected, as minimum evaporation then coincides with maximum river outflow. Similarly, a minimum in sapropel duration is found when evaporation is almost exactly in anti-phase with precession. In between these peaks the sapropel duration as a function of the phase of evaporation is described by a cosine. The sapropel midpoint is found to vary significantly (up to thousands of years with a large amplitude of evaporation variability) when varying the phase of the evaporation forcing. The shift in sapropel midpoint relative to the precession minimum is at a maximum when evaporation lags or leads approximately 5 kyr. This makes sense, as the minimum in midpoint shift occurs when evaporation is either in phase with precession, or in anti-phase (i.e. a shift of 0 or 10 kyr), the 5 kyr lead/lag falls right in between these points. The timing of the midpoint as a function of the phase of evaporation in between these extremes is described by a nearly perfect sine wave. Note that the peaks are not exactly at -5 and and 5 kyr, but slightly shifted, this is likely a result of the equilibrium time of the system.

This experiment, combined with the systematic testing of the parameter space, highlights that although the exact timing and duration depend on the exact forcing, the minimum in deep water oxygen concentration always occurs close to the precession minimum and the model response is always quasi-linear, as long as fresh water budgets are not reversed. We also find that the magnitude of the effect of the phase of evaporation on sapropel timing and duration depends on the amplitude of the evaporation variability (not shown). This makes sense, as the changes in circulation largely respond to freshwater budgets (the only difference between river inflow and evaporation being their respective temperatures) and the amplitude of evaporation variability scales linearly with its impact on the variability of the freshwater budgets.

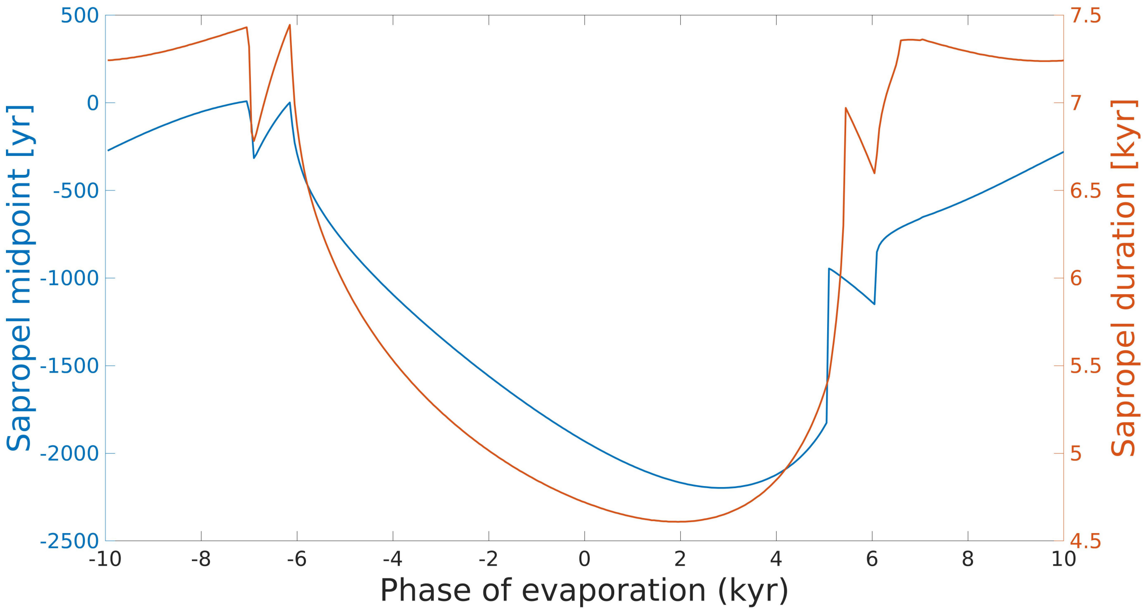

Figure 3.8 Sapropel duration (right axis) and timing of the midpoint relative to the precession minimum (on the left axis) as a function of the phase of evaporation. Apart from the phase of evaporation, the model forcing is the same as the first run in subsection 3.3.3

When systematically varying the components of the water budget within the limits mentioned in model setup, we find that in the regimes where the freshwater budget of (part of) the basin changes sign, sapropels are cut short considerably. When performing the same analyses described above, but now using the forcing of the first run in subsection 3.3.3, we find that this causes the midpoint of the sapropel to occur prior to the precession minimum (Fig. 3.8). Note that runs with multiple sapropel intervals cannot be described as having a single midpoint or duration.

3.4 Discussion

3.4.1 Model convergence

The time step of one year naturally results from the concept that deep water forms during winter storms, making it the highest resolution possible as long as seasonal variability is not included. From a purely mathematical perspective, however, the time resolution should not affect the outcome significantly, as long as a sufficiently small time step is used to prevent aliasing. We tested this by varying the temporal resolution given a certain forcing. We find no significantly different results with a time step below 10 years. With a time step larger than 10 years aliasing occurs. We conclude that a time step of 1 year is sufficient for the analyses in this study.

3.4.2 The role of assumptions and simplifications

All models require assumptions and simplifications to be made, as they are by design a simplified version of (part of) a system. Simple box models, such as the model presented in this paper, aim to identify the smallest subset of processes that can describe a certain phenomenon. As such, this model represents a generic semi-enclosed basin, given that no specific geometry is included. This implies that by altering the parameter values and in some cases the strait exchange equations, the model can easily be adapted to other semi-enclosed basins, such as the Black Sea.

In our model we parametrize intra-annual variability. Including seasonality would require separate intermediate water boxes (increasing complexity), while for the oxygenation of deep water only the amount of DWF and mixing with the overlying water mass is truly relevant. Furthermore, we would have to make assumptions regarding the annual variability of the forcing parameters (river outflow and evaporation), which are not well constrained for geological history. We therefore decided to parameterize the seasonal variability, by calculating a yearly averaged DWF flux based on winter temperatures. This allows us to study the fundamental mechanisms of sapropel formation. OGCMs would be more appropriate to study the role of seasonal variation.

We do not include separate boxes for the Eastern and Western Mediterranean in our model. The aim of a conceptual model is to capture the first order aspects of a process with a minimal setup. The current setup does this. Incorporating separate sub-basins would imply doubling the number of boxes and would also double the number of forcing parameters and equations, all of which add uncertainty to the model (quantitative reconstructions do not exist for most of these parameters). Moreover, the complexity quickly increases, making it much harder to test and describe the parameter space and identify key mechanisms. While this could be tested in a future study, we find it important to first understand the behaviour of the a semi-enclosed basin with a gateway before studying what is essentially a second order system. We expect that the effect in the Eastern basin is similar to the difference between a first order and second order filter: a larger shift of the midpoint (larger group delay), and likely a higher sensitivity in the Eastern basin. Any resonances in the system are also expected to become more prominent (since the resonant frequencies are now amplified twice).

The model forcing used in this study is chosen to reflect either the variability envisaged in the commonly accepted mechanism (as sketched in subsection 3.1.1), or oceanographic and climatic variability deduced from modelling studies and the geological record as accurately as possible. Other processes such as the North Atlantic oscillation and solar activity are not taken into account, because they are not thought to be of first order importance for sapropel formation, as described in Rossignol-Strick (1985) and Rohling et al. (2015), for example. While these processes likely influence sapropel formation, they are unlikely to be essential. Besides precession, obliquity also affects sapropel formation, but it is not our aim to reconstruct the exact conditions during specific time intervals. For an individual sapropel, adding an obliquity component would effectively slightly modulate the frequency and amplitude of the forcing. Since the model is not very sensitive to the exact frequency of the forcing, and we already extensively tested the parameter space in terms of amplitude, a simple (20 kyr) sine wave suffices as forcing. Also note that since obliquity does not have a harmonic relation with precession, the modulation would not have the same effect on every sapropel. It likely affects the thickness of a sapropel for example, but the effect may work both ways when comparing different sapropels.

The model output comprises an average value for deep water oxygen, as the deep water is a single box. In reality, however, oxygen concentrations vary spatially. A prime example of this is the absence of sapropels in most of the Western Mediterranean Sea. This abstraction should be taken into consideration when interpreting the model results. This model focusses on the transient response of water fluxes in the Mediterranean Sea, the oxygen output is calculated to get a first order impression of deep water ventilation. A biogeochemical model, similar to the one presented in Slomp and Van Cappellen (2007), would have to be included to specifically study bottom water oxygenation. We expect that the main difference with a biogeochemical model is that in our model river input directly affects oxygen consumption, while the surface/intermediate boxes would act as a reservoir for nutrients (with their own feedbacks) in the biogeochemical model, thereby delaying the response to changes in river input. Note finally that in reality DWF occurs following two different mechanisms (open ocean convection and mixing of the water at margins during winter storms, which then cascades to the deep basin, see subsection 3.1.1), as well as in multiple sub-basins that each have their own conditions. The regime in Fig. 3.5 relies on the freshwater budget of the margins changing sign. In reality there are many different marginal water masses in the sub-basins, rather than one single ”margin”. This makes it likely that the freshwater budget becoming positive in any one of these sub-basins will have similar consequences for the circulation. Since the freshwater budgets of these basins are independent, it would be possible to drastically alter the circulation multiple times during a single precession cycle. Presently, the Adriatic sea has a positive freshwater budget (Raicich, 1996), and the Aegean sea is known to have had a positive fresh water budget in the past (Zervakis et al., 2004).

The simplicity of the model makes it especially suitable for describing transient, nonlinear behaviour, allowing for the identification of crucial mechanisms. More complex models, while providing other benefits, are generally too difficult to interpret on this level, or do not allow for runs of sufficient length to study the transient response over a full precession cycle. The presented model runs give an overview of the behaviour of the model. When systematically testing the parameter space, we find that this behaviour largely depends on general trends and reversal of fresh water budgets, rather than specific forcing or parameter choices. This makes the results of the study much more robust and meaningful.

Exchange with the Black Sea also affects circulation in the Mediterranean Sea (Soulet et al., 2013, show increased runoff during HS1). For sapropels during which there is exchange through the Bosphorus strait, the exchange is not constant through time, and also depends on the inflow of Mediterranean water into the Black Sea. Opening or closing of the strait prior to, or during, a sapropel may impact the circulation. When the sill becomes deep enough to allow for a two layer exchange, a large amount of saline water would flow into the Black Sea (following the same principle as at the Gibraltar Strait), thereby causing extra, relatively fresh, water to flow out into the Mediterranean Sea. During some sapropels, the strait may have been closed. Furthermore, there is very little data regarding the exchange opening and closing of the Bosphorus Strait prior to the most recent opening (approximately 11 ka), perhaps with the exception of the Pontian (which is beyond the scope of this paper). Consequently, we do not include exchange with the Black Sea. For the cases where there was a steady outflow of fresh water (or an exchange that can be parametrized as such) this could indeed be seen as an extra fresh water source for the margins. We have already tested this effect by varying the river outflow into the margins.

Melt water pulses likely affect sapropel formation, but we do not consider them to be of first order importance. During many sapropels, melt water pulses did not occur. In future applications of this model where a specific sapropel/interval is studied, drivers such as melt water pulses should be included.

3.4.3 Describing nonlinear relationships and transient response

The occurrence of sapropels is often considered from a binary perspective: a sediment is either a sapropel, or it is not. The dominant forcing mechanism (astronomic variability), however, can be easily described by a combination of a limited number of sine-waves: the resonant frequencies of the planetary bodies in our solar system (for example Laskar, 1988). For a single sapropel, only climatic precession—a nearly a perfect sine—is considered to be of first order importance in controlling bottom water oxygenation (Rossignol-Strick, 1985), with the rest of the orbital configuration mostly modulating the effect of precession. If a model strives to capture the current hypothesis of sapropel formation, starting from astronomic variability, it must therefore transform a sine wave into something that is not a sine wave, requiring the model to be nonlinear. Our model allows for such behaviour. Even when considering intra-sapropel variability, thereby surpassing a binary approach, the sapropel record is clearly not sinusoidal (see for example Grant et al., 2016; Dirksen et al., 2019).

One of the main research questions of this study is when sapropel formation occurs. In a linear system, one would simply calculate the phase of the output with respect to the input. However, as the output is no longer linearly related to the input, this is not possible. A simple threshold analysis is not ideal either, as the cut-off level can have major impact on both timing and duration, while a clear definition is not readily available. Furthermore, even when the threshold is defined, this method would not be usable for sapropelic marls, which are thought to be the result of the same process, but do not share the same chemical composition. We partly avoid this problem by not only considering the midpoint of the sapropel (when assuming a certain oxygen threshold, see subsection 4.5), but also the full wave form (e.g. which intervals could be sapropelic with a slightly different forcing). In the sedimentary record this is generally not possible, since the non-sapropelic intervals do not record all parameters and are often bioturbated. So while our approach cannot be applied to the sedimentary record, it does give insight into the factors that influence sapropel timing. Even this definition of sapropel timing becomes problematic when one or more interruptions occur, since in that case there is more than one midpoint.

We find that, when using realistic model forcing, stable sapropel conditions do not occur. Even when using constant forcing, a permanent complete stop of DWF either does not occur, or only under very specific conditions. Note that in the Black Sea permanent stratification does appear to occur, but here, the positive freshwater budget allows some of the water flowing into the Black Sea at the Bosphorus Strait to sink to the deep water (Bogdanova, 1963), keeping it relatively saline and dense. However, our results indicate that sapropel conditions can occur transiently without a positive freshwater budget, with realistic forcing. We therefore conclude that studying the oceanographic state during sapropel conditions by modelling steady-state conditions with a stratified water column results in a very limited understanding of sapropel formation.

3.4.4 Comparison with geological data and other models

Comparing model results to geological data is most effective when an accurate age model is available for the geological data.We will therefore only consider the 5 youngest sapropels in this paper. The most recent sapropel (S1) is thought to have been triggered by sea level rise, which in turn resulted in a connection between the Black Sea and the Mediterranean Sea (Rohling et al., 2015). As both sea level variability and exchange through the Bosphorus Strait are beyond the scope of this paper, sapropel S1 is not suitable for comparison. We therefore focus on sapropels S3, S4, and S5 in the rest of the section.

In the run with variable air temperature (Fig. 3.4), the modelled sapropel duration and timing is within dating uncertainty with what has been found for sapropel S3 and S4 in core LC21 (Grant et al., 2016). Note that the same study finds that sapropels S1 and S5 lag precession by 2.1-3.3 kyr. This suggests that our model is capable of capturing the most relevant mechanisms for S3 and S4, but that other features not included in the model affected the timing of S1 and S5. For S5 there is evidence suggesting that the Black Sea reconnected to the Mediterranean Sea within the dating uncertainty of the onset of sapropel S5 (Grant et al., 2016, 2012; Wegwerth et al., 2014)

It should be noted that while the model often shows a midpoint lag (relative to the insolation minimum) of a few hundred years, uncertainties related to radiometric dating methods are often larger. However, we find that midpoint lag becomes larger with decreasing strait efficiency, implying that during times with low sea level or otherwise restricted exchange, the lag might become very relevant. A prime example of such a case would be the Messinian Salinity crisis and the surrounding intervals (Topper and Meijer, 2015). Moreover, as shown in Figures 3.5 and 3.6, alternative regimes (where the freshwater budget of either part of the basin, or the entire basin changes sign) can shift the midpoint of the sapropel considerably, as shown in Fig. 3.8. Unlike the relatively minor shifts in midpoint resulting from only changing the phase of evaporation, the resulting difference in sapropel timing is sufficiently large to be detectable in the geological record.

Lange et al. (2008) find that the freshening of the surface waters starts earlier and lasts longer than the suboxic bottom water conditions during S1. Our model also shows this behaviour in all of the presented runs (most notably in figures 3.3, 3.4 and 3.6). This makes sense as the DWF does not stop completely when the surface water starts to become less saline; it only reduces slowly. Furthermore, the oxygen has to be depleted for suboxic condition to occur, this is limited by oxygen consumption, and further slowed down by vertical mixing and DWF. How much longer the period of reduced sea surface salinity lasts compared to the period of suboxic bottom water likely depends on the exact location and water depth. The model is therefore mostly useful to gain insight into the mechanisms, rather than in the exact timing.

The regime described in Fig. 3.6 can show a sudden termination of the sapropel, which is similar to that seen in records of sapropel S5 (Dirksen et al., 2019). In the model such a sudden termination can only be achieved by forming deep water in the open Mediterranean, by reversing the freshwater budget of the entire Mediterranean. The coupling between the margins and deep water is insufficient to cause such a sudden termination. This suggests that during S5 the freshwater budget of part of the basin, or the whole basin potentially reversed. Such a large change in freshwater budget is in line with Bale et al. (2019), who found that surface salinities in three different cores in the eastern Mediterranean were sufficiently low to support free-living heterocystous cyanobacteria during sapropel S5. Moreover, oceanographic conditions may differ significantly between different parts of the basin: the oxygen concentration (and related variables) of a hypothetical core taken at the margin would be expected to show a pattern more similar to the DWF in the marginal box, while a core in the open Mediterranean may be more similar to the open Mediterranean surface/intermediate water box.

Sapropel interruptions commonly occur in the stratigraphic record (for example in S5 in core LC21, Rohling et al., 2006, 2015). With slightly different settings, the sharp peak in deep water oxygen in Fig. 3.6E can be made to occur earlier and less intense, resulting in an interrupted sapropel. The model therefore suggests that such interruptions can occur without further external forcing. This hypothesis could be tested in the stratigraphic record by looking for evidence of a reversed freshwater budget of (part of) the basin during such interrupted sapropels, and constructing high resolution intra-sapropel age models to assess the relative timing of the relevant features compared to insolation.

Each sapropel in the geological record is different, this already becomes apparent when considering the most recent 6: S1 has a different timing and is likely related to sea level variability (Grant et al., 2016; Hennekam, 2015; Grimm et al., 2015). S2 is not found at all. S4 has and interruptions in core LC21 (Grant et al., 2012), and the high resolution records of for example trace metals show very different characteristics. In the same core, the timing of the midpoint of S3 and S4 compared to insolation is the same, while that of S1 and S5 are different. S5 is much longer than all of the previous sapropels, does not have any burn down at at least one location (Dirksen

et al., 2019), has an interruption in other locations (Rohling et al., 2006) and again shows generally different characteristics in different cores (Dirksen et al., 2019; Grant et al., 2016; Rohling et al., 2006). S6 again looks very different.
We conclude that both in the geological record and in the model, a typical sapropel does not exist. The timing and mechanisms involved may differ considerably between sapropels and locations, as highlighted by our model results. Moreover, we find that an increase in freshwater budget alone is not sufficient to describe all key aspects of sapropel formation. An increase in atmospheric temperatures during the precession minimum (as observed in data and modelling studies, Marzocchi et al., 2015; Herbert et al., 2015) directly affects buoyancy loss during the interval in which sapropels form. This makes atmospheric temperature variability an integral feature of the system. Without it unrealistic evaporation or river outflow is needed to result in sufficiently long sapropels. Our model results support this hypothesis.

3.5 conclusions

The analysis presented in this paper illustrates that relatively simple models can give new, fundamental insights into the physical processes driving sapropel formation. The timing of sapropels relative to insolation has been widely studied in the sedimentary record. On the basis of our novel long-duration experiments we find that the timing of sapropels is very sensitive to the exact climatologic and oceanographic conditions. The nonlinear response to insolation forcing implies that the sapropel record does not have a linear phase relation with insolation. The strongly nonlinear regimes in our model highlight that the mid-point of a sapropel (the average of the ages of the top and bottom of the sapropel) can be shifted significantly with a minor change in forcing, by cutting it short with a sudden termination, while during the rest of the precession cycle the response can be very similar to the nearly linear regime presented in the reference experiment. Our model results suggest that an increase in freshwater input alone, as in the general hypothesis for sapropel formation, does not provide a sufficient reduction in buoyancy loss to form sapropels as they are found in the geological record. We propose that precession controlled atmospheric temperature variability also plays a key role in the process of sapropel formation.

3.6 Appendix A

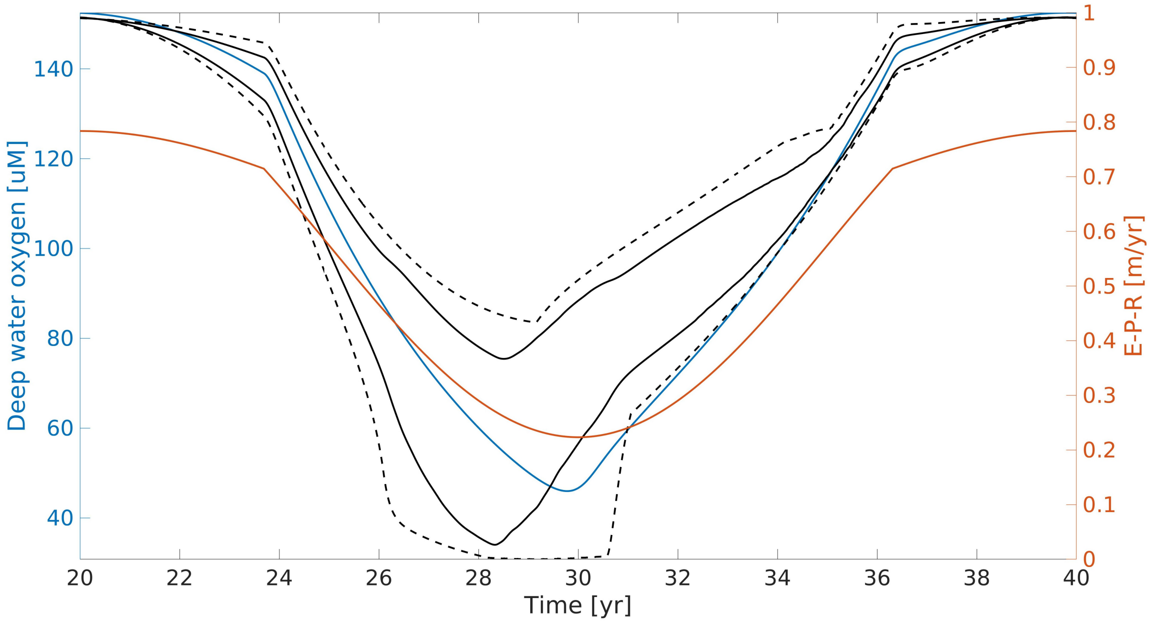

Figure 3.9 An example of the sensitivity analyses. Here the maximum of R_1 is varied randomly by up to $5 \cdot 10^3$ m^3/s above or below the general setting over 200 runs. The blue line indicate the initial run, the solid black lines indicate the upper and lower 1σ of each point in time, and the black dashed lines the minimum and maximum.

4 Transient-model analysis of the formation of organic rich deposits in the Holocene Black Sea

4.1 Abstract

In the early Holocene the Bosphorus strait was shallow due to low eustatic sea level after the last glacial maximum. The Black Sea was a brackish lake, with no inflow from the Sea of Marmara and only outflow of excess freshwater. Upon full opening of the Bosphorus, at 9 *ka*, bidirectional flow started and the bottom water in the Black Sea initially remained oxygenated. Subsequently, the oxygen concentration decreased until the basin reached a state with a stratified water column and anoxic bottom water. Organic rich sediments have been associated with this stratified period. When productivity decreased, organic carbon content decreased as well and the basin reached its current state. This chapter aims to clarify the physical, chemical and biological process that resulted in the evolution of the Black Sea from the early Holocene up to the present.

A novel transient box model is presented, combining a dynamic representation of water circulation with that of the limiting nutrient, phosphorus, to study the mechanisms of bottom water oxygenation and the formation of organic rich sediments in the Black Sea during the Holocene. We find that the model converges to a mixed state prior to the opening. When the strait is opened, deep convection oxygenates the bottom water and more nutrients are transported into the Black Sea through the Bosphorus. This sudden increase in nutrients at the surface causes an increase in productivity, which in turn causes an increase in oxygen consumption in the deep water. Subsequently, the model converges to a stratified state, with anoxic bottom water and relatively low productivity, i.e. the current situation in the Black Sea. These findings are in accordance with the sedimentary records, which indicate oxic bottom waters during the lake phase. The results highlight the interplay of hydro- and nutrient dynamics as controlling factors of the development of anoxia in the Holocene Black Sea.

The evolution of regional sea level is not well quantified. We therefore explore two options: 1) a monotonic sea-level rise and 2) the same sea-level curve with a harmonic oscillation superimposed. When forcing the model with a monotonic sea-

---

Picture left: Approaching Istanbul with the RV Pelagia at the end of cruise 64-PE406-E. The red boat is the pilot. The Bosphorus connects the Mediterranean to the Black sea. This chapter is in preparation for publication (Dirksen et al., to be published).

level rise, option 1, we find a single period of bottom water oxygenation, while the harmonic oscillations, option 2, cause several peaks in bottom water oxygenation. A sea-level induced reduction in the strait efficiency (i.e. the magnitude of density driven flow through the strait at a given density difference) is sufficient to cause multiple intervals with oxic bottom water. Hence, it is not required to fully block the inflow. We find that non-monotonic sea-level rise causes an earlier stratified phase, i.e. convection stops before the nutrients have reached an equilibrium. This results in higher nutrient concentrations at the surface at the start of the stratified phase, which in turn causes an increase in primary production and thereby greater export productivity and oxygen consumption in the deep water. A non-monotonic sea-level rise is therefore more likely to cause the formation of organic rich sediments. However, the results with a monotonic sea level increase have an overall best match with the geological record.

4.2 Introduction

The Black Sea, currently a saline water body with a relatively low salinity of 17, is connected to the Sea of Marmara through the Bosphorus Strait, which also provides a connection to the global ocean through the Mediterranean Sea (Fig. 4.1). With its surface area of $423,000\ km^2$ it is a significant water body (Kubryakov et al., 2012). Presently, the water column is highly stratified. Consequently, very little oxygen is supplied to the bottom water, causing anoxia and euxinia. Oceanographically, the Black Sea has changed significantly throughout its geological history. During the early Holocene it was an isolated, brackish lake, due to low eustatic sea level after the last glacial (Piper, 2016). Previous studies suggest that there was always an outflow from the Black Sea, through the Bosphorus to the Mediterranean Sea. In this sense, the Bosphorus was never fully closed. When we mention the "opening" of the Bosphorus, we refer to the first moment at which two-way transport is established, simultaneously allowing the inflow of the relative saline Mediterranean water *and* the outflow of the Black Sea surface water. Similarly, a "closed" Bosphorus refers to the situation where there is either only one-way strait transport, or no transport at all. The transition from a brackish lake to a stratified sea is a direct result of the opening of the Bosphorus strait, although the exact timing, dynamics and mechanisms are still unclear (Mertens et al., 2012).

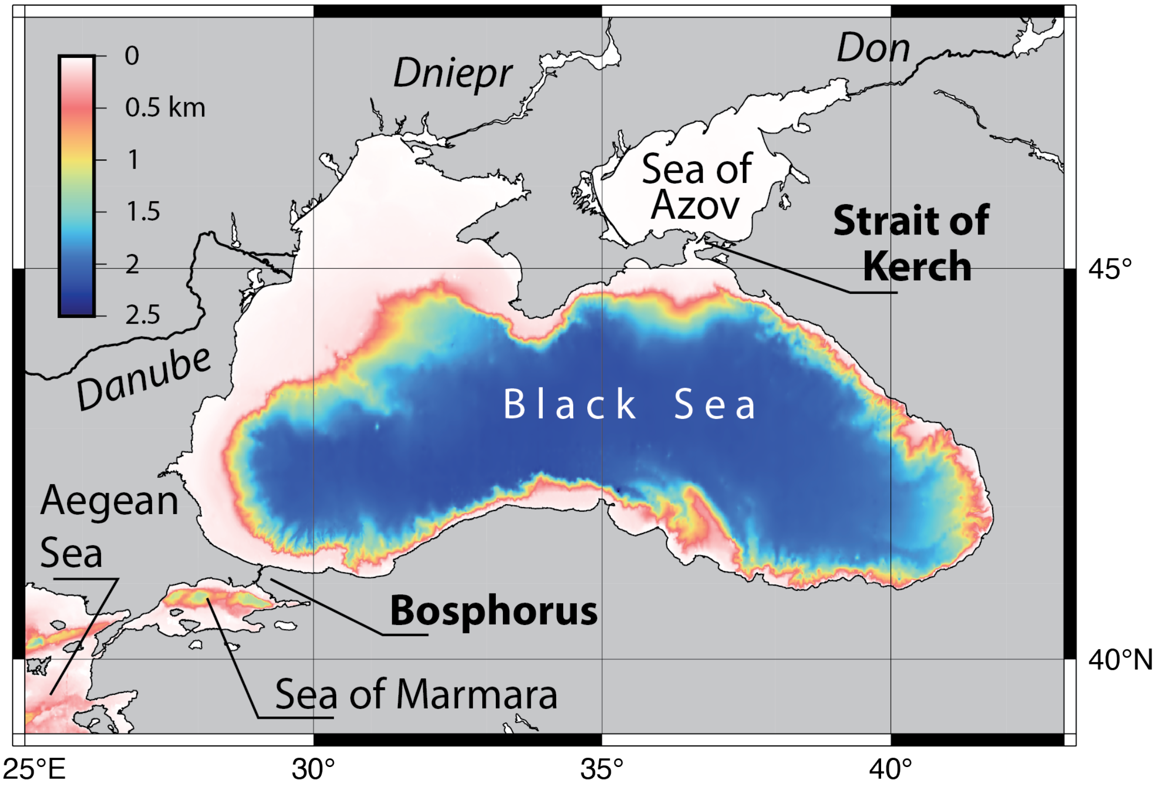

Figure 4.1 A bathymetric map showing the Black Sea, adjacent basins, straits and the main rivers.

The melting of the ice sheets caused the level of the Mediterranean Sea and the Sea of Marmara to rise in concert with global sea level. Around 9 ka this led to connection of the Sea of Marmara and the Black Sea. This resulted in a rapid saltwater inflow from the Sea of Marmara (Soulet et al., 2010; Egger et al., 2016), altering the salinity profile and stratification of the Black Sea (Ryan et al., 1997). According to Piper (2016) and Lane-Serff et al. (1997), the period with one-way strait transport ended when the sea level exceeded the critical height of 11 m above the sill. Some Holocene sea-level reconstructions show a monotonic rise (e.g. those shown in Boudreau et al., 2022), while other reconstructions show a more complex cyclic series of transgressions and regressions (Kislov, 2018). We explore the consequences of both options.

After the opening of the Bosphorus Strait there was a period of increased vertical mixing, enhancing primary production (PP). Prolonged inflow caused a stable stratification to develop, followed by anoxia and euxinia throughout the water column, due to a lack of ventilation and increased organic matter input by PP (Arthur and Dean, 1998). The onset of the anoxic and euxinic conditions occurred approximately 7.8 ka, when an organic rich layer was deposited (Arthur and Dean, 1998; Wilkin et al., 1997; Eckert et al., 2013) with a typical total organic carbon (TOC) of up to 15%, compared to $2-4\%$ prior to the opening (Eckert et al., 2013). Next, diminished primary productivity caused a decrease in the burial of organic carbon (Arthur and Dean, 1998). The formation of this organic rich deposit at the onset of stratification, shortly after the opening of the Bosphorus Strait (Eckert et al., 2013), suggests that these two events were related. Today and likely in the past, the anoxic and euxinic environment does not persist throughout the entire water column. The surface waters are in equilibrium with the atmosphere and are separated from the anoxic and euxinic water by a suboxic chemocline. The suboxic chemocline has been at a depth of approximately 150 m for the past 2.7 ka. The sediments formed after the organic rich layer still have a relatively high TOC of approximately 5% (Eckert et al., 2013).

The nutrient dynamics of the Black Sea are strongly affected by stratification and consequently by anoxia and euxinia. The strong stratification makes the phytoplankton in the photic zone more dependent on nutrients provided by riverine inflows and exchange with the Sea of Marmara (Friedrich et al., 2002; Slomp and Van Cappellen, 2007). The highest nutrient concentrations are found in coastal zones near shelves, close to the rivers (Fig. 4.1). The gyre in the western part of the basin causes these nutrient-rich waters to largely remain on the shelf (Friedrich et al., 2002). Hence, most PP occurs in these coastal zones (Friedrich et al., 2002). Coastal anoxia, caused by e.g. eutrophication, is exacerbated by global warming (Altieri and Gedan, 2015). Coastal anoxic zones are detrimental to local ecosystems, and their expansion and increase in intensity is a concern (Diaz and Rosenberg, 2008).

Rivers are the primary source of freshwater for the Black Sea. The Danube and Dniepr flow into the large north-western shelf (Fig. 4.1) and account for 72 % of the river discharge (Ludwig et al., 2009). Early Holocene glacial melt-water intrusions likely caused a large change in the freshwater budget. The run-off from ice sheets over the northern Anatolian mountains and the Fennoscandian ice sheet increased the freshwater input in the Black Sea (Wegwerth et al., 2016). However, quantitative reconstructions of the effect of glacial melt on the river outflow into the Black Sea, as well as quantitative reconstructions of net evaporation, are lacking.

4.2.1 Aim

This study presents a novel, transient, integrated hydrodynamic and nutrient box model for the Black Sea, describing the transport of water and nutrients in the basin. Key mechanisms that control the burial of organic matter and bottom water oxygenation are identified. Information about the presence and development of anoxia in the past is important to make predictions about anoxia in the future. The great advantage of a box model is that it gives a detailed description of transient behaviour on geological time scales, with a CPU-time of seconds on a stand-alone computer. The model allows us to study the transient behaviour of organic matter burial on millennial time scales and beyond, while still retaining a high temporal resolution of one year. A simplified sea-level curve is used, i.e. a monotonic increase, to highlight the response of the basin to an opening event of the Black Sea. In addition, the impact of a harmonic oscillation superimposed on the monotonically increasing sea level is presented.

4.2.2 Previous modelling studies

In contrast to the Mediterranean Sea, the water and nutrient cycling of the Black Sea has not been studied extensively with numerical models. Most of the modelling studies focus on the strait exchange and its influence on the Mediterranean Sea. Karaca et al. (1999) developed a two-box model of Black Sea water and salinity that includes a surface-water layer and a deep-water layer. They modelled the evolution of salinity over time, starting directly after the opening of the Bosphorus Strait. The simulated salinity reached a value close to steady state, present-day values, illustrating the robustness of even a simple model. However, this model imposes present-day water fluxes, making it unsuitable for studying the transient response of these fluxes. Lane-Serff et al. (1997) modelled the hydraulics of the Bosphorus Strait to study the opening of the connection between the Mediterranean and the Black Sea. They postulated a required critical sea-level, necessary for a bidirectional flow to occur through the Bosphorus Strait: 11 m above the sill. The effect of isostasy on the opening of the Bosphorus Strait was investigated by Lambeck et al. (2007). Isostasy potentially affects the Black Sea basin shape and depth, as well as the Bosphorus Strait itself, and could hence be important when determining the exact moment of connection and the further development of the sea level (Giosan et al., 2006). It was found that the disappearance of ice sheets has a significant effect on the height of the sill of the Bosphorus strait and that the magnitude of the effect differs per location. Schroeder et al. (2012) reviewed knowledge on climate in the Mediterranean region and assessed the water exchange with the Black Sea through the Sea of Marmara. They conclude that the strait exchange is currently a two-layer system, and address the directionality and magnitude of the flows as a function of the density structure of the strait and the fresh water budget of the Black Sea. However, none of these studies discuss the transient response. The hydrodynamic Black Sea model presented in this paper is an adaptation of the box model for the Mediterranean Sea described in chapter 3. The phosphorus dynamics are modelled using a modified version of a biogeochemical model for the ocean presented in Slomp and Van Cappellen (2007).

4.3 Methods

4.3.1 Circulation model

Figure 4.2 provides an overview of the boxes and the water fluxes of the circulation model, as adapted from chapter 3. The density of the water in each box is calculated as a function of salinity and temperature. We implement heat exchange in the form of a relaxation to an imposed atmospheric temperature. Following the setup of chapter 3, box 0 represents the Sea of Marmara, box 1 the shallow margin of the Black Sea in the north west, box 2 the upper 170 m of the open Black Sea, and box 3 the deep Black Sea spanning a depth range of 1725 m. The combined depth of boxes 2 and 3 are an approximation of the average depth of the main basin of the Black Sea. The narrow margins along other coast lines are ignored. The river discharge into box 2 is disregarded, since there are no major rivers entering this part of the Black Sea.

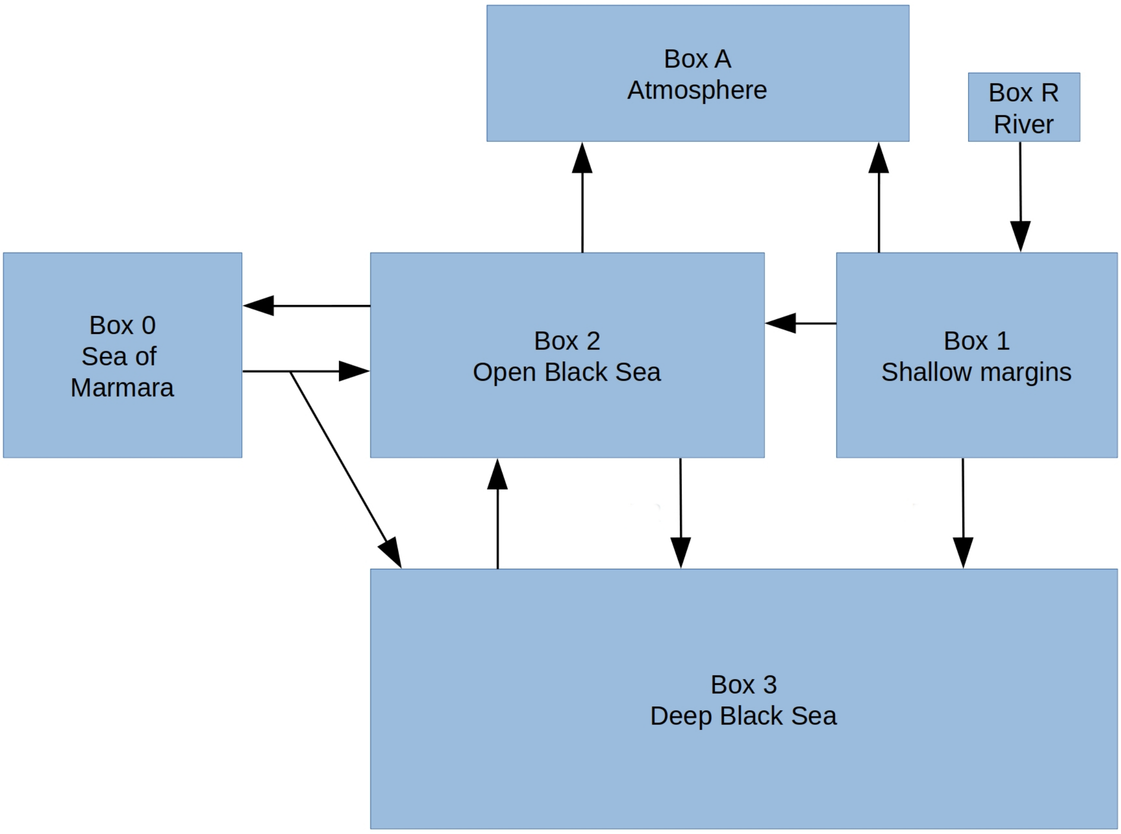

Figure 4.2 A schematic overview of the Black Sea water circulation model, which is an adaptation of the model in chapter 3. The arrows indicate water fluxes. A flux from the external basin, the Sea of Marmara, to the deep water is included in the model, as well as mixing between the inflowing water and the open and deep Black Sea boxes (not depicted). This allows the inflowing water to sink, provided its density exceeds the density of the deep water. The model parameters, given in table 4.1, reflect the characteristics of the Black Sea.

Name	Value	Units	Description
dt	1	yr	Time step
c_A	1.5	$W/(m^2 \cdot K)$	Sea to air heat transport efficiency*
c_{03}	0.5	$[-]$	Partitioning parameter of inflowing water**
c_{13}	$1.7 \cdot 10^5$	$m^6 \cdot (s \cdot kg)$	Water transport efficiency between box 1 and 3**
c_{fm}	$2.6e \cdot 10^{-4}$	s/m^3	Mixing parameter of the inflow water**
k_{12}	$1 \cdot 10^{-4}$	m^2/s	Horizontal mixing between box 1 and 2*
L	1000	m	Length scale of horizontal diffusivity*
k_{bg}	$1 \cdot 10^{-5}$	m^2/s	Background vertical mixing strength**
k_{str}	$2 \cdot 10^{-5}$	$m^5/(kg \cdot s)$	Vertical mixing strength parameter**
A	$4.23 \cdot 10^{11}$	m^2	Surface area of the Black Sea****
f	0.25	$-$	Fraction of the surface area covered by box 1****
d_1	40	m	Depth of box 1****
d_2	170	m	Depth of box 2****
d_3	1725	m	Depth of box 3****
S_0	30.092	kg/m^3	Salinity of the Marmara Sea inflow water***
T_0	12.92	$°C$	Temperature of the Marmara Sea inflow water***
T_{A1}	13	$°C$	Temperature of atmosphere box A1
T_{A2}	14	$°C$	Temperature of atmosphere box A2
T_{R1}	12.3	$°C$	Temperature of the rivers into box 1 ***
c_p	$4.187 \cdot 10^3$	$J/(K \cdot kg)$	Specific heat of water

Table 4.1 All circulation model parameters, excluding the model forcing. The subscript numbers refer to the box, e.g. c_{03} is the partitioning parameter for the flow from box 0 to box 3, while T_0 is the temperature of box 0. *chapter 3,**empirically determined, ***Bogdanova (1963),****Özsoy and Ümit Ünlüata (1997).

In the model runs we assume that the simulated sea-level change only affects strait exchange. The effect of the change in the volume of the main basin (boxes 2 and 3 in the model) is expected to be small, as this part of the Black Sea is 1895 m deep in the model, while the sea-level change is approximately 50 m. There could be an impact on the waters of the shallow margin, i.e. box 1. This part has a relatively large area with a depth of < 50 m. However, box 1 effectively only transports the freshwater of the various rivers to box 2. Due to the short residence time, the effects of evaporation and heat loss —which are a function of volume— are expected to be negligible. In the model runs presented here, the freshwater budget is always positive. A decrease in surface area would only cause a decrease in evaporation and thereby a more positive freshwater budget. Similarly, the effect of the sea-level change on the total volume of the Black Sea is very small and the volume of the shallow margins has very little impact on the model.

The deep flow through the Bosphorus (into the Black Sea) is parametrized to be proportional to the square root of the density difference; the factor of proportionality is referred to as the strait efficiency (chapter 3). In order to capture the effect of sea-level change we assume a linear relation between strait efficiency and strait depth ($d_{sill} = -40\ m$, Lane-Serff et al., 1997). This is a crude but effective way to capture the role of varying sea level on seaway exchange. We follow Lane-Serff et al. (1997) in using a critical sea level of 11 m above the sill as a requirement for two layer transport. In other words, the strait efficiency is 0 when the sea level is less than 11 m above the sill.

The present vertical density structure of the Bosphorus is used to obtain the current strait efficiency, allowing us to calibrate the relationship between sea level and strait efficiency.

$$c_{20-present} = \frac{Q_{dens}}{\sqrt{|(\rho_0 - \rho_2)|}} \tag{4.1}$$

Where $c_{20-present}$ is the present strait efficiency of the Bosphorus, Q_{dens} the present day density driven flow through the strait and ρ the density. The subscript numbers, 2 and 0, refer to the related boxes. We can now calculate the strait efficiency for a given sea level (SL, negative when below present):

$$c_{20} = max(0, c_{20-present} \cdot (1 - \frac{SL}{d_{sill} + 11}) \tag{4.2}$$

Where c_{20} is the strait efficiency for a given sea level (SL) and sill height (d_{sill}). We use the notation $max(a, b)$ in the same way as in chapter 3. This value is then used to calculate the density driven flow of water through the strait, following chapter 5:

$$Q_{mb} = \begin{cases} c_{20} \cdot \sqrt{|\rho_2 - \rho_0|} & \text{for} \quad \rho_2 \leq \rho_0 \\ 0 & \text{for} \quad \rho_2 > \rho_0 \end{cases} \tag{4.3}$$

$$Q_{bm} = \begin{cases} c_{20} \cdot \sqrt{|\rho_0 - \rho_2|} & \text{for} \quad \rho_0 \leq \rho_2 \\ 0 & \text{for} \quad \rho_0 > \rho_2 \end{cases} \tag{4.4}$$

Where Q_{mb} is the density driven flux into the Black Sea and Q_{bm} the density driven flux out of the Black Sea. At present, the Bosphorus inflow is observed to disperse between the deep and intermediate water after entering the Black Sea (Bogdanova, 1963). This is accounted for in several ways, depending on the situation. Following Boudreau et al. (2022), when the density of the inflowing water exceeds that of the deep water, part of it is taken to sink directly into the deep box while the rest flows into the surface/intermediate box. Thus, a flux from box 0 to box 3 is added to represent the sinking of the inflowing Marmara Sea water into the deep Black Sea.

$$F_{03} = \begin{cases} c_{03} \cdot Q_{mb} & \text{for} \quad \rho_0 > \rho_3 \\ 0 & \text{for} \quad \rho_0 \leq \rho_3 \end{cases} \tag{4.5}$$

Where F_{03} is the water flux from box 0 to box 3. Generally F_{ij} refers to the flux from box i to box j. c_{03} represents the fraction of the density-driven inflow that feeds into the deep water. When the density of the inflowing water is higher than that of the surface box, but lower than the deep water, we assume that part of it mixes with the deep water (in accordance with Boudreau et al., 2022). The fraction of the inflowing water that mixes with the deep water scales with the magnitude of the inflow, simulating the effect of the intermediate water lens that is observed to form under such conditions (Boudreau et al., 2022). Provided $rho_0 < rho_2$ and $rho_0 < rho_3$ the amount of inflowing water that mixes with the deep water is calculated as:

$$m_{03} = \begin{cases} min(1, Q_{mb} \cdot c_{fm}) \cdot k_{bg} \cdot \frac{A_2 \cdot 2}{d_2 + d_3} & \text{for} \quad \rho_0 \leq \rho_3 \\ 0 & \text{for} \quad \rho_0 > \rho_3 \end{cases} \tag{4.6}$$

Where m_{03} is the mixing between box 0 and 3, c_{fm} the flux scaling parameter and k_{bg} is the background mixing paramter. A_2 is the area of box 2 and d_2 and d_3 the depths of boxes 2 and 3 respectively. The function $min(a, b)$ selects the smallest of the two values (similar to how $max(a, b)$ is used to select the maximum). This prevents the area of the intermediate water lens from exceeding the surface area of boxes 2 and 3.

The inflowing water that does not sink to the deep water flows into box 2. Combined with the density driven and compensating fluxes this yields the inflow from box 0 to box 2:

$$F_{02} = Qmb + Qbm - F_{03} + max(0, -fwbtot) \tag{4.7}$$

Where $fwbtot$ is the total freshwater budget of the entire basin, at the relevant time step. Similarly, the flux out of the Black Sea is then:

$$F_{20} = Qmb + Qbm + max(0, fwbtot(t)) \tag{4.8}$$

When the density of the open Black Sea surface water exceeds that of the deep water, the instability is resolved through convective adjustment. Note that the down going flux is compensated by F_{32}, making the combination of these fluxes effectively act as mixing. The amount of water exchanged is of such a magnitude that the densities of the two boxes is the same after one time step. We found that this analytical solution is independent of the density of the boxes and therefore constant. This formula, equation 4.9, for deep convection in the open Black Sea reflects convective adjustment more accurately, following the approach of chapter 5.

$$F_{23} = \begin{cases} \frac{V_2 \cdot d_2}{(1-f) \cdot d_3 + d_2} & \text{for} \quad \rho_2 > \rho_3 \\ 0 & \text{for} \quad \rho_2 \leq \rho_3 \end{cases} \tag{4.9}$$

Where V_2 is the volume of box 2 (i.e. $d_2 \cdot A_2$) and f the fraction of the surface area of box 1, relative to the surface area of the Black Sea (i.e. $f = A_1/A$). The heat exchange with the atmosphere remains unchanged from chapter 3. In the present model runs the atmospheric temperatures (TA_1 and TA_2) are constant. A sensitivity analysis (not shown) indicates that atmospheric temperature variability does not significantly impact the results. The other water model equations are unchanged from chapter 3.

4.3.2 Nutrient model

The dynamics of phosphorus, which is assumed to be the limiting nutrient for phytoplankton growth (e.g. Ludwig et al., 2009; Slomp and Van Cappellen, 2007), and deep water oxygen are derived from the water fluxes calculated by the circulation model. This replaces the approach to capture deep-water oxygen consumption presented in (chapter 3). Figure 4.3 provides an overview of the processes in each box. All equations are given in section 4.3.3.

Phosphorus (P) is present as soluble reactive phosphorus (SRP) and particulate organic phosphorus (POP). SRP follows the water fluxes, can be transformed into POP by primary production (PP) in the upper boxes, and is buried as P bound to authigenic ferric iron oxides (FeP) or as authigenic carbonate fluorapatite (CaP) in boxes 1 and 3, following Slomp and Van Cappellen (2007). Primary production is a function of the SRP concentration in each of the surface boxes. CaP burial depends on the oxygen and SRP concentrations, while FeP only depends on the SRP and oxygen concentration. In contrast to SRP, POP does not follow the water fluxes. It can be exported to the deep box (independent of the water fluxes), degraded into SRP, or partly buried. POP export only occurs in box 2 and depends on the rate of PP. In the upper boxes, the transformation of POP into SRP depends on PP. In the deep water, we assume that a fixed part of the exported POP is transformed into SRP. POP burial is a function of the amount of POP and the oxygen concentration. Burial only occurs in boxes 1 and 3. We assume a linear relationship between POP and particulate organic carbon in the water collumn, since it concerns the same organic matter. Oxygen consumption can then be derived from POP degradation. Organic rich deposits form when there is bottom water anoxia and sufficient burial of organic matter. Deep water POP and the deep water oxygen concentration therefore control organic carbon burial in the model. The model thus allows us to directly study the parameters that control the formation of these deposits.

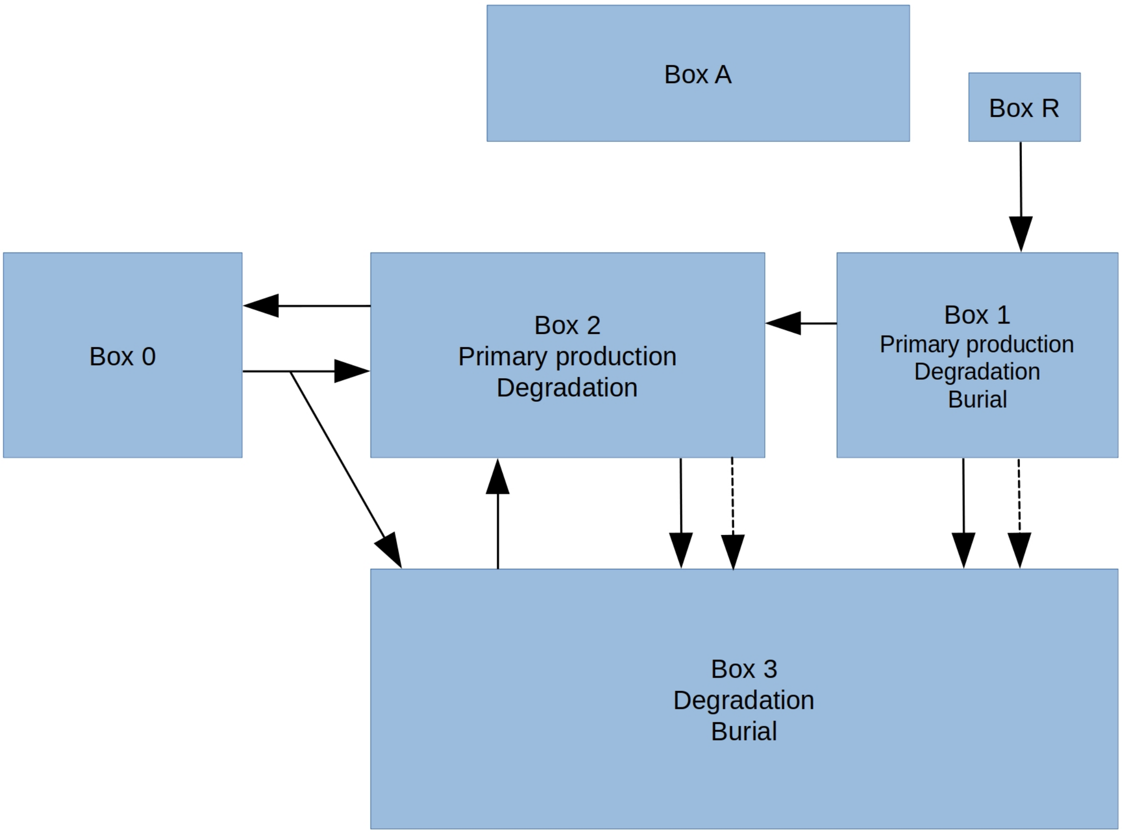

Figure 4.3 A schematic overview of the nutrient model. The box labels indicate which nutrient model components (primary production, degradation and burial) are applied to each of the three boxes. The solid lines represent water fluxes obtained from the circulation model that carry SRP. The dashed lines represent the sinking of POP. Note that there is no exchange of nutrients with the atmosphere (Box A).

4.3.3 Nutrient model equations and parameters

In this subsection we discuss the nutrient model equations, describing interactions between the various boxes as shown in Figure 4.3. All parameters are given in table 4.2. The subscript numbers refer to the box.

Primary productivity, PP (in $mmol\ m^{-3}\ s^{-1}$), in the upper boxes, 1 and 2, is linearly dependent on the SRP concentration (in $mmol\ m^{-3}$) in the relevant box, because phosphorus is assumed to be the limiting nutrient. kPP_1 and kPP_2 are rate constants for primary production in s^{-1}.

$$\begin{aligned} PP_1 &= max(0, kPP_1 \cdot SRP_1), \\ PP_2 &= max(0, kPP_2 \cdot SRP_2) \end{aligned} \tag{4.10}$$

Export of POP, i.e. $POPexp$, which only occurs in box 2, is linearly dependent on primary productivity in box 2. We thereby assume that a fixed fraction, $kPOPexp$, of POP is exported.

$$POPexp = kPOPexp \cdot PP_2 \tag{4.11}$$

The phosphorus release as a result of POP degradation, in boxes 1 and 2, $Prel$, is linearly dependent on the primary production in the corresponding box.

$$\begin{aligned} Prel_1 &= kPrel_1 \cdot PP_1, \\ Prel_2 &= kPrel_2 \cdot PP_2 \end{aligned} \tag{4.12}$$

Where $kPrel$ is a constant. The degradation of organic P in the deep water, $Prel_3$, is linearly dependent on the POP export into box 3.

$$Prel_3 = kPrel_3 \cdot POPexp \tag{4.13}$$

The fraction of POP that is buried at each time step, $POPbur$, depends on the oxygen concentration O relative to the reference oxygen concentration $Oref$. POP burial does not occur in box 2, as there is no sediment directly below the box. $kPOPbur$ is a constant.

$$\begin{aligned} POPbur_1 &= kPOPbur_1 \cdot POP_1 \cdot (0.75 + 0.25 \cdot O_1/Oref), \\ POPbur_3 &= kPOPbur_3 \cdot POP_3 \cdot (0.75 + 0.25 \cdot O_3/Oref) \end{aligned} \tag{4.14}$$

Burial of SRP can occur either in the form of FeP or CaP, following Slomp and Van Cappellen (2007). Both scale with the SRP concentration in the relevant box, FeP burial also depends on the oxygen concentration. $kFeP$ and $kCaP$ are constants.

$$\begin{aligned} FeP_1 &= kFeP \cdot SRP_1 \cdot O_1/Oref, \\ FeP_3 &= kFeP \cdot SRP_3 \cdot O_3/Oref \end{aligned} \tag{4.15}$$

Where FeP is the SRP burial flux in the form of FeP.

$$\begin{aligned} CaP_1 &= kCaP \cdot SRP_1 \cdot (0.5 + 0.5 \cdot O_1/Oref), \\ CaP_3 &= kCaP \cdot SRP_3 \cdot (0.5 + 0.5 \cdot O_3/Oref) \end{aligned} \tag{4.16}$$

Where CaP is the SRP burial flux in the form of CaP. Part of this flux is dependent on the oxygen concentration, we estimate this to be in the order of 50%. The sum of these two SRP burial components yields the total SRP burial:

$$\begin{aligned} SRPbur_1 &= FeP_1 + CaP_1, \\ SRPbur_3 &= FeP_3 + CaP_3 \end{aligned} \tag{4.17}$$

Degradation of organic matter is the only process that consumes oxygen in the model. For each mol of carbon released, one mol of oxygen is consumed. The Redfield ratio between C and P, RF_{CP}, is used to calculate the organic carbon degradation from the POP degradation $POPrel$. The oxygen consumption, $Ocons$, is calculated as follows:

$$Ocons = \begin{cases} RF_{CP} \cdot POPrel_3 & \text{for} \quad O_3 > 0 \\ 0 & \text{for} \quad O_3 \leq 0 \end{cases} \tag{4.18}$$

The SRP, POP and oxygen concentration of each box for the next time step is calculated using the same method as for temperature and salinity. The oxygen concentration at the surface ($Osurf$) is taken to be constant and in equilibrium with the atmosphere.

Parameter	Value	Units	Description
RF_{CP}	106	$[-]$	The Redfield ratio of the elements C and P
SRP0	2	$[mmol\ m^{-3}]$	SRP of Marmara Sea water**
SRPR1	3	$[mmol\ m^{-3}]$	SRP of river water***
Osurf	325	$[mmol\ m^{-3}]$	Oxygen concentration at the surface
Oref	325	$[mmol\ m^{-3}]$	Reference Oxygen concentration
kPrel1	0.8	$[-]$	P release parameter for box 1*
kPrel2	0.8	$[-]$	P release parameter for box 2*
kPrel3	0.15	$[-]$	P release parameter for box 3*
kPP1	$3 \cdot 10^{-9}$	$[s^{-1}]$	PP parameter of box 1*
kPP2	$2.9 \cdot 10^{-9}$	$[s^{-1}]$	PP parameter of box 2*
kPOPexp	0.20	$[-]$	POP export parameter*
kPOPbur	$7 \cdot 10^{-11}$	$[-]$	POP burial parameter$^{*} * **$
kFeP	$8 \cdot 10^{-11}$	$[s^{-1}m^{-3}]$	A small fraction of total P burial is FeP$^{*} * **$
kCaP	$1.9 \cdot 10^{-10}$	$[s^{-1}m^{-3}]$	50% of total P burial is CaP$^{*} * **$
CPoxic	200	$[-]$	The oxic CP ratio
CPanoxic	1100	$[-]$	The anoxic CP ratio
mmolC2ktC	$12 \cdot 10^{-12}$	$[kt\ mmol^{-1}]$	The weight of a $mmol$ C in kt

Table 4.2 All nutrient model parameters, as used in the results, section 4.5. *Adapted from Slomp and Van Cappellen (2007), **Tugrul et al. (2002), ***Lancelot et al. (2002).**** The kPOPbur, kFeP and kCaP parameters are chosen such that POP burial and CaP burial contribute equally to the total P burial, while FeP only contributes a small fraction.

Next we calculate the organic carbon burial for comparison with the geological record. To do so, we first determine the ratio of buried POC to buried POP, CP, following Cappellen and Ingall (1994):

$$CP = \frac{(CP_{oxic} \cdot CP_{anoxic})}{(O_3/O_{ref}) \cdot CP_{anoxic} + (1 - (O_3/O_{ref})) \cdot CP_{oxic}} \tag{4.19}$$

Where CP_{oxic} refers to the CP ratio under oxic conditions, while CP_{anoxic} refers to the CP ratio under anoxic conditions.

The buried POC is given by multiplying CP with the buried POP and converterted into kilotons per year.

$$POCbur = CP \cdot POPbur_3 \cdot V_3 \cdot dt \cdot mmolC2ktC \tag{4.20}$$

4.4 Sea level curve

The first experiment described below, a constant sea level is used, which only allows for one way transport. The sea level curves used to force the subsequent model experiments are calculated with the following set of empirical formulas. An empirical sea level curve is composed of a harmonic oscillation and an exponential curve. First the harmonic oscillation is calculated, i.e. a sine wave where Δ is the amplitude (set to 0 to obtain a monotonic increase), ϕ the phase, P the period and t the time vector:

$$D = \Delta \cdot sin\Big(2\pi \cdot \frac{t+\phi}{P}\Big) \tag{4.21}$$

Next, the exponential curve is added to the oscillation (equation 4.21), where $a \cdots d$ are empirical constants and t_{open} is the point in time when the water level exceeds the sill:

$$SL_{curve} = a + b \cdot \Big(1 - e^{-c \cdot (t - t_{open})}\Big) + d \cdot t + D \tag{4.22}$$

Finally all calculated sea level values below the sill height are set to be equal to the sill height, since the sea level no longer affects the Black Sea if it does not exceed the sill:

$$SL = max(D_{strait}, SL_{curve}) \tag{4.23}$$

All parameters used to calculate the sea level curves, see table 4.3, have been determined empirically to approximate the sea level curves shown in Kislov (2018), Boudreau et al. (2022) and references therein.

Parameter	Value	Units	Description
a	-55.1	$[m]$	Offset of the sea level curve
b	51.3	$[m]$	Exponential shaping parameter
c	$-4.0 \cdot 10^{-4}$	$[-]$	Magnitude of the exponent
d	$2.5 \cdot 10^{-4}$	$[m]$	Linear slope parameter
Δ	$0,\ 9$	$[m]$	Amplitude of the harmonic oscillation*
P	4	$[kyr]$	Period of the harmonic oscillation
ϕ	4	$[kyr]$	Phase of the harmonic oscillation
D_{strait}	-35	$[m]$	Sill height relative to the current water level

Table 4.3 All forcing parameters. *The run in subsection 4.5.2 uses $\Delta = 0$, while $\Delta = 9$ for the run in subsection 4.5.

4.5 Results

4.5.1 One way strait transport

In the early Holocene, the Black Sea was likely fresh or weakly brackish (Soulet et al., 2010; Boudreau et al., 2022). The lacustrine conditions would have been associated with convection in winter, which would have flushed out any saline water remaining from the previous marine interval in typically tens of thousands of years (Lane-Serff et al., 1997). We assume that the Black Sea water was entirely fresh at the start of the model runs, in accordance with Soulet et al. (2010); Boudreau et al. (2022). With a higher salinity at the start of the model run, almost all salt is flushed out during the spin up, as predicted by Lane-Serff et al. (1997).

We first conduct an equilibrium experiment where the model forcing is constant in time and represents the state of the Black Sea prior to the opening of the Bosphorus, i.e. only one-way strait transport occurs. The sea level is not raised and the Bosphorus Strait only accommodates an outflow to compensate for the positive freshwater budget of the Black Sea. Typically a steady state is reached after a few $kyrs$, but note that the equilibrium time is not the same for all parameters. The oxygen concentration (Figure 4.4) reflects the equilibrium process well. The time required to reach this state mainly depends on the mixing intensity. In the equilibrium state, the temperature difference between the upper boxes causes a slow circulation, causing oxygenated bottom waters. The result is in accordance with the literature cited above.

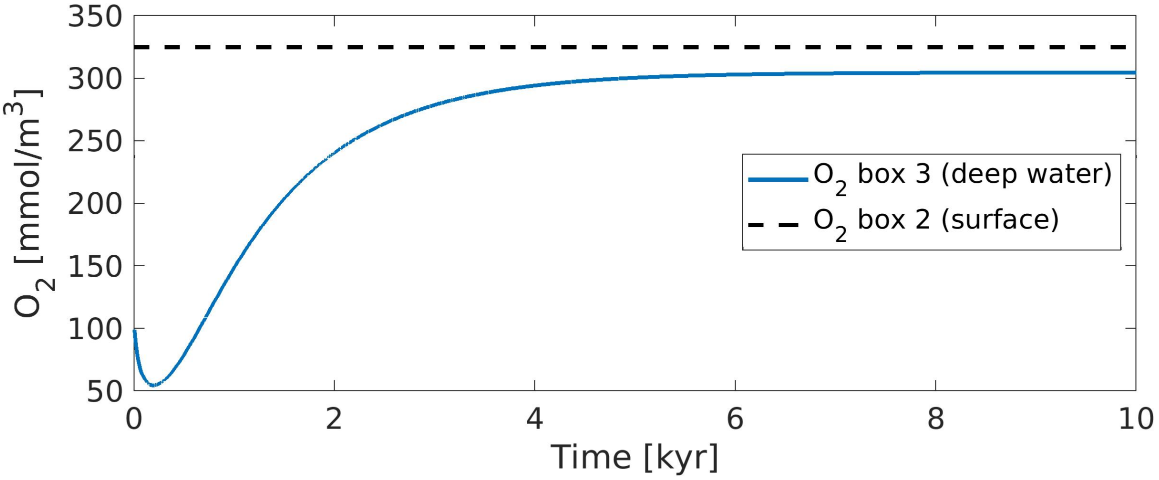

Figure 4.4 The oxygen concentration reaches a steady state after typically 4 $kyrs$ and approaches the surface concentration of 325 $mmol/m^3$.

4.5.2 Transient effects of opening the Bosphorus with a monotonic sea level rise

The results in Figure 4.5 concern a model run that represents Holocene sea level change (Kislov, 2018). All other forcing parameters are given in table 4.3. The shelf box (box 1) is not significantly affected by the opening of the Bosphorus Strait and therefore not extensively discussed. At the spin up ($t < 0$ kyr), the sea level is below sill height, only allowing excess water to flow out of the Black Sea; at the end of the spin up, the model is in the same equilibrium as described in the previous subsection: a weak circulation ($F13 > 0$, $F23 = 0$) with oxic bottom waters. The sea level is raised, as shown in Figure 4.5A, with a rate that is fast at the onset and then decreases over time. We define $t = 0$ kyr as the moment where the critical sea level is exceeded and the strait efficiency starts to increase, allowing two-way strait exchange, i.e. the opening of the Bosphorus. We identify three main time intervals: 1) the period where $t < 0$ kyr, where the strait is closed, 2) the time interval $0 < t < 2.2$ kyr, where strong convection occurs and 3) $t > 2.2$ kyr where convection has stopped and the system approaches the present equilibrium. As stated above, the situation during the first interval is identical to the equilibrium condition described in subsection 4.5.1.

When the Bosphorus opens and the second interval starts, the following sequence of events is triggered. Saline water, originating from the Mediterranean Sea, flows from the Sea of Marmara into the Black Sea, causing the salinity of the Black Sea to increase (Fig. 4.5B). The density of the surface box exceeds that of the deep box, triggering a brief period of sustained deep convection: the deep-water formation flux F_{23} in Figure 4.5C is high. The increasing salinity of the Black Sea causes its density to approach that of the Sea of Marmara, thereby reducing the inflow into the Black Sea (not shown). In turn, this reduces the volume that flows into the surface, which increases the relative impact of river discharge into the Black Sea, decreasing the surface salinity relative to the deep salinity. Eventually this stops the deep convection. In the third interval, after the convection stops, the only remaining source of deep water formation is the fraction of the inflowing Marmara Sea water that descends into box 3 (F_{03}). The salinity is found to stabilize after $\sim 10\ kyr$. This result thus implies that the present Black Sea has not yet reached its equilibrium, as already pointed out by Soulet et al. (2010).

The transient response of the water circulation has a major impact on the nutrients: the opening of the strait introduces a new source of nutrients for box 2, namely box 0 (corresponding to the Sea of Marmara). This results in an increase in SRP_2 (Figure 4.5D), which, through increased productivity and export of POP to the deep water, also causes an increase in POP_3 (Figure 4.5E) and POC burial in box 3 (Figure 4.5F). The deep water oxygen concentration (Figure 4.5F) remains high, since the convection and inflowing water from the Sea Of Marmara supply sufficient oxygen from the surface.

When the convection stops, i.e. the third interval, the system approaches a new equilbrium. SRP_2 increases as the inflowing nutrients are no longer transported to the deep water by the convection. This in turn causes the productivity and POP_3 to further increase. The high deep water POP causes increased oxygen consumption, which, combined with the slow circulation, results in a depletion of deep water oxygen. This effect is also reflected in the increased CP ratio and deep water POC burial. The nutrient parameters and oxygen reach an equilibrium after approximately $\sim 7\ kyr$. The POC burial in the deep water has no distinct “layer” that could be identified as a separate sedimentary unit in a hypothetical geological record, since the POC burial monotonically increases after the opening.

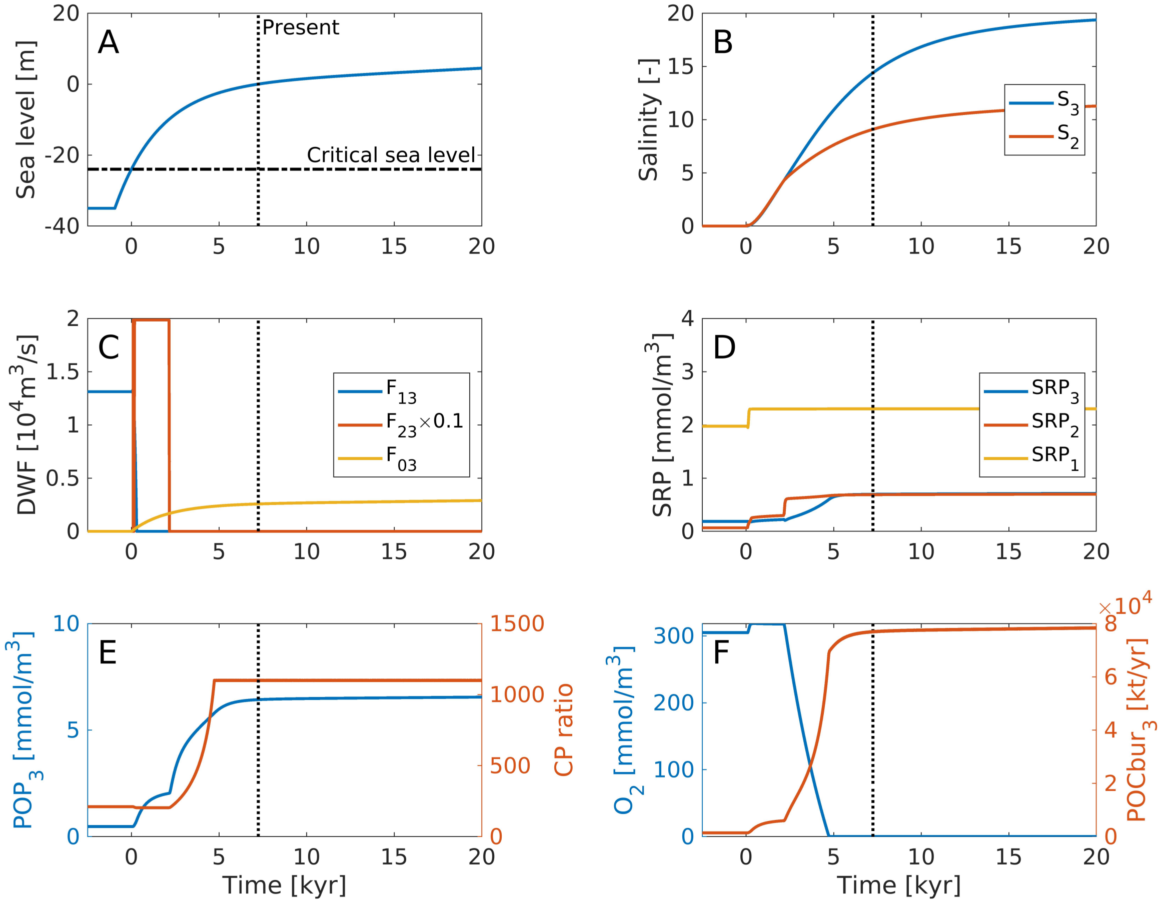

Figure 4.5 **A**: The sea level variation in time represents option (1), i.e. a monotonic increase. Time=0 represents the opening of the strait and the vertical dashed line the present. The horizontal dashed-dotted line represents the critical sea level, above which two-way strait transport occurs. Sea level=0 is the present sea level. **B**: The evolution of the salinities of each of the dynamic boxes through time. **C**: The deep-water formation (DWF) versus time. F_{23} is depicted after division by a factor of 10 for better comparison. **D**: Soluble reactive phosphorus (SRP) for boxes 1, 2 and 3 versus time. **E**: Particulate organic phosphorus (POP) for box 3 versus time on the left axis and the CP ratio for box 3 on the right axis. **F**: The deep-water oxygen concentration versus time on the left axis and the POC burial for box 3 versus time on the right axis. For all panels, the numbers in the legends refer to the box number. E.g. S3 is the salinity of box 3, the deep water.

4.5.3 Non-monotonic sea level increase

The sea level curve of the Black Sea has significant uncertainties (Kislov, 2018, and references therein), it is therefore possible that the Holocene sea level increase was not monotonic. To investigate the impact of such a scenario on the circulation and the formation of organic rich deposits, we add a sine wave with a period of 4 kyr (Fig. 4.6) and an amplitude of 9 m to the sea level curve in Figure 4.5A. A sine wave modulation is a convenient way to implement a varying sea level in the model.

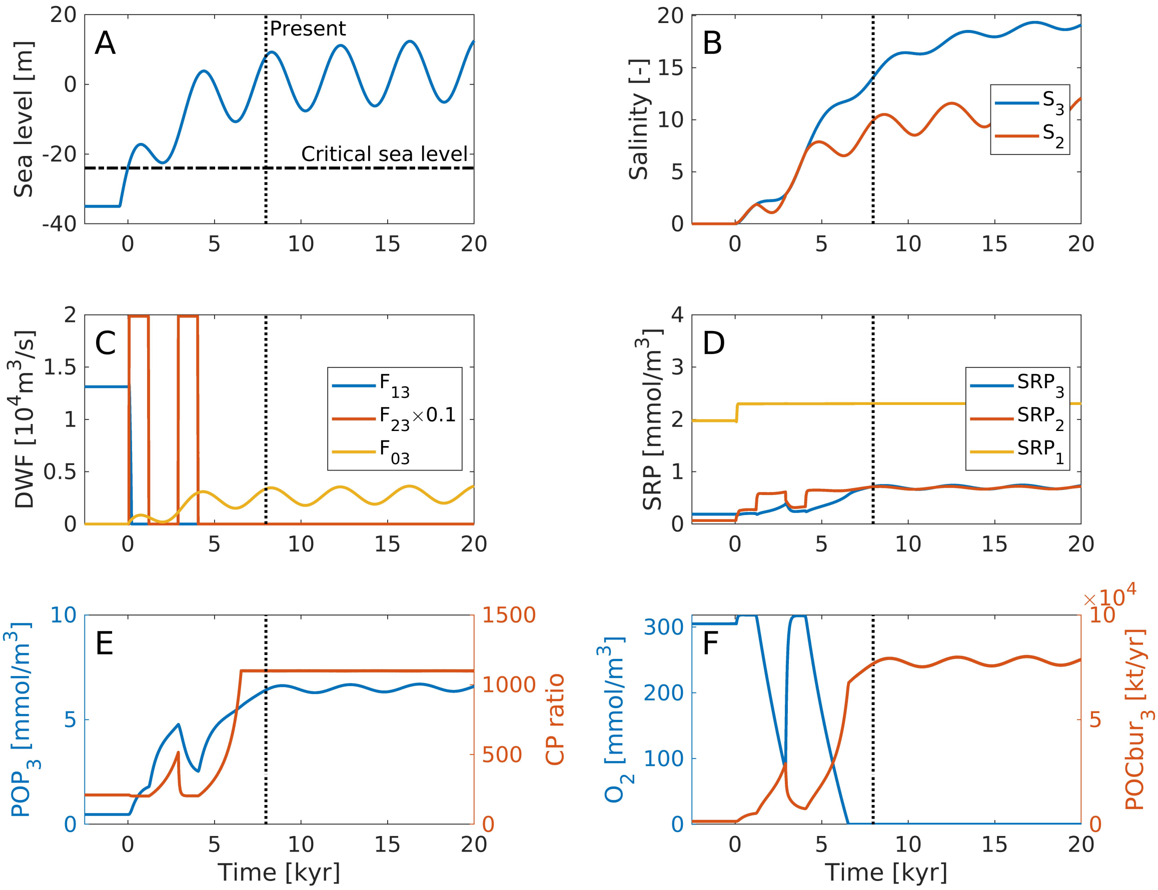

Figure 4.6 The results of the advanced sea level forcing. **A**: The sea level variation in time represents option (2), i.e. a non-monotonic increase. Time=0 represents the opening of the strait and the vertical dashed line the present. The horizontal dashed-dotted line represents the critical sea level, above which two-way strait transport occurs. Sea level=0 is the present sea level. **B**: The evolution of the salinities of each of the dynamic boxes through time. **C**: The deep-water formation (DWF) versus time. F_{23} is depicted after division by a factor of 10 for better comparison. **D**: Soluble reactive phosphorus (SRP) for boxes 1, 2 and 3 versus time. **E**: Particulate organic phosphorus (POP) for box 3 versus time on the left axis and the CP ratio for box 3 on the right axis. **F**: The deep-water oxygen concentration versus time on the left axis and the POC burial for box 3 versus time on the right axis.

During the initial increase in sea level, the same mechanism applies as described for the previous experiment: the opening of the strait causes the salinity to increase (Fig. 4.6B) and a peak in deep convection occurs shortly after two-way strait exchange starts (Fig. 4.6C). Next, the sea level drops, causing a decrease in strait efficiency, reducing the inflow from box 0. As a result of the decreased influence of the inflowing saline water, the salinity of box 2 decreases (Fig. 4.6B). Consequently, the density of box 2 decreases relative to box 3 and vertical convection stops: the basin briefly becomes stratified (between ~ 1.2 and ~ 2.9 kyr in Figure 4.6C). Note that two-way strait exchange does not have to stop for this behaviour to occur: a significant reduction in strait efficiency suffices. During the subsequent sea level rise, the salinity in box 2 increases and convection resumes in the period $2.9 < T < 4.1\ kyr$. After this second convection phase the circulation reaches the same final state as in the run in subsection 4.5.2. For other possible sea level curves, the alternation between the convection and stratification state continues until the inflow from box 0 to box 2 is no longer sufficient to cause deep convection. Finally, the basin always approaches its current dynamic equilibrium, where it is mostly stratified, with only some of the inflowing water from the Sea of Marmara sinking to the deep-water. The nutrients behave largely the same as in the run in subsection 4.5.2 and we therefore limit the description to the differences. A remarkable difference occurs in the stratified phase in between the convection peaks, i.e. $1.2 < T < 2.9\ kyr$. At $1.2kyr$, the system approaches a new dynamic equilibrium. Again, the lack of convection keeps the nutrients in box 2, causing high SRP_2, POP_3 and POC burial, as well as a decrease in deep water oxygen. When the convection resumes at $2.9\ kyr$, the SRP rich water in box 2 is mixed with low SRP water of box 3, resulting in a decrease in SRP_2 and, consequently, in productivity, as well as POP_3. The deep water POC burial decreases, but remains higher than during the first convection peak. After the final convective phase, the nutrients approach a similar dynamic equilibrium as in the run presented in subsection 4.5.2. Note that a ripple is found on most parameters in final dynamic equilibrium, due to the oscillating sea level. We conclude that a non-montonic sea level increase can cause a distinct peak in organic carbon in the sediment.

4.6 Discussion

Our time dependent model, that combines water flow and nutrient dynamics, shows complex behaviour that cannot be captured by equilibrium models. This allows to gain insights on organic carbon burial and the effects of the opening of the Bosphorus, as well as the impact of various parameters. The equations for inflow through the Bosphorus are adjusted to accommodate a factor that forces part of the inflow into the surface water, even if the inflow is more dense than the surface water. This captures the mixing that occurs between the surface water and the inflow, whilst the inflow travels into the basin and to the deep water (Bogdanova, 1963). This partitioning factor is primarily necessary to compensate for the assumption that sinking of the Bosphorus inflow is solely based on density, which would cause the entire inflow to sink to the deep basin, which is not observed. Forcing the flow to split between the surface and deep box allows us to capture this behaviour without having to include small-scale hydrographic processes. The associated scaling parameter (c_{03} of equation 4.5) primarily affects deep-water formation (F_{23}) and the steady-state salinity of the surface water. If a larger portion is forced into the surface box, the salinity in that box becomes higher and the deep-water formation peak after the opening of the Bosphorus becomes higher and wider. If less than $\sim 30\%$ of the inflow is forced into the surface water, the deep-water formation peak after the opening of the Bosphorus does not appear. If more than $\sim 80\%$ is forced into the surface water, the model does not reach stratification with present-day forcing. Between these two extreme values, variations only have a minor effect on the magnitude of the deep-water formation peak and consequent oxygenation of the bottom water. The Sea of Azov, connected to the Black Sea through the Strait of Kerch (Fig 4.1), was not included in the model because it has very limited exchange with the Black Sea. It has a positive freshwater budget due to the riverine flux from the Don (Kosarev et al., 2008). Compared to the Black Sea, the Sea of Azov is very small and transport through the very shallow Strait of Kerch (maximum depth 14 m, Kosarev et al., 2008) is limited.

The nutrient model calculates how and when anoxia occurs in the water column. The only process consuming oxygen in the deep-water box is organic matter degradation. The export of organic matter from the surface is the only source for the deep water, any form of chemosynthesis is not taken into account. This organic carbon can only be removed through degradation or burial. Hence, two potential mechanisms could cause the oxygen concentration to decrease: either the supply of oxygen is reduced, or primary production increases, which indirectly increases oxygen consumption. In chapter 3 we use a much more simple formula to quantify bottom water ventilation. When using this formula instead of the nutrient model in the runs presented here, we find very similar results (not shown). This indicates that the formula used in chapter 3 is a reasonable first order estimate. The main advantage of the nutrient model is that it also gives insight into nutrient dynamics and quantifies organic carbon burial.

A limited increase in the modelled deep-water oxygen concentration occurs directly after the opening of the Bosphorus, due to increased deep-water formation, transporting dissolved oxygen to the deep water (Figure 4.5). This interval also shows an increase in organic carbon burial. Arthur and Dean (1998) concluded, based on organic carbon measurements, that a period of enhanced vertical mixing did indeed follow the opening of the Bosphorus and estimated that period to last less than 2 $kyrs$. These authors did not find any evidence for a short-term increase in ventilation of the bottom waters during this period and conclude that increased organic carbon in the sediments is caused by increased PP. These findings are in agreement with our results. They conclude that the organic rich deposit is terminated by a decrease in primary productivity. The latter effect is only observed if a non-monotonic sea level increase is assumed, as demonstrated in Figure 4.6, where a decrease in SRP_2 coincides with the peak in carbon burial at 2.9 kyr. However, literature does not describe multiple deep convection intervals. The modelled organic carbon burial prior to the opening is similar to the amount found in unit 1, as defined in Teodoru et al. (2007), whereas the modelled burial after the opening is much higher. Potentially, the model overestimates organic carbon burial under anoxic conditions. Other explanations are also possible, e.g., the SRP concentration of the water flowing into the Black Sea may not have been constant through time. Both a non-monotonic sea level increase and non-constant SRP in the Marmara Sea water cause a decrease in the amount of SRP flowing into the Black Sea and thereby a decrease in productivity.

Geological data suggests that the organic rich layer formed when the water column was anoxic (Eckert et al., 2013), which we also find in our model. Wilkin et al. (1997) studied deep-water anoxia in the Black Sea using pyrite framboid size distribution as a proxy, with this size being smaller in anoxic basins. They recorded a decrease in size distribution around $\sim 7.8\ kyr$ and a size increase shortly prior to that interval. This was interpreted to indicate a period of oxic deep water followed by the onset of water column anoxia. They find the more oxic interval to have been short, which is largely in agreement with our model results. Absolute timing and duration are not reported in Wilkin et al. (1997), since they do not have an age model. Eckert et al. (2013) found evidence for an onset of anoxic deep water conditions at $\sim 7.6\ ka$. This is $\sim 1.4\ kyr$ after the opening of the Bosphorus Strait, indicating a shorter period with increased ventilation after the opening of the Bosphorus. Their analysis finds a single, but gradually established, peak in organic carbon content of the sediments. The start of this peak is interpreted as the only onset of anoxia in the deep water of the Black Sea, which, in view of our results, would indicate a largely monotonic rise in sea level.

4.7 Conclusions

A transient box model that combines water and nutrient dynamics can capture the main trends that result from the opening of the Bosphorus, as found in the geological record of the Black Sea. A sea-level curve with a series of transgressions and regressions can result in multiple intervals of bottom water oxygenation. Moreover, the model results suggest that this can happen while maintaining two-way strait exchange: when the strait efficiency decreases during the initial bottom water oxygenation interval, the surface salinity decreases as well, resulting in stratification. When the sea level rises again, strait efficiency increases, surface salinity increases and convection resumes. During the stratified interval in between the peaks in bottom water oxygenation, the deep water organic carbon burial is higher compared to the onset of bottom water anoxia with a monotonic sea-level increase. However, the results with a monotonic sea level curve have the best match with the geological record, because there is no evidence for a second convection phase.

5 A mechanism for high-frequency variability in sapropels

Based on: Dirksen, J. P., Meijer, P. (2022). A mechanism for high-frequency variability in sapropels. *Marine Geology*, 448, 106812, `https://doi.org/10.1016/j.margeo.2022.106812`.

Abstract

Sapropels deposited in the Mediterranean Sea provide high resolution records of past oceanographic changes. Previous studies have found abrupt transitions in chemical composition of these sediments. We present a transient box model that provides a potential mechanism for these transitions. The high-frequency variability is a result of fluxes stopping or changing direction, causing a relaxation towards a new equilibrium. The time scales depend on the volume of the reservoirs and the magnitude of the fluxes. We find typical periods in the order of 100-1000 years, similar to what has been found in a sediment core.
Keywords: sapropels, transient box model, high-frequency variability.
Sapropels deposited in the Mediterranean Sea provide high resolution records of past oceanographic changes. Previous studies have found abrupt transitions in chemical composition of these sediments. We present a transient box model that provides a potential mechanism for these transitions. The high-frequency variability is a result of fluxes stopping or changing direction, causing a relaxation towards a new equilibrium. The time scales depend on the volume of the reservoirs and the magnitude of the fluxes. We find typical periods in the order of 100-1000 years, similar to what has been found in sediment cores.
Keywords: sapropels, transient box model, high-frequency variability.

5.1 Introduction

Rapid changes as a result of a comparatively low-frequency forcing are of interest as they provide new insight into mechanisms that could affect climate change on human time scales. Here we study high-frequency variability in the Mediterranean Sea with a new transient box model. Previous studies on high-frequency variability mostly focused on high latitudes. The ice sheets are known to show significant variability on the Milankovitch time scales as well as on centennial to millennial time scales. They provide very high temporal resolution and also sufficient length to capture long

---

Picture left: A 9 Bft Storm with 7 m high waves on the Eastern Mediterranean Sea during cruise 64-PE406-E in January 2016. Deep water formation occurs in the Mediterranean Sea during such winter storms.

term variability, up to 2.7 Myrs (Bibby et al., 2016). Therefore, these records are ideal to study the impact of relatively slow variations on variability that occurs much faster. For example, relatively slow Heinrich events have been hypothesized to excite the faster Dansgaard–Oeschger cycles (Sampieri, 2002; Timmermann et al., 2003). In turn, Heinrich events are linked to much slower glacial-interglacial cycles which are forced by orbital variability, mainly on 100 *kyr* time scales (Timmermann et al., 2003). Another mechanism linking high and low-frequency variability is described in Starr et al. (2020): icebergs traveling further north from the Southern Ocean into the South Atlantic play a key role in the onset of the ice ages. This can only occur when sufficient cooling has already happened, typically due to Milankovitch variability. So, in this case, the low-frequency variability is a boundary condition for the fast variability, which in turn triggers low-frequency variability. At low latitudes, records of sufficient resolution and length to detect the interaction of Milankovitch and higher frequency variability are rare. Most records either lack the resolution due to bioturbation, insufficient sampling, or poor time control, or are limited to the last few thousand years (for example Mercone et al., 2001; Incarbona et al., 2011; Llave et al., 2006).

The geological record of the Eastern Mediterranean Sea contains regularly occurring organic-rich layers, called sapropels. The deposition of these layers coincides with increased Nile outflow due to enhanced African summer monsoon activity during precession minima (Rossignol-Strick, 1985; Rohling et al., 2015). This additional freshwater is hypothesized to form a lid on the Mediterranean Sea, slowing down or even stopping the circulation. The lack of circulation in turn stops bottom water ventilation, preserving organic matter and preventing bioturbation. Sapropels thus provide a high resolution record of changes in thermohaline circulation. Dirksen et al. (2019) observed such variability on multicentennial time scales in sapropel S5 in a core from the Levantine basin. Sierro et al. (2020) studied the sedimentary record of the Mediterranean outflow on the Atlantic side of the Gibraltar strait using sediment core data, linking changes in outflow velocity to the millennial scale variability of the Greenland ice sheet.

In this study we use a so-called box model. A box represents a homogeneous water mass, which interacts with the surrounding boxes. The interaction represents physical processes, such as convection and strait transport. Rather than calculating the water properties and circulation that are in equilibrium with a changed forcing (e.g., an insolation maximum), we use the model to follow the system as a function of time (for an entire precession cycle), doing justice to its transient nature. We represent the Mediterranean Sea by five dynamic water boxes. The boundary conditions are represented by additional boxes that have constant or predetermined properties. In Dirksen and Meijer (2020) we showed that a box model can capture the primary features of sapropel formation and give insight into timing and other fundamental mechanisms. This model, however, does not capture some of the high-frequency variability observed in proxy records (e.g. in sapropel S5, Dirksen et al., 2019). The extended model, with additional intermediate water boxes, presented here allows for more complex behaviour and can therefore be used to improve our understanding of processes that act on shorter time scales. We find that when a flux stops or reverses, the equilibrium state of most system variables changes significantly. This causes a fast transition towards the new dynamic equilibrium. This high-frequency variability is independent of the forcing frequency. The time scales are entirely dependent on the dynamics and sizes of the volumes concerned. Since the model has multiple boxes many transitions can occur in one run. The results imply that when interpreting high resolution proxy records, one should always be mindful that a significant part of the variability may be caused by non-linear internal processes instead of external forcing. For example, when fluxes change direction, a given water mass suddenly receives water from a different source, with different properties. That could cause a jump in, for example, temperature. When such a jump in temperature is observed in a geological record, one may erroneously conclude that very rapid climate change occurred. These principles apply to all records of past oceanographic and climatic variability. For sapropels in the Mediterranean Sea this implies that interruptions, sudden terminations and internal variability may largely be caused by the non-linear response of the ocean to much slower forcing.

5.2 Methods

To be able to study the more complex behaviour found in sediment cores, we introduce separate surface and intermediate boxes, while retaining the model framework of Dirksen and Meijer (2020). The main components of the extended model are explained here. A complete description of all model equations and details about the way these are combined and solved, can be found Dirksen and Meijer (2020) in combination with the annotated model code (see link to public repository near end of paper). Throughout this paper, we use Matlab as our computational environment. The layout of the model is shown in Figure 5.1. As in our previous paper we set out to capture the essence of the Mediterranean Sea and consider a single main basin ("open basin") connected to the Atlantic Ocean and having a single marginal sub basin. This allows us to focus on the primary effects of having a separate intermediate water layer. The properties of the Atlantic box are kept constant and the model is forced at the surface by prescribing the flux of freshwater (evaporation, precipitation and river discharge) and an atmospheric temperature to which the temperature of each surface box is relaxed. The present-day Mediterranean Sea has a small annual heat loss (Song and Yu, 2017). The model captures this by assuming perpetual winter conditions for the atmosphere, following Dirksen and Meijer (2020). As a consequence, the Atlantic box is always the water box with the highest temperature in the model. Forcings are defined separately for the open and the marginal box. Given these boundary conditions, the model uses conservation of water, salt and heat to solve for the salinity and temperature of the five Mediterranean boxes and for the magnitude of the water fluxes between the various parts.

While some of the fluxes are "compensating" (Figure 5.1) in that their value at any given point in time follows from the requirement to conserve volume, others are determined by the density difference between the interacting boxes. Density is calculated from salinity and temperature using the EOS80 formula (on Oceanographic Tables, 1986).

In both straits comprised by the model, the deeper of the two fluxes is considered density-driven. That is, horizontal flux at intermediate depth is from the box with higher density towards that with lower density. The flux is made proportional to the square root of the density difference, as would be appropriate for a hydraulically-controlled strait exchange (e.g. Meijer, 2021). The factor of proportionality is termed the coefficient of strait efficiency and its value is chosen a priori. If a strait accommodates intermediate-depth inflow into the open basin and the density of the water it carries exceeds that of the deep water, the flux will sink into the deep-water box. Also with reference to the vertical direction, convection is taken to occur when the density of the overlying box exceeds the density of the lower box. Convection consists of two fluxes that always flow in both directions simultaneously. In the model, the magnitude of these fluxes is linearly dependent on the density difference. Diffusive mixing is included as a constant ”flux” in the same formula. The total exchange in one time step is limited to the volume of the smallest box involved, to prevent unrealistic behaviour.

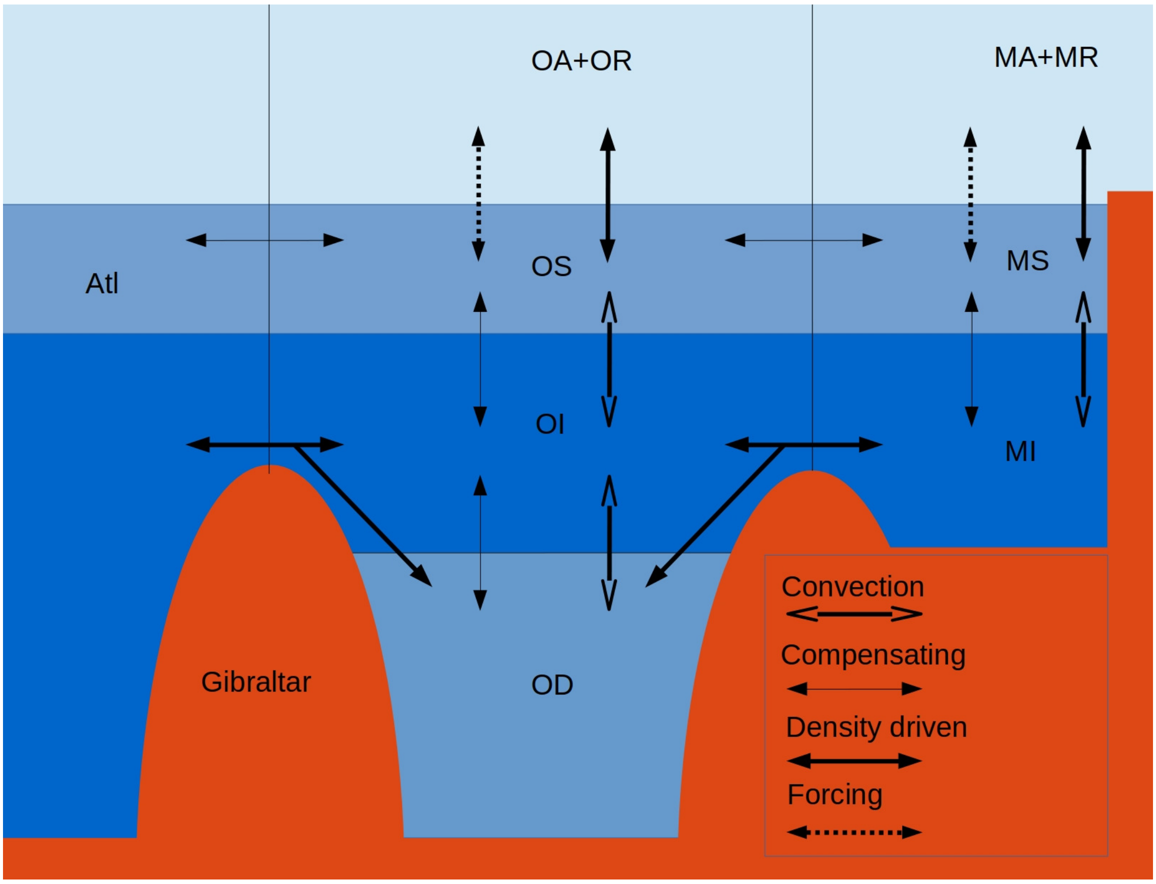

Figure 5.1 A schematic representation of the model, showing the Atlantic (Atl), Open Atmosphere (OA) and Open River (OR), Open Surface (OS), Open Intermediate (OI), Open Deep (OD), Marginal Atmosphere (MA), Marginal River (MR), Marginal Surface (MS) and Marginal Intermediate boxes are indicated. The margin represents the Aegean Sea and the Adriatic Sea and the Open basin represents Western basin, Eastern Basin, Levantine Sea and the Gulf of Lion (see Figure 5.6). The convection fluxes also include diffusive mixing. The "density driven" exchange with the atmosphere represents temperature relaxation. The forcing ecompasses both evaporation and river discharge.

The forcing function is a 20 *kyr* sine wave, representing climatic precession. This sine wave modulates river outflow and net evaporation (i.e. the difference between evaporation and precipitation) with realistic values. The other parameters, such as atmospheric temperature, are kept constant. The freshwater budgets of the surface boxes is made to change sign for part of the cycle (similar to Dirksen and Meijer, 2020). Although there is no evidence that the intermediate water flow at Gibraltar or Sicily changed direction, even during the most extreme anoxic events (Zahn et al., 1987; Rogerson et al., 2005; Schönfeld, 2002; Schönfeld and Zahn, 2000; Llave et al., 2006; Incarbona et al., 2011), it is likely that the freshwater budget of individual sub basins (or combinations thereof) did change sign. At present, marginal basins have a freshwater budget already close to zero (Zervakis et al., 2004; Raicich, 1996). Note that when the freshwater budget briefly changes sign, the direction of the intermediate water flow at the strait is not directly affected, since the intermediate current only changes direction when the density difference changes sign. Moreover, estimates of the increase of Nile discharge at sapropel times indicate that the freshwater budget of the Eastern Mediterranean may have changed sign (Amies et al., 2019). Aiming to study the effect of the freshwater budget of parts of the basin changing sign, we chose a forcing that emphasizes this behaviour. We present two model runs, for the first run the forcing is chosen to reflect the conditions during sapropel S5. Amies et al. (2019) found that the peak Nile outflow was eight times larger than present. We apply the same methodology to the Holocene sapropel, S1. Vadsaria et al. (2019) estimated that the Nile outflow during S1 was five times the present value, using a regional ocean–atmosphere coupled model, which includes simulations of ϵNd distribution. While the Nile flows into the open basin, our model is also very sensitive to the maximum river discharge into the marginal boxes for which, unfortunately, quantitative reconstructions are lacking. Therefore, besides a less augmented river discharge into the open basin, we use the same settings as for the S5 run to study S1.

The temperature, salinity and density of each box are calculated for each time step based on the exchange of properties with the surrounding boxes. We post-processed the resulting box temperatures with a so-called wavelet analysis, using the Matlab code from Torrence and Compo (1998), as described in Dirksen et al. (2019).

5.3 Results

The model results are shown in Figure 5.2 and 5.4. For the first run the forcing is chosen to reflect conditions during sapropel S5, while the second run uses a lower river outflow in the open basin to reflect S1 reconstructions.

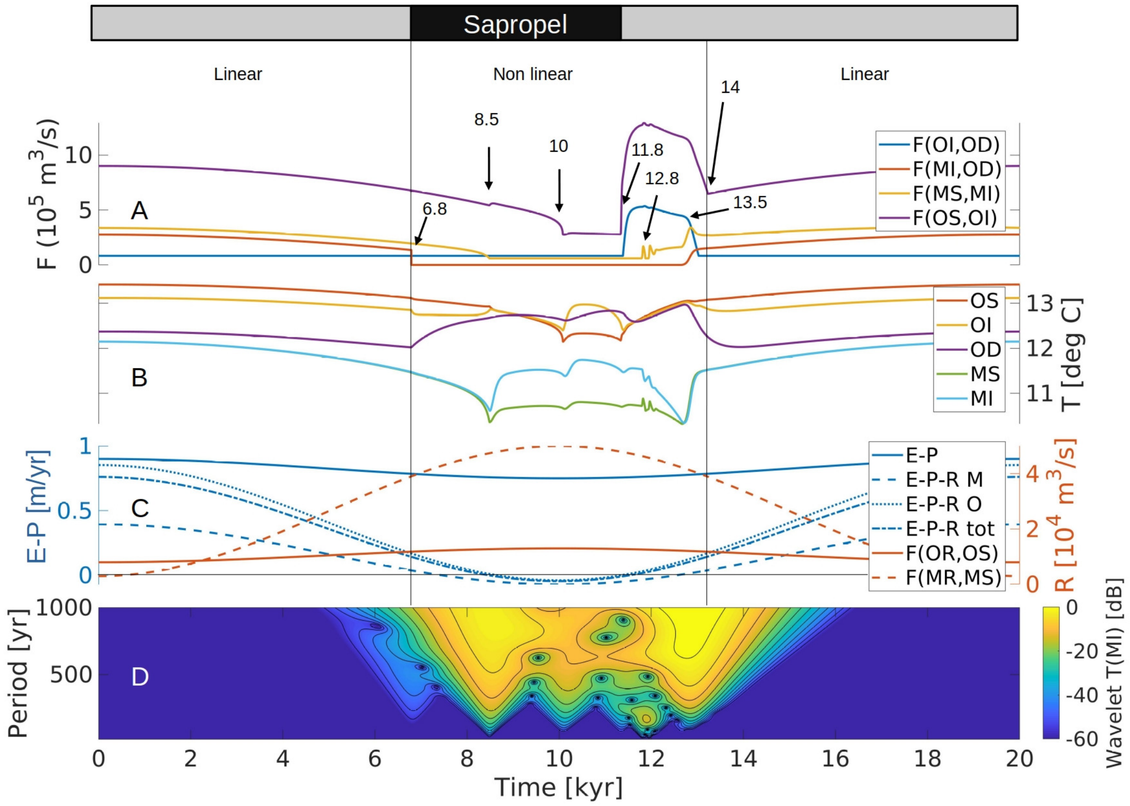

Figure 5.2 An overview of the model run. Time runs from left to right. **A:** all downward fluxes F in $[m^3/s]$, between the box combinations (OI,OD), (MI,OD), (MS,MI) and (OS,OI). The horizontal axis represents the time after spin up. The vertical lines indicate the transition from a linear to a non-linear regime where abrupt changes in fluxes occur. The arrows indicate the transitions in circulation and water properties indicated by the time in $[kyr]$. The "sapropel" interval, indicated by the black bar, is defined as the situation in which the only exchange with the open deep water box is background mixing with the overlying box. It starts at 6.8 kyr, when the deep water formation from the margins stops, and ends at 11.8 kyr, when deep convection in the open basin starts. **B:** the temperatures of the corresponding boxes. Note that when fluxes abruptly change, the temperature also changes significantly. **C:** the model forcing and freshwater budget for the various boxes. The horizontal black line indicates a freshwater budget of 0. The left vertical axis represents the net evaporation of the entire basin (E-P), and the freshwater budgets of each sub basins and the whole basin are shown in blue, in m/s. The right vertical axis represents the river outflow of each sub basin is shown in red, in 10^4 m^3/s. **D:** the wavelet analysis of the temperature of box MI. The colours indicate the spectral power of the frequencies through time in dB, yellow represents high power and blue low power. Wavelet analysis is a convenient tool to determine the periodicities of this time domain signal. Peaks and notches are found during the non-linear regime, typically in the range of 100-1000 years, much faster than the forcing.

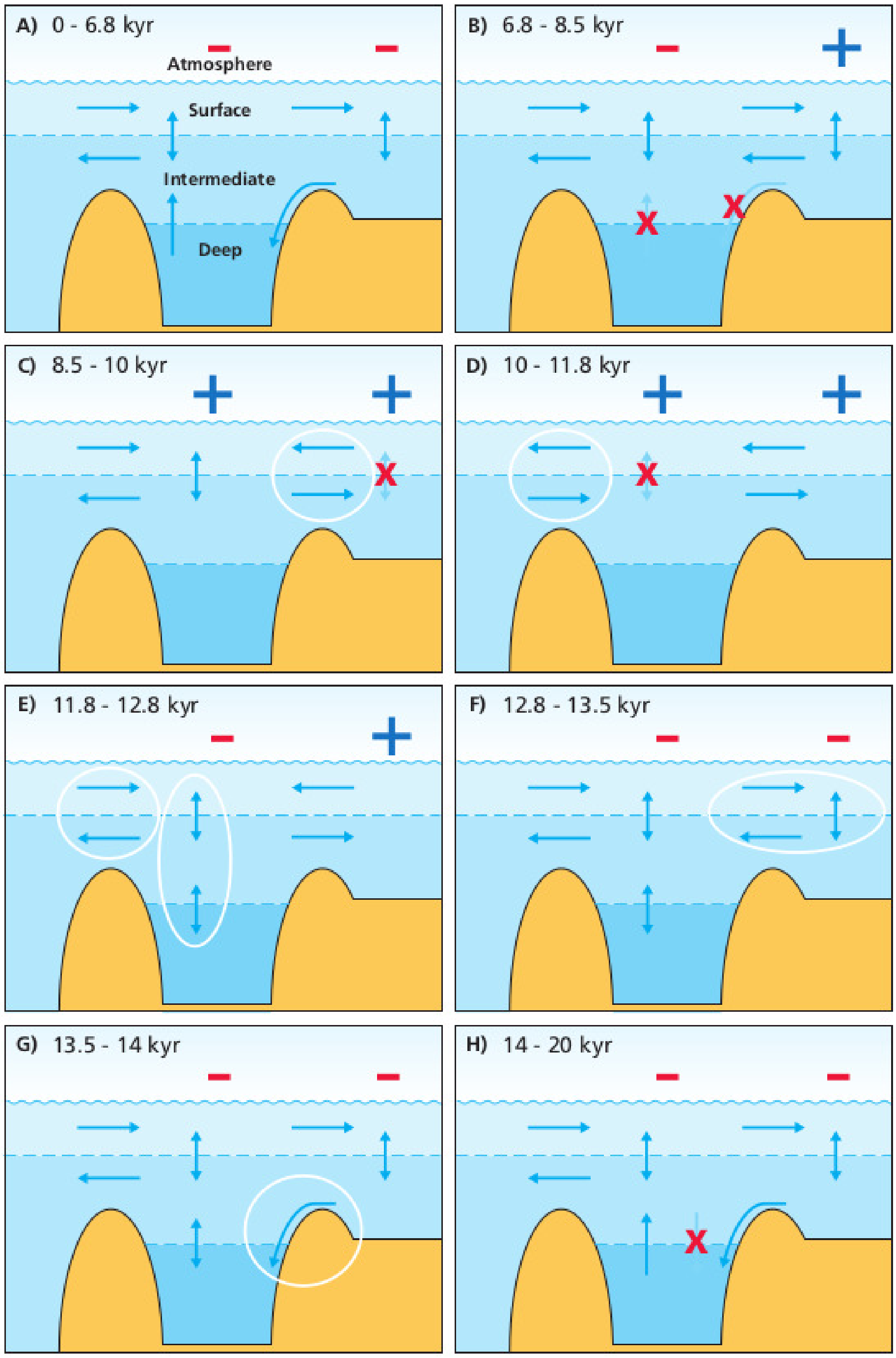

Figure 5.3 A schematic overview of the various states of the circulation according to the model run. Only the most important fluxes are shown. The signs in the atmosphere indicate the freshwater budget of the basins. A red minus indicates a negative freshwater budget, while a blue plus indicates a positive freshwater budget. The panels refer to the time intervals delineated by the arrows in figure 5.2, i.e. $0 - 6.8$ kyr, $6.8 - 8.5$ kyr, ..., $14 - 20$ kyr. The first panel is equal to the last panel, completing the cycle. New fluxes, or fluxes that changed direction are encircled, while vanishing fluxes are crossed out.

Three main intervals, delineated by vertical lines, can be identified in the S5 run: during the first 6.8 *kyr* the responds linearly to the forcing. The second interval, from 6.8 to 14 *kyr*, in which sapropel formation is predicted, is characterized by strong non-linear behaviour. Finally, in the third interval, from 14 *kyr* onward, the system returns to the initial state. Figures 5.2A-C show the vertical fluxes, box temperatures and model forcing respectively, while Figure 5.2D shows the wavelet transform of the marginal intermediate water temperature. Note that the non-linear interval shows multi-centennial variability. In this section we provide a detailed description of these results.

Previously we found that a change in sign of the freshwater budget of parts of the basin causes non-linearities, including a sudden termination of sapropel conditions (Dirksen and Meijer, 2020). As explained, we again assume a positive freshwater budget for part of the cycle, see Figure 5.2C. When fluxes stop or reverse direction, the equilibrium state changes abruptly. Consequently, the model relaxes towards this new equilibrium. This non-linear behaviour is unrelated to the forcing frequency. Generally, this process is expressed as a 'discontinuity' in the first derivative of, most prominently, temperature or volume flux, i.e. an abrupt change. The salinity and consequently density are much more directly affected by the forcing and therefore primarily show linear behaviour.

We describe the various states of the circulation found in the model run in Figure 5.2. A schematic overview of the circulation pattern of each state is given in Figure 5.3. At the start of the run, from 0 to 6.8 *kyr*, the circulation is in a linear regime, which is sketched in Figure 5.3A. Water flows into the open Mediterranean surface box to compensate for the density driven flux towards the Atlantic box and the fresh water deficit of both the marginal and open surface box. In the open surface box there is convection with the underlying intermediate box, a flux to the same intermediate box to compensate for the density driven outflow to the Atlantic box (this and other compensating vertical fluxes in addition to convection are not shown separately in Figure 5.3) and a compensating flux towards the marginal surface box. In the marginal surface box there is convection with the marginal intermediate box and a compensating flux towards the intermediate box to allow for conservation of volume. In the marginal intermediate box there is density driven flux towards the open boxes, which sinks to the open deep box. From the open deep box there is a flux to compensate for this deep water formation towards the open intermediate box. In the open intermediate box there is in turn a flux of the same magnitude towards the open surface box to compensate for the water coming from the deep box.

The system transitions to a non-linear regime at 6.8 *kyr*, shown in Figure 5.3B. The flux from the marginal intermediate box to the open deep box stops (Figure 5.2A) because the density of the marginal intermediate box no longer exceeds the density of the open deep box, due to the decreased net evaporation and increased river outflow (Figure 5.2C). Since the deep water box is only exchanging properties with the overlying intermediate box, its temperature starts to relax towards the temperature of the intermediate open box (Figure 5.2B). The time scale depends on the volume of the deep box and magnitude of mixing. The wavelet analysis in Figure 5.2D shows that the initial response is best described as a broad spectrum with emphasis on longer periods, with sharp notches, confined both in frequency and time, surrounding the peaks.

Next, at 8.5 *kyr*, the convection in the marginal boxes stops (Figure 5.2A and Figure 5.3C). This logically mainly affects the properties of the marginal boxes. The temperature of the intermediate water relaxes to a value closer to that of the open intermediate box because it has less interaction with the overlying box and water now flows into it from the open intermediate box. Furthermore, the salinity of the marginal surface box quickly decreases due to the increased river outflow and decreased exchange with the surrounding boxes with higher salinity.

The next major transition occurs at 10 *kyr* when the intermediate water exchange with the Atlantic reverses. As was the case for the marginal basin and illustrating what was pointed out in the Methods section, the reversal of exchange occurs well after the change in sign of the water budget: 1.6 *kyrs* later. Also at 10 *kyr*, the convection between the surface and intermediate water in the open basin stops (Figure 5.3D), i.e. complete stagnation occurs. The lack of exchange between the surface and intermediate water, besides background mixing, causes the open intermediate water conditions to relax to values closer to the Atlantic water, i.e. the temperature increases. Similarly, the marginal intermediate box now mainly exchanges water with the open intermediate box, causing the temperature to increase, albeit to a lesser extent. The deep water also relaxes to the open intermediate water conditions. The larger volume of the deep box and limited exchange result in a much slower relaxation. The surface boxes have a strong exchange with the atmosphere relative to the background mixing with the intermediate water boxes, resulting in a small temperature change.

After this point the freshwater budget starts to decrease again (E-P-R moving towards more positive values in Figure 5.2C). As a result convection occurs in all boxes of the open basin (Figure 5.3E). This abruptly ends the interval with minimal deep water ventilation. Although the deep water is now ventilated again, the circulation has not yet reached the equivalent of the present-day state. Two brief intervals of convection occur in the marginal basin at 11.8 *kyr* when buoyancy loss in the surface box occurs again (Figure 5.3F).

Next at 12.8 *kyr*, there is a brief interval with deep vertical convection, convection at the margins and deep water formation (Figure 5.3H). Finally, the deep convection stops and the equivalent of the present day circulation is reached at 13.5 *kyr* (Figure 5.3H). The deep water temperature only reaches dynamic equilibrium at roughly 14 *kyr*. Note that the open deep water box responds much slower than the other boxes at all transitions because it has a much larger volume.

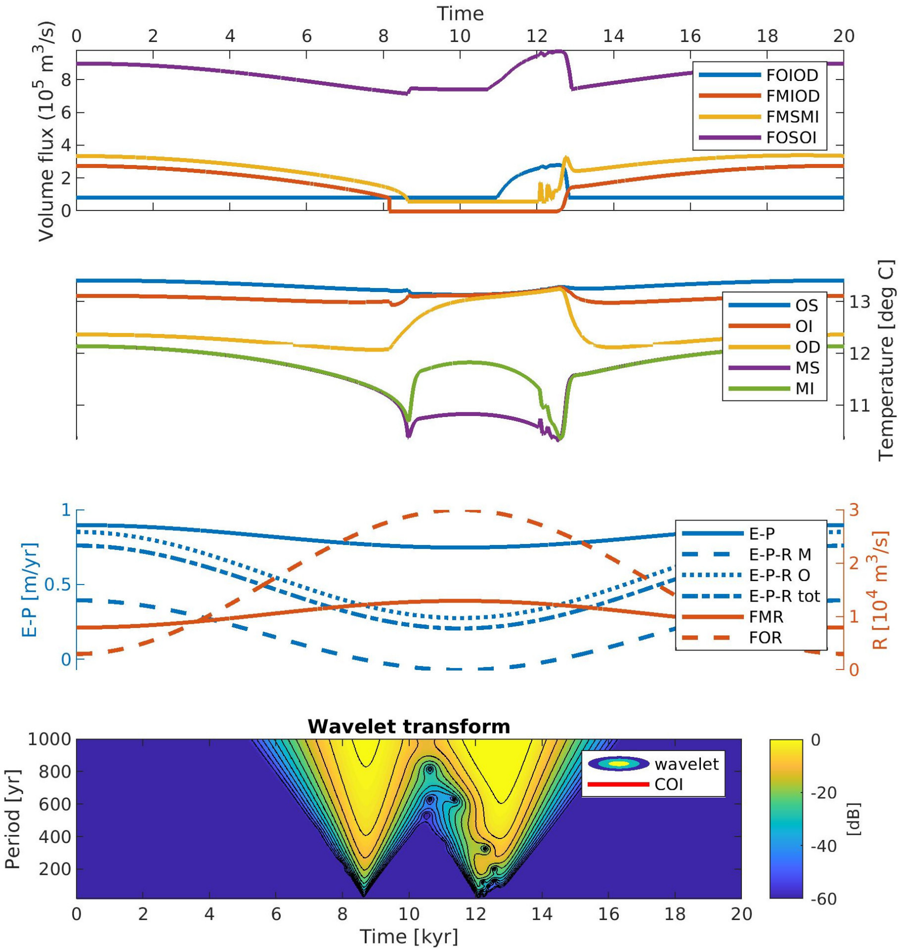

Figure 5.4 An overview of the S1 model run. Time runs from left to right. **A:** all downward fluxes F in $[m^3/s]$, between the box combinations (OI,OD), (MI,OD), (MS,MI) and (OS,OI). The horizontal axis represents the time after spin up. The vertical dashed lines indicate the transition from a linear to a non-linear regime where abrupt changes in fluxes occur. The arrows indicate the transitions in circulation and water properties indicated by the time in $[kyr]$. The "sapropel" interval, indicated by the black bar, is defined as the situation in which the only exchange with the open deep water box is background mixing with the overlying box. It starts at 6.8 kyr, when the deep water formation from the margins stops, and ends at 11.8 kyr, when deep convection in the open basin starts. **B:** the temperatures of the corresponding boxes. Note that when fluxes abruptly change, the temperature also changes significantly. **C:** the model forcing and freshwater budget for the various boxes. The left vertical axis represents the net evaporation of the entire basin (E-P), and the freshwater budgets of each sub basins and the whole basin are shown in blue, in m/s. The right vertical axis represents the river outflow of each sub basin is shown in red, in 10^4 m^3/s. **D:** the wavelet analysis of the temperature of box MI. The colours indicate the spectral power of the frequencies through time in dB, yellow represents high power and blue low power. Wavelet analysis is a convenient tool to determine the periodicities of this time domain signal. Peaks and notches are found during the non-linear regime, typically in the range of 100-1000 years, much faster than the forcing.

The S1 run, shown in figure 5.4, shows very similar behaviour to the S5 run. With five times the present Nile outflow during the precession minimum, our model reaches a stagnation of deep water formation and convection in the marginal boxes and a reduction in intermediate convection in the open basin, i.e. the regime C in Figure 5.3. In contrast to the S5 model results, the density driven intermediate water exchange with the Atlantic box does not reverse and the intermediate convection never fully stops. Instead, the model directly transitions from regime C to regime E, although with a slower onset of convection. Otherwise the behaviour of the model is the same as in the S5 run.

5.4 Discussion and conclusion

The precessional forcing of the freshwater budget can cause abrupt changes in the circulation. The model shows how, in response to this, the different (parts of) basins relax towards a new equilibrium state with a time scale $\tau \sim V/F$, with the volume V and through flow F. Although precession is a relatively slow process with a period of 20 kyr, a change in circulation can introduce much faster variability in the order of $\tau \sim 0.1 - 1$ kyr. For example, for the marginal intermediate box, with a volume of $2.25 \cdot 10^{14}$ m^3 and a typical flux magnitude of $2 \cdot 10^5$ m^3/s, we find a time scale of ~ 70 yrs. When the magnitude of the fluxes increases, the time scale decreases. For example, towards the end of the “sapropel” interval the fluxes slow down and as a consequence we see the peaks and notches shift towards longer periods in the wavelet transform (Figure 5.2D). Note that frequencies of the peaks and notches observed in Figure 5.2D are indeed in the same order of magnitude as the time scales found using the formula above. When the equilibrium state of a set of coupled boxes changes, those boxes will only reach their equilibrium when the box with the longest time scale has done so. The boxes with shorter time scales will initially approach their equilibrium state relatively fast (following their own time scale), until they are in dynamic equilibrium with a box with a longer time scale. From that point onwards the fast box will approach the equilibrium with the time scale of the slower box. Consequently, we expect to find the time scales related to slower boxes in the signals of faster boxes, given that they are coupled. The wavelet analysis of the intermediate water temperature (Figure 5.2) indeed also shows periodicities that are in the order of 800 yrs, which, using the formula above, is the time scale of the open deep water box in the relevant interval.

Given the importance of volume for the behaviour here emphasized, to what extent are our findings dependent on the representation with boxes of fixed dimensions? Note that the two sets of dynamic boxes in the model (the open basin and the marginal basin) represent basins in the Mediterranean Sea. Since the volume of these basins is constant on orbital time scales, this division is justified. The potential absence of, for example, a separate open intermediate water mass during part of the precession cycle, e.g. the linear interval in Figure 5.2, is realistically captured by convection in the model, which effectively homogenises layers. At present, the surface and intermediate water are also mixed during winter (Schroeder et al., 2012). When, during the remainder of the cycle, the interfaces between the water masses were fixed, but at different depth than here assumed, or varied slowly around an average depth, we expect our time scales to still be in the correct order of magnitude. The same is likely true when, in reality, different water masses existed side by side at the same depth. We therefore conclude that the assumption of constant box volumes is valid. While we show a single model result to highlight the non linear response, this behaviour generally occurs when the freshwater budgets briefly become positive. We therefore conclude that the model results are robust.

We compare our results to XRF data of sapropel S5 ($128-121$ *kyr*) in several sediment cores: 64PE406-E1 and ODP967 (Rodríguez-Sanz et al., 2017b) in the Levantine basin and LC21 (Grant et al., 2016) in the Aegean Sea (Figure 5.5). Barium (Ba) and the Barium/Titanium (Ba/Ti) ratio are proxies for productivity (e.g. Bishop, 1988; Dymond et al., 1992). The Ba/Ti records of S5 in core 64PE406-E1 and ODP967 are similar. They both show a gradual increase starting at 128 *kyr* and a sudden termination at 122 *kyr*. The Ba record of LC21 shows a large peak at the start of the sapropel, the difference compared to 64PE406-E1 and ODP967 may be explained by its location; it seems likely that productivity close to the Nile (64PE406-E1 and ODP967) was not the same as in the Aegean Sea (LC21).

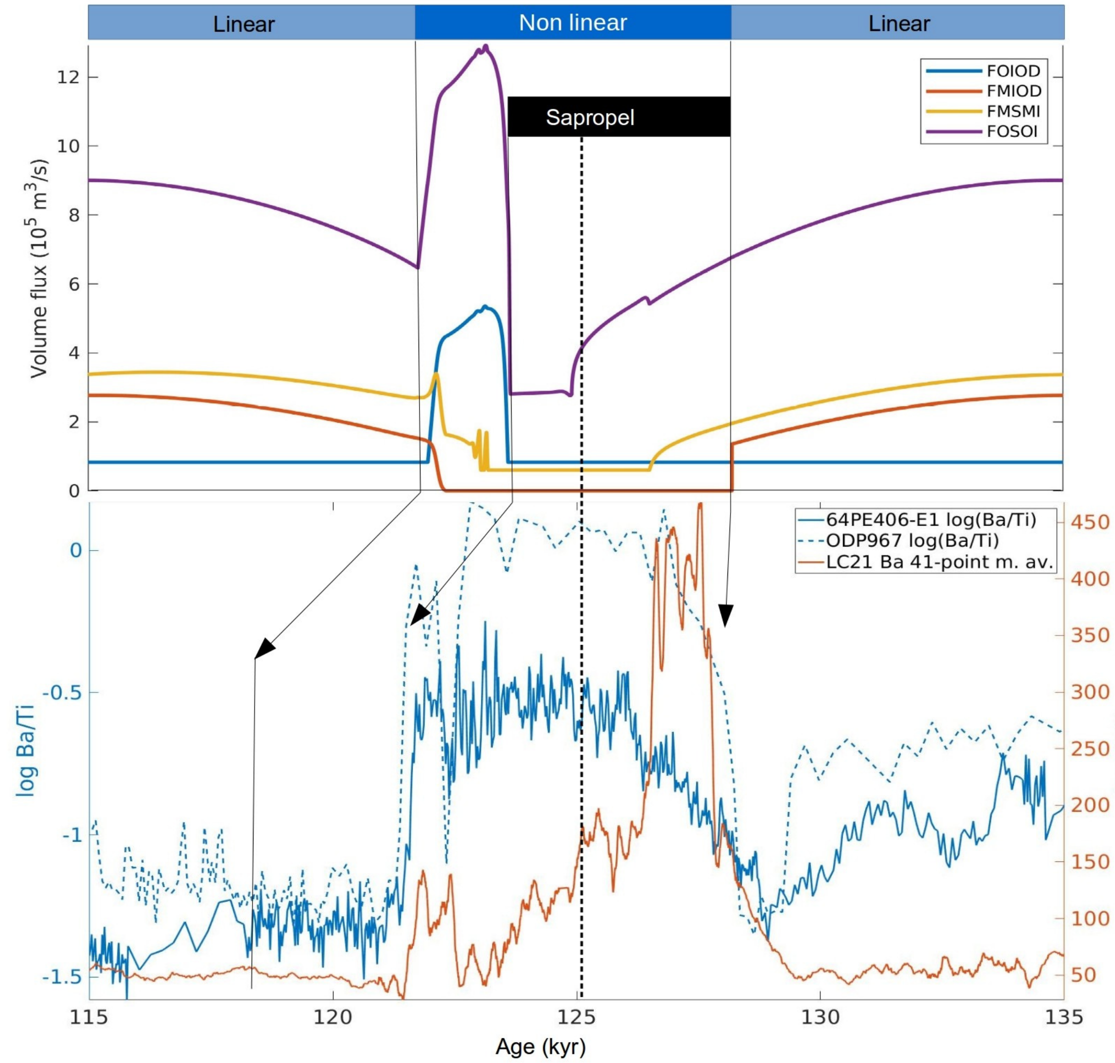

Figure 5.5 The vertical fluxes of the model run (top panel) are compared with Ba/Ti XRF data from core 64PE406-E1 and ODP967, as well as Ba data from core LC21 (bottom panel). The time axis comprises a single precession cycle and runs from right to left. The vertical dashed line at 125 ka represents the approximate sapropel midpoint in the core data and the maximum of the river outflow and minimum net evaporation in the model. The arrows indicate transitions found in both the core data and the model run.

These proxies show high-frequency variability in the sapropel interval in cores 64PE406-E1 and LC21 (Figure 5.5). Proxies for bottom water anoxia (Mo/Ti Ziegler et al., 2008) and marine organic carbon (Br/Ti, e.g. Scott and Lyons, 2012; Tribovillard et al., 2006) in core 64PE406-E1 show very similar high-frequency variability (Dirksen et al., 2019). The proxies of these properties correlate with each other on even the shortest time scales (see the Monte-Carlo analysis in Dirksen et al., 2019). This implies that the Barium (productivity) variability also correlates with anoxia. The increased productivity is likely caused by increased Nile outflow, since the river water provides nutrients. The extra fresh water influx is also hypothesized to cause a stratified water column (Rossignol-Strick, 1985; Rohling et al., 2015). In the model, stratification occurs when the vertical fluxes (Figure 5.5) are minimal, as a result of increased river outflow and decreased evaporation. The vertical deep water fluxes in the model, FMIOD and FOIOD, are of particular interest, since the sediment cores are taken in deep parts of the basin and the sapropels in these cores therefore formed in the deep water.

The model predicts sudden changes in circulation, which causes the water properties to decay towards the new equilibrium. Such transitions would likely also affect productivity, since different water masses have different properties and nutrient concentrations. A sudden change in the equilibrium state is therefore expected to cause a similar decay towards a new equilibrium state in the proxies. Our model predicts such sudden changes and may therefore offer an alternative explanation for variability hitherto ascribed to high-frequency forcing (Dirksen et al., 2019).

Sapropel S5 is interrupted in core ODP967 (Rodríguez-Sanz et al., 2017b) at 122 *kyr*, just before the end of the sapropel. The interruption coincides with an increase in productivity at LC21. This could be explained by convection or deep water formation in the Levantine basin (e.g. the regime in panel E in Figure 5.3), supplying nutrients to the surface that accumulated during the stratified phase. The model does not predict an interruption, this is likely the result of the simplified forcing. Note that Dirksen et al. (2019) did not find an interruption in S5 in core 64PE406-E1. In our model we find that the stratification, when all downward fluxes are minimal, becomes unstable towards the end of the sapropel, at 11.8 *kyr* in Figure 5.2A, corresponding to the transition from panel D to E in Figure 5.3. After the interruption in the cores, sapropel formation briefly resumes, followed by a sudden termination at all core sites. This could either imply a sudden transition to the present day circulation, or a transition to a state where deep convection occurs in the Levantine basin and one or both marginal basins similar to regimes E, F or G in Figure 5.3. The latter implies that while the sapropel is terminated, the circulation will still have to change to reach the linear state, which would introduce multi centennial scale variability in the interval directly after the sapropel. This would correspond with the non-linear interval directly after the sapropel in Figure 5.5 between of 11 to 13 *kyr* in Figure 5.2A and panels E,F and G in Figure 5.3. Here the model indeed shows a different circulation than the present state: there is strong convection in all boxes and no deep water formation from the margins. The corresponding interval in the cores is bioturbated (see Figure 4A in Dirksen et al., 2019), this bioturbation effectively acts as a low pass filter, meaning that the relevant variability may still be detectable. Furthermore, Dirksen et al. (2019) has shown that burn down did not occur (since there was no Mn/Ti peak after the sapropel) and as indicated by the results shown in Dirksen and Meijer (2020), directly resuming the normal circulation would likely not give a fast enough transition to prevent burn down. Note that the model forcing is a sine wave, while the actual monsoon intensity deviates. Nevertheless, the start of the the sapropel is correctly predicted, while the sapropel duration is underestimated, indicating that the actual forcing is not harmonic.

Next we compare frequency components and trends in the model with those found in core 64PE406-E1. We find that both show slowly varying frequencies in the order of 100-1000 years. The peaks in the wavelet transform of the core data in Dirksen et al. (2019) show an acceleration, i.e. longer periods, towards the end of the sapropel, similar to what we find in the model (Figure 5.2D). In Dirksen et al. (2019) the modulation of the high-frequency components was interpreted as a the sedimentation rate variability. Here we propose an alternative mechanism. The time scale τ of this variability depends on the magnitude of the fluxes, as discussed above. Since the Nile outflow is expected to affect the magnitude of the fluxes, it should also modulate the high-frequency components. The model predicts that the main frequencies vary in time. Note that this hypothesis and the mechanism presented in Dirksen et al. (2019) are not mutually exclusive. The Nile flood record is known to correlate with Holocene solar variability (Ruzmaikin et al., 2006), so it seems likely that the discharge also showed this variability during the deposition of sapropel S5. In that case the Nile outflow would modulate the flux magnitudes directly, which would in turn modulate the time scale of any transitions. A modulation of the sedimentation rate would have had the same effect on the record, so it is possible that both of these mechanisms occurred simultaneously. With a sine wave forcing, our model captures the timing, termination and a significant part of the high frequency variability reasonably well. However, the characteristic laminations found in the sapropel in sediment cores are not reproduced by the model.

S1 has been studied extensively in sediment cores and with models. The rapid termination of the stratified state in our model due to deep convection in both presented runs is in agreement with the basin-wide, deep-water renewal found at the end of S1 formation by Wu et al. (2019). The formation of sapropel S1 may have been influenced by changes in sea level variations Cornuault et al. (2018). However, the ventilation in our model is not very sensitive to realistic changes in strait efficiency, i.e. the primary effect of sea level change. Furthermore, Vadsaria et al. (2019) indicate that the observed behaviour can largely be explained by monsoon variability.

We conclude that high-frequency variability in the Mediterranean Sea may not only result from high-frequency forcing, but also from non-linear internal variability. Specifically, abrupt changes in circulation cause the various parts of the basin to relax towards a new equilibrium state, the time scale of this relaxation depends on the volume of the water mass and the magnitude of the circulation. The time scales found in our model are in agreement with those found in sediment cores. We find that our model captures the overall behaviour of both S1 and S5.

5.5 Data statement

The annotated model code is available at `https://doi.org/10.17605/OSF.IO/PQ5MY`. The $\{*\}.m$ files will run in Matlab, but can be viewed in any text editor.

5.6 Appendix A

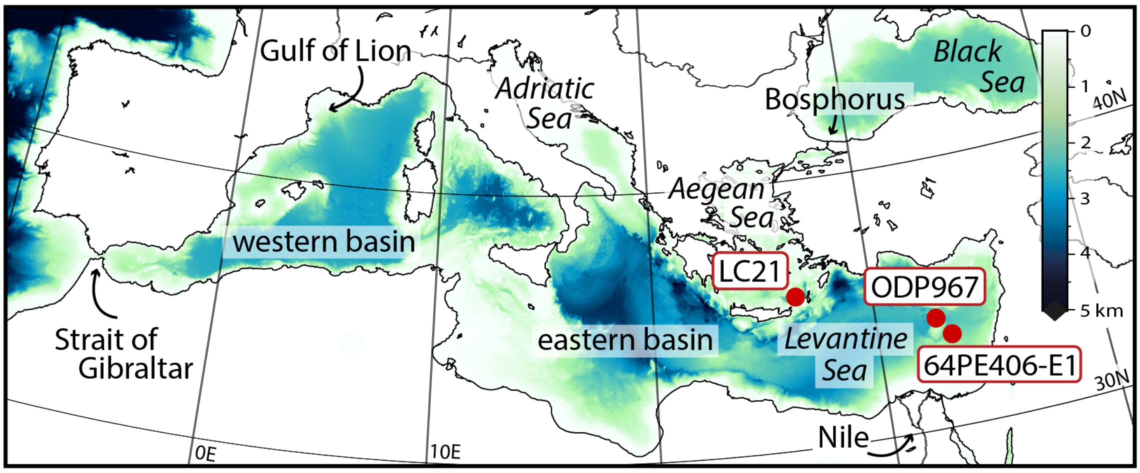

Figure 5.6 A map of the Mediterranean Sea. The colour map indicates water depth in kilometres. The dots indicates the location of cores LC21, ODP967 and 64PE406-E1.

6 Synthesis and Outlook

6.1 General

Past oceanographic conditions are reconstructed using sediment cores. In Chapter 2 advanced analysis techniques, such as XRF core scanning, reveal a fine, complex structure of layers. In subsequent chapters a transient box model is used to interpret the data and study the fundamental mechanisms that control sapropel formation. These models for the Mediterranean Sea and the Black Sea indicate that sapropel formation is an inherently transient process: sapropels form when the basin transitions to a different circulation state. This fundamental insight would have been impossible to achieve with models that focus separately on the states with and without sapropel deposition ("time slice experiments").

6.2 Tipping points?

The box model consists of differential equations that describe the interaction of a small number of boxes. Each box represents a volume of water (or atmosphere) with uniform properties such as temperature. The model is forced by a very slow process: orbital precession (20 kyr). Nevertheless, surprisingly abrupt transitions, with time constants of less than 100 years, to new equilibrium states are found. The most prominent example of a transition in the Mediterranean Sea occurs in response to a change from net evaporation to net freshwater input, at which time a sapropel forms. Importantly, this does not imply that the basin has to complete a transition from anti-estuarine to estuarine circulation. Starting from a state of anti-estuarine circulation, a period with a positive freshwater budget may cause the circulation to stop, but the circulation only becomes estuarine once the intermediate and deep water density has decreased sufficiently. While the vertical circulation has stopped, however, there is little exchange of properties between the surface and underlying water masses, meaning that the intermediate and deep water gain buoyancy very slowly. Consequently, this state without vertical circulation could persist for several thousand years. If, in the meantime, the freshwater budget becomes negative again (net evaporation), the full transition will not be completed and the anti-estuarine circulation resumes. The finding of rapid transitions naturally leads one to wonder whether the model is predicting tipping points. When considering tipping points in relation to sapropel formation, one would intuitively first look at the start of sapropel formation: a sudden stop of deep water formation and relatively fast onset

---

Picture left: The piston core used in this thesis, while being collected by the RV Pelagia during cruise 64PE406-E on the Eastern Mediterranean Sea, near Cyprus.

of bottom water anoxia. However, my model suggests that the onset of sapropel formation is not a tipping point at all: while the deep water formation suddenly stops, it is not irreversible and otherwise a relatively gradual change. In some cases, specifically S5, there is a very sudden termination of the sapropel. My model suggests that this is caused by deep convection, which results in an instantaneous transition to a completely different circulation. In contrast to the onset of the sapropel, this transition is not reversible. We therefore conclude that the termination of S5 is most likely a true tipping point.

6.3 Combining insights

In Chapter 5 I find that the abrupt termination of sapropel S5 is likely the result of deep convection. However, that does not explain the absence of burn down, signified by the lack of a Mn/Ti peak in Figure 2.2 in Chapter 2. The nutrient model presented in Chapter 4 provides a potential mechanism: during the sapropel state, the water column is stratified and nutrients accumulate in the deep water. The convection that terminates the sapropel brings these nutrients to the surface, where they cause an increase in productivity. Potentially, the breakdown of this organic matter kept the oxygen concentration at the top of the sediment sufficiently low to prevent significant burn-down.

6.4 Forcing the model with a proxy record of the forcing?

So far, I have modelled the forcing with a sine wave with a period equal to the orbital precession. Such a harmonic forcing model captures most of the prominent features found in cores. Sediment-core data, from which the actual forcing can be derived using a proxy, is available. Figure 6.1 compares the harmonic forcing model to the actual data of core 64PE406-E1 (Dirksen et al., 2019). While the harmonic forcing captures most of the variability, there is a difference with the actual forcing. The actual core data can also be used to force the current model. Such complex forcing is more appropriate for reconstructing past oceanographic variability, but obfuscates the fundamental processes.

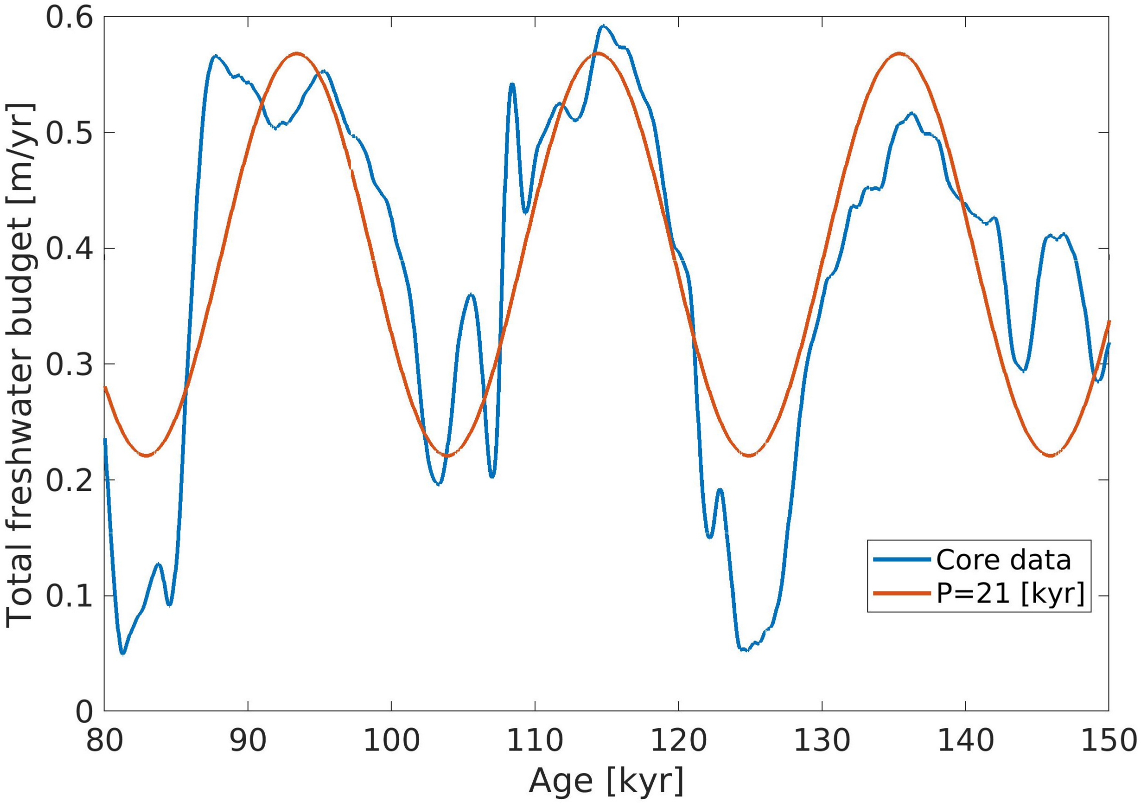

Figure 6.1 The solid blue line represents the experimental core data, scaled to represent the total freshwater budget, from which all forcing is derived. The red line is a least square fit of a sine, with a period of 21 *kyr*.

6.5 Other basins

The current model has a number of known limitations, which prevent the direct application to other basins with different strait configurations, such as the Japan Sea (East Sea) and the Red Sea. However, the description of these basins is well within the framework of this model—by adaption of the strait equations and the number of the boxes, these basins can be described. Moreover, sapropels are also found in the Japan Sea, where they occur on millennial time scales instead. Furthermore, heat input from the ocean floor seems to be an important driver, indicating that different mechanisms may be important in this basin. It is likely that a low-complexity box model also applies. The Miocene Sorbas basin of southeastern Spain, although not described in this thesis, is likely to be captured by the current model, be it with different parameters. Sapropels are also found in this basin. Since it is a much smaller basin, a relatively small river input could change the sign of the freshwater budget and therefore stop the circulation, causing sapropel formation, thereby following the same mechanism as the rest of the Mediterranean Sea on a much smaller scale. In the Mediterranean Sea, true sapropels are not found in the western basin. The models presented in this thesis do not have a separate eastern and western basin. An extended version of the model, essentially duplicating the intermediate water model of Chapter 5, could be used to study the implications of such a second order system. However, we do know that there is no large source of freshwater in the Western Mediterranean Sea, making it unlikely that it ever approached an estuarine circulation. Consequently, the non-linear mechanism described in this thesis should not occur in the western basin and its ventilation should thus not be disrupted by precessional variability, preventing sapropel formation. Nevertheless, it would be interesting to include an additional set of boxes, representing the this basin. Such a model could be used to study the interaction of the eastern and western basin, since this could affect sapropel formation in the eastern basin.

Acknowledgements

This thesis would not have been possible without the help and input of many people. First and foremost, I would like to thank my supervisor, Paul Meijer and promotor Wout Krijgsman.

The pleasant coperation with the colleagues of the tectonophysics group and members of the deparmant of Earth Sciences is greatly appreciated. I would also like to thank Carloline Slomp, Frits Hilgen, Lukas Van Der Wiel, Nikolai Nijholt and Dirk Simon. In particular, I would like to thank Ronja Ebner for the many fruitfull discussion and all the fun, yet important, coffeebreaks.

During my internship at the NIOZ, I was inspired by a very enthousiastic and skilled research group, who encouraged me to pursuit a PhD in paleoceanography. I would like to thank the OCS group for their effort and pleasant cooperation and in particular Gert-Jan Reichart, Rick Hennekam, Esmee Geerken. The trip on the research vessel Pelagia has made a lasting impression, many thanks to the crew of cruise 64PE406! All the spectacular photos in this thesis originate from this trip.

Working with Suzan Pit and Bart Stam during their Master gave me valuable new perspectives and greatly contributed to this thesis. Many thanks!

The last chapters of this thesis were written during the covid-19 pandemic. Like many other, I was forced to work in isolation, at home. I would not have been able to complete this thesis without the moral support of my friends. In particular I would like to thank Melissa Vleugel, Barbara Delgado and my bandmates in Gula: Ilja Fase, Jan Blijenberg and Aad Oliehoek.

References

Abu-Zied, R. H., E. J. Rohling, F. J. Jorissen, C. Fontanier, J. S. Casford and S. Cooke (2008), Benthic foraminiferal response to changes in bottom-water oxygenation and organic carbon flux in the eastern mediterranean during lgm to recent times. Marine Micropaleontology 67, 46–68.

Adloff, F., U. Mikolajewicz, M. Kučera, R. Grimm, E. Maier-Reimer, G. Schmiedl and K. C. Emeis (2011), Upper ocean climate of the eastern mediterranean sea during the holocene insolation maximum - a model study. Climate of the Past 7, 1103–1122.

Altabet, M. A., M. J. Higginson and D. W. Murray (2002), The effect of millennial-scale changes in arabian sea denitrification on atmospheric co 2. Nature 415, 159–162.

Altieri, A. H. and K. B. Gedan (2015), Climate change and dead zones. Global Change Biology 21, 1395–1406.

Amies, J., E. J. Rohling and K. M. Grant (2019), Quantification of african monsoon runoff during last interglacial sapropel s5. Paleoceanography and Paleoclimatology , 1–30.

Anklin, M., J.-M. Barnola, J. Beer, T. Blunier, J. Chappellaz, H. Clausen, D. Dahl-Jensen, W. Dansgaard, M. De Angelis, R. Delmas et al. (1993), Climate instability during the last interglacial period recorded in the grip ice core. Nature 364, 203–207.

Arthur, M. A. and W. E. Dean (1998), Organic-matter production and preservation and evolution of anoxia in the holocene black sea 13, 395–411.

Ashkenazy, Y., P. H. Stone and P. Malanotte-Rizzoli (2012), Box modeling of the eastern mediterranean sea. Physica A: Statistical Mechanics and its Applications 391, 1519–1531. URL `http://dx.doi.org/10.1016/j.physa.2011.08.026`.

Bale, N. J., R. Hennekam, E. C. Hopmans, D. Dorhout, G. jan Reichart, M. V. D. Meer, T. A. Villareal, J. S. S. Damsté and S. Schouten (2019), Biomarker evidence for nitrogen-fixing cyanobacterial blooms in a brackish surface layer in the nile river plume during sapropel deposition XX, 1–5.

Barker, S., G. Knorr, R. L. Edwards, F. Parrenin, A. E. Putnam, L. C. Skinner, E. Wolff and M. Ziegler (2011), 800,000 years of abrupt climate variability. science 334, 347–351.

Bensi, M., V. Cardin, A. Rubino, G. Notarstefano and P. M. Poulain (2013), Effects of winter convection on the deep layer of the southern adriatic sea in 2012. Journal of Geophysical Research: Oceans 118, 6064–6075.

Bianchi, D., M. Zavatarelli, N. Pinardi, R. Capozzi, L. Capotondi, C. Corselli and S. Masina (2006), Simulations of ecosystem response during the sapropel s1 deposition event. Palaeogeography, Palaeoclimatology, Palaeoecology 235, 265–287.

Bibby, T., J. Putkonen, D. Morgan, G. Balco and D. L. Shuster (2016), Million year old ice found under meter thick debris layer in antarctica. Geophysical Research Letters 43, 6995–7001. URL `http://doi.wiley.com/10.1002/2016GL069889`.

Bigg, G. R. (1994), An ocean general circulation model view of the glacial mediterranean thermohaline circulation. Paleoceanography 9, 705–722.

Bishop, J. K. (1988), The barite-opal-organic carbon association in oceanic particulate matter. Nature 332, 341–343.

Blaga, C. I., G.-J. Reichart, A. F. Lotter, F. S. Anselmetti and J. S. Sinninghe Damsté (2013), A tex86 lake record suggests simultaneous shifts in temperature in central europe and greenland during the last deglaciation. Geophysical Research Letters 40, 948–953.

Bogdanova, A. K. (1963), The distribution of mediterranean waters in the black sea. Deep-Sea Research and Oceanographic Abstracts 10, 665–672.

Bond, G., W. Broecker, S. Johnsen, J. McManus, L. Labeyrie, J. Jouzel and G. Bonani (1993), Correlations between climate records from north atlantic sediments and greenland ice. Nature 365, 143–147.

Bond, G., W. Showers, M. Cheseby, R. Lotti, P. Almasi, P. DeMenocal, P. Priore, H. Cullen, I. Hajdas and G. Bonani (1997), A pervasive millennial-scale cycle in north atlantic holocene and glacial climates. science 278, 1257–1266.

Boudreau, B. P., S. Calvert and M. Kienast (2022), Memory Effects in Salinity Profiles From Black Sea Sediments. Paleoceanography and Paleoclimatology 37, 1–14.

Broccoli, A. J., K. A. Dahl and R. J. Stouffer (2006), Response of the itcz to northern hemisphere cooling. Geophysical Research Letters 33. `https://agupubs.onlinelibrary.wiley.com/doi/pdf/10.1029/2005GL024546`, URL `https://agupubs.onlinelibrary.wiley.com/doi/abs/10.1029/2005GL024546`.

Bryden, H. L. and T. H. Kinder (1991), Steady two-layer exchange through the strait of gibraltar. Deep Sea Research Part A. Oceanographic Research Papers 38, S445–S463.

Calvert, S. E., B. Nielsen and M. R. Fontugne (1992), Evidence from nitrogen isotope ratios for enhanced productivity during formation of eastern mediterranean sapropels. Nature 359, 223–225.

Cappellen, P. V. and E. D. Ingall (1994), Benthic phosphorus regeneration, net primary production and ocean anoxia. Paleoceanography 9, 677–692.

Capron, E., A. Govin, R. Feng, B. L. Otto-Bliesner and E. Wolff (2017), Critical evaluation of climate syntheses to benchmark cmip6/pmip4 127 ka last interglacial simulations in the high-latitude regions. Quaternary Science Reviews 168, 137–150.

Channell, J. E. T., D. A. Hodell, B. S. Singer and C. Xuan (2010), Reconciling astrochronological and 40 ar/ 39 ar ages for the matuyama-brunhes boundary and late matuyama chron. Geochemistry, Geophysics, Geosystems 11, n/a–n/a.

Command, N. O. (1987), Us navy climatic study of the mediterranean sea. Naval Oceanography Command Detachment, Asheville, North Carolina (342 pp.) .

Cook, E. R., R. D. D'Arrigo and M. E. Mann (2002), A well-verified, multiproxy reconstruction of the winter north atlantic oscillation index since a.d. 1400. Journal of Climate 15, 1754–1764.

Cornuault, M., K. Tachikawa, L. Vidal, A. Guihou, G. Siani, P. Deschamps, F. Bassinot and M. Revel (2018), Circulation changes in the eastern mediterranean sea over the past 23,000 years inferred from authigenic nd isotopic ratios. Paleoceanography and Paleoclimatology 33, 264–280.

Cramp, A. and G. O'Sullivan (1999), Neogene sapropels in the mediterranean: A review. Marine Geology 153, 11–28.

Dahl-Jensen, D., M. Albert, A. Aldahan, N. Azuma, D. Balslev-Clausen, M. Baumgartner, A.-M. Berggren, M. Bigler, T. Binder, T. Blunier et al. (2013), Eemian interglacial reconstructed from a greenland folded ice core. Nature 493, 489–494.

Dansgaard, W., S. J. Johnsen, H. B. Clausen, D. Dahl-Jensen, N. Gundestrup, C. Hammer, C. Hvidberg, J. Steffensen, A. Sveinbjörnsdottir, J. Jouzel et al. (1993), Evidence for general instability of past climate from a 250-kyr ice-core record. nature 364, 218–220.

De Lange, G. and H. Ten Haven (1983), Recent sapropel formation in the eastern mediterranean. Nature 305, 797.

Diaz, R. J. and R. Rosenberg (2008), Spreading dead zones and consequences for marine ecosystems. Science 321, 926–929.

Dirksen, J., S. Pit, C. Slomp and P. Meijer (to be published), Transient-model analysis of sapropel formation in the Holocene Black Sea .

Dirksen, J. P. and P. Meijer (2020), The mechanism of sapropel formation in the mediterranean sea: insight from long-duration box model experiments. Climate of the Past 16, 933–952.

Dirksen, J. P., R. Hennekam, E. Geerken and G. J. Reichart (2019), A novel approach using time-depth distortions to assess multicentennial variability in deep-sea oxygen deficiency in the eastern mediterranean sea during sapropel s5. Paleoceanography and Paleoclimatology 34, 774–786.

Dykoski, C. A., R. L. Edwards, H. Cheng, D. Yuan, Y. Cai, M. Zhang, Y. Lin, J. Qing, Z. An and J. Revenaugh (2005), A high-resolution, absolute-dated holocene and deglacial asian monsoon record from dongge cave, china. Earth and Planetary Science Letters 233, 71–86.

Dymond, J., E. Suess and M. Lyle (1992), Barium in deep-sea sediment: A geochemical proxy for paleoproductivity. Paleoceanography 7, 163–181.

Eckert, S., H. J. Brumsack, S. Severmann, B. Schnetger, C. März and H. Fröllje (2013), Establishment of euxinic conditions in the holocene black sea. Geology 41, 431–434.

Egger, M., P. Kraal, T. Jilbert, F. Sulu-Gambari, C. J. Sapart, T. Röckmann and C. P. Slomp (2016), Anaerobic oxidation of methane alters sediment records of sulfur, iron and phosphorus in the black sea. Biogeosciences 13, 5333–5355.

Finnigan, T. D., K. B. Winters and G. N. Ivey (2001), Response characteristics of a buoyancy-driven sea. Journal of Physical Oceanography 31, 2721–2736.

Friedrich, J., C. Dinkel, G. Friedl, N. Pimenov, J. Wijsman, M. T. Gomoiu, A. Cociasu, L. Popa and B. Wehrli (2002), Benthic nutrient cycling and diagenetic pathways in the north-western black sea. Estuarine, Coastal and Shelf Science 54, 369–383.

Gertman, I., N. Pinardi, Y. Popov and A. Hecht (2006), Aegean sea water masses during the early stages of the eastern mediterranean climatic transient (1988-90). Journal of Physical Oceanography 36, 1841–1859.

Gertmann, I., I. Ovchinnikov and Y. Popv (1994), Deep convection in the eastern basin of the mediterranean sea. Oceanology 34, 19–25.

Giosan, L., J. P. Donnelly, S. Constantinescu, F. Filip, I. Ovejanu, A. Vespremeanu-Stroe, E. Vespremeanu and G. A. T. Duller (2006), Young danube delta documents stable black sea level since the middle holocene: Morphodynamic, paleogeographic, and archaeological implications. Geology 34, 757–760.

Grant, K. M., E. J. Rohling, M. Bar-Matthews, A. Ayalon, M. Medina-Elizalde, C. B. Ramsey, C. Satow and A. P. Roberts (2012), Rapid coupling between ice volume and polar temperature over the past 50,000 years. Nature 491, 744–747. URL `http://dx.doi.org/10.1038/nature11593`.

Grant, K. M., R. Grimm, U. Mikolajewicz, G. Marino, M. Ziegler and E. J. Rohling (2016), The timing of mediterranean sapropel deposition relative to insolation, sea-level and african monsoon changes. Quaternary Science Reviews 140, 125–141. URL `http://dx.doi.org/10.1016/j.quascirev.2016.03.026`.

Grimm, R., E. Maier-Reimer, U. Mikolajewicz, G. Schmiedl, K. Müller-Navarra, F. Adloff, K. M. Grant, M. Ziegler, L. J. Lourens and K. C. Emeis (2015), Late glacial initiation of holocene eastern mediterranean sapropel formation. Nature Communications 6.

Grootes, P. M., M. Stuiver, J. White, S. Johnsen and J. Jouzel (1993), Comparison of oxygen isotope records from the gisp2 and grip greenland ice cores. Nature 366, 552–554.

Grossmann, A. and J. Morlet (1984), Decomposition of hardy functions into square integrable wavelets of constant shape. SIAM journal on mathematical analysis 15, 723–736.

Haug, G. H., K. A. Hughen, D. M. Sigman, L. C. Peterson and U. Röhl (2001), Southward migration of the intertropical convergence zone through the holocene. Science 293, 1304–1308.

Hayes, D. R., K. Schroeder, P.-M. Poulain, P. Testor, L. Mortier, A. Bosse and X. du Madron (2019), 18 review of the circulation and characteristics of intermediate water masses of the mediterranean: Implications for cold-water coral habitats 9, 195–211.

Heinrich, H. (1988), Origin and consequences of cyclic ice rafting in the northeast atlantic ocean during the past 130,000 years. Quaternary research 29, 142–152.

Hennekam, R. (2015), High-frequency climate variability in the late Quaternary eastern Mediterranean Associations of Nile discharge and basin overturning circulation dynamics.

Hennekam, R. and G. de Lange (2012), X-ray fluorescence core scanning of wet marine sediments: methods to improve quality and reproducibility of high-resolution paleoenvironmental records. Limnology and Oceanography: Methods 10, 991–1003.

Hennekam, R., T. Jilbert, B. Schnetger and G. J. De Lange (2014), Solar forcing of nile discharge and sapropel s1 formation in the early to middle holocene eastern mediterranean. Paleoceanography 29, 343–356.

Herbert, T. (1994), Reading orbital signals distorted by sedimentation: models and examples. Orbital Forcing and Cyclic Sequences , 483–507.

Herbert, T. D., G. Ng and L. C. Peterson (2015), Evolution of mediterranean sea surface temperatures 3.5–1.5 ma: regional and hemispheric influences. Earth and Planetary Science Letters 409, 307–318.

Herrmann, M., C. Estournel, M. Déqué, P. Marsaleix, F. Sevault and S. Somot (2008), Dense water formation in the gulf of lions shelf: Impact of atmospheric interannual variability and climate change. Continental Shelf Research 28, 2092–2112.

Higgs, N., J. Thomson, T. Wilson and I. Croudace (1994), Modification and complete removal of eastern mediterranean sapropels by postdepositional oxidation. Geology 22, 423–426.

Hilgen, F. J. (1991), Extension of the astronomically calibrated (polarity) time scale to the miocene/pliocene boundary. Earth and Planetary Science Letters 107, 349–368.

Hilgen, F. J., W. Krijgsman, C. G. Langereis, L. J. Lourens, A. Santarelli and W. J. Zachariasse (1995), Extending the astronomical (polarity) time scale into the miocene. Earth and Planetary Science Letters 136, 495–510.

Hoffman, J. S., P. U. Clark, A. C. Parnell and F. He (2017), Regional and global sea-surface temperatures during the last interglaciation. Science 355, 276–279.

Incarbona, A., M. Sprovieri, F. Lirer and R. Sprovieri (2011), Surface and deep water conditions in the sicily channel (central mediterranean) at the time of sapropel s5 deposition. Palaeogeography, Palaeoclimatology, Palaeoecology 306, 243–248. URL `http://dx.doi.org/10.1016/j.palaeo.2011.04.030`.

Jilbert, T., G.-J. Reichart, P. Mason and G. J. de Lange (2010), Short-time-scale variability in ventilation and export productivity during the formation of mediterranean sapropel s1. Paleoceanography 25.

Jordà, G., K. V. Schuckmann, S. A. Josey, G. Caniaux, J. García-Lafuente, S. Sammartino, E. Özsoy, J. Polcher, G. Notarstefano, P. M. Poulain, F. Adloff, J. Salat, C. Naranjo, K. Schroeder, J. Chiggiato, G. Sannino and D. Macías (2017), The mediterranean sea heat and mass budgets: Estimates, uncertainties and perspectives. Progress in Oceanography 156, 174–208.

Jorissen, F. J. (1999), Benthic foraminiferal successions across late quaternary mediterranean sapropels. Marine Geology 153, 91–101.

Karaca, M., A. Wirth and M. Ghil (1999), A box model for the paleoceanography of the black sea. Geophys. Res. Letters 26, 497–500.

Kemp, A. E., R. B. Pearce, I. Koizumi, J. Pike and S. J. Rance (1999), The role of mat-forming diatoms in the formation of mediterranean sapropels. Nature 398, 57.

Kirby, J. F. and C. J. Swain (2013), Power spectral estimates using two-dimensional morlet-fan wavelets with emphasis on the long wavelengths: Jackknife errors, bandwidth resolution and orthogonality properties. Geophysical Journal International 194, 78–99.

Kislov, A. (2018), On the interpretation of century–millennium-scale variations of the black sea level during the first quarter of the holocene. Quaternary International 465, 99–104.

Kondrashov, D., Y. Feliks and M. Ghil (2005), Oscillatory modes of extended nile river records (a.d. 622-1922). Geophysical Research Letters 32, 1–4.

Kosarev, A. N., A. G. Kostianoy and T. A. Shiganova (2008), The Sea of Azov. Berlin, Heidelberg: Springer Berlin Heidelberg, 63–89. URL `https://doi.org/10.1007/698_5_091`.

Krijgsman, W., F. J. Hilgen, I. Raffi, F. J. Sierro and D. S. Wilson (1999), Chronology, causes and progression of the messinian salinity crisis. Nature 400, 652–655.

Krom, M. D., J. D. Stanley, R. A. Cliff and J. C. Woodward (2002), Nile river sediment fluctuations over the past 7000 yr and their key role in sapropel development. Geology 30, 71–74.

Kubryakov, A., G. Korotaev, V. Dorofeev, Y. B. Ratner, A. Palazov, N. Valchev, V. Malciu, R. Mateescu and T. Oguz (2012), Black sea coastal forecasting system. Ocean Science 8, 183–196.

LAMBECK, K., D. SIVAN and A. PURCELL (2007), Timing of the last mediterranean sea black sea connection from isostatic models and regional sea-level data. The Black Sea Flood Question: Changes in Coastline, Climate, and Human Settlement , 797–808.

LANCELOT, C., J. STANEVA, D. VAN EECKHOUT, J.-M. BECKERS and E. STANEV (2002), Modelling the danube-influenced north-western continental shelf of the black sea. ii: Ecosystem response to changes in nutrient delivery by the danube river after its damming in 1972. Estuarine, Coastal and Shelf Science 54, 473–499. URL `https://www.sciencedirect.com/science/article/pii/S0272771400906590`.

LANE-SERFF, G. F., E. I. ROHLING, H. L. BRYDEN and H. CHARNOCK (1997), Postglacial connection of the black sea to the mediterranean and its relation to the timing of sapropel formation. Paleoceanography 12, 169–174.

LANGE, G. J. D., J. THOMSON, A. REITZ, C. P. SLOMP, M. S. PRINCIPATO, E. ERBA and C. CORSELLI (2008), Synchronous basin-wide formation and redox-controlled preservation of a mediterranean sapropel. Nature Geoscience 1, 606–610.

LASKAR, J. (1988), Secular evolution of the solar system over 10 million years. Astronomy and Astrophysics 198, 341–362.

LLAVE, E., J. SCHÖNFELD, F. J. HERNÁNDEZ-MOLINA, T. MULDER, L. SOMOZA, V. D. D. RÍO and I. SÁNCHEZ-ALMAZO (2006), High-resolution stratigraphy of the mediterranean outflow contourite system in the gulf of cadiz during the late pleistocene: The impact of heinrich events. Marine Geology 227, 241–262.

LOURENS, L. J., A. ANTONARAKOU, F. J. HILGEN, A. A. V. HOOF, C. VERGNAUD-GRAZZINI and W. J. ZACHARIASSE (1996), Evaluation of the plio-pleistocene astronomical timescale. Paleoceanography 11, 391–413.

LOURENS, L. J., R. WEHAUSEN and H. J. BRUMSACK (2001), Geological constraints on tidal dissipation and dynamical ellipticity of the earth over the past three million years. Nature 409, 1029–1033.

LUDWIG, W., E. DUMONT, M. MEYBECK and S. HEUSSNER (2009), River discharges of water and nutrients to the mediterranean and black sea: Major drivers for ecosystem changes during past and future decades? Progress in Oceanography 80, 199–217. URL `http://dx.doi.org/10.1016/j.pocean.2009.02.001`.

MALANOTTE-RIZZOLI, P. (1991), The northern adriatic sea as a prototype of convection and water mass formation on the continental shelf. Elsevier Oceanography Series 57, 229–239.

MARCHITTO, T. M., R. MUSCHELER, J. D. ORTIZ, J. D. CARRIQUIRY and A. VAN GEEN (2010), Dynamical response of the tropical pacific ocean to solar forcing during the early holocene. Science 330, 1378–1381.

MARINO, G., E. J. ROHLING, W. I. C. RIJPSTRA, F. SANGIORGI, S. SCHOUTEN and J. S. S. DAMSTÉ (2007), Aegean sea as driver of hydrographic and ecological changes in the eastern mediterranean. Geology 35, 675–678.

Marshall, J. and F. Schott (1999), Open-ocean convection: Observations, theory, and models. Reviews of Geophysics 37, 1–64.

Marzocchi, A. (2016), Modelling the impact of orbital forcing on late Miocene climate: implications for the Mediterranean Sea and the Messinian Salinity Crisis. Ph.D. thesis, University of Bristol.

Marzocchi, A., D. J. Lunt, R. Flecker, C. D. Bradshaw, A. Farnsworth and F. J. Hilgen (2015), Orbital control on late miocene climate and the north african monsoon: Insight from an ensemble of sub-precessional simulations. Climate of the Past 11, 1271–1295.

Matthiesen, S. and K. Haines (2003), A hydraulic box model study of the mediterranean response to postglacial sea-level rise. Paleoceanography 18.

Meijer, P. (2021), (Paleo)oceanography of semi-enclosed seas with a focus on the Mediterranean region; Insights from basic theory. Earth-Science Reviews 221, 103810. URL `https://doi.org/10.1016/j.earscirev.2021.103810`.

Meijer, P. T. and H. A. Dijkstra (2009), The response of mediterranean thermohaline circulation to climate change: a minimal model. Climate of the Past Discussions 5, 1731–1749. URL `http://www.clim-past-discuss.net/5/1731/2009/`.

Meijer, P. T. and E. Tuenter (2007), The effect of precession-induced changes in the mediterranean freshwater budget on circulation at shallow and intermediate depth. Journal of Marine Systems 68, 349–365.

Mercone, D., J. Thomson, R. H. Abu-Zied, I. W. Croudace and E. J. Rohling (2001), High-resolution geochemical and micropalaeontological profiling of the most recent eastern mediterranean sapropel. Marine Geology 177, 25–44.

Mertens, K. N., L. R. Bradley, Y. Takano, P. J. Mudie, F. Marret, A. E. Aksu, R. N. Hiscott, T. J. Verleye, E. A. Mousing, L. L. Smyrnova, S. Bagheri, M. Mansor, V. Pospelova and K. Matsuoka (2012), Quantitative estimation of holocene surface salinity variation in the black sea using dinoflagellate cyst process length. Quaternary Science Reviews 39, 45–59. URL `http://dx.doi.org/10.1016/j.quascirev.2012.01.026`.

Mikolajewicz, U. (2011), Modeling mediterranean ocean climate of the last glacial maximum. Climate of the Past 7, 161–180.

Myers, P. G. (2002), Flux-forced simulations of the paleocirculation of the mediterranean 17, 1–7.

Myers, P. G. and E. J. Rohling (2000), Modeling a 200-yr interruption of the holocene sapropel s1. Quaternary Research 53, 98–104.

Myers, P. G., K. Haines and E. J. Rohling (1998), Modeling the paleocirculation of the mediterranean: The last glacial maximum and the holocene with emphasis on the formation of sapropel s1. Paleoceanography 13, 586–606.

on Oceanographic Tables, J. P. (1986), Progress on oceanographic tables and standards, 1983-1986: work and recommendations of the Unesco/SCOR/ICES/IAPSO Joint Panel. No. 50 in UNESCO Tech. Pap. Mar., Unesco.

Oppo, D. W., L. D. Keigwin, J. F. McManus and J. L. Cullen (2001), Persistent suborbital climate variability in marine isotope stage 5 and termination ii. Paleoceanography 16, 280–292.

Oppo, D. W., J. F. McManus and J. L. Cullen (2006), Evolution and demise of the last interglacial warmth in the subpolar north atlantic. Quaternary Science Reviews 25, 3268–3277.

Pearson, K. (1897), On a form of spurious correlation which may arise when indices are used in the measurement of organs. Mathmatical contributions to the theory of evolution 60, 489–498.

Pinardi, N., M. Zavatarelli, M. Adani, G. Coppini, C. Fratianni, P. Oddo, S. Simoncelli, M. Tonani, V. Lyubartsev, S. Dobricic and A. Bonaduce (2015), Mediterranean sea large-scale low-frequency ocean variability and water mass formation rates from 1987 to 2007: A retrospective analysis. Progress in Oceanography 132, 318–332.

Piper, D. Z. (2016), Geochemistry of the black sea during the last 15 kyr: A protracted evolution of its hydrography and ecology. Paleoceanography 31, 1117–1137.

Powley, H. R., M. D. Krom and P. Van Cappellen (2016), Circulation and oxygen cycling in the mediterranean sea: Sensitivity to future climate change. Journal of Geophysical Research: Oceans 121, 8230–8247.

Raicich, F. (1996), On the fresh water balance of the adriatic sea. Journal of Marine Systems 9, 305–319.

Rodríguez-Sanz, L., S. M. Bernasconi, G. Marino, D. Heslop, I. A. Mueller, A. Fernandez, K. M. Grant and E. J. Rohling (2017a), Penultimate deglacial warming across the mediterranean sea revealed by clumped isotopes in foraminifera. Scientific Reports 7, 1–11.

Rodríguez-Sanz, L., S. M. Bernasconi, G. Marino, D. Heslop, I. A. Mueller, A. Fernandez, K. M. Grant and E. J. Rohling (2017b), Penultimate deglacial warming across the mediterranean sea revealed by clumped isotopes in foraminifera. Scientific reports 7, 1–11.

Roether, W., B. B. Manca, B. Klein, D. Bregant, D. Georgopoulos, V. Beitzel, V. Kovačević and A. Luchetta (1996), Recent changes in eastern mediterranean deep waters. Science 271, 333–335.

Rogerson, M., E. J. Rohling, P. P. Weaver and J. W. Murray (2005), Glacial to interglacial changes in the settling depth of the mediterranean outflow plume. Paleoceanography 20, 1–12.

Rohling, E. J. (1994), Review and new aspects concerning the formation of eastern mediterranean sapropels. Marine Geology 122, 1–28.

Rohling, E. J. (1999), Environmental control on mediterranean salinity and δ18o. Paleoceanography 14, 706–715.

Rohling, E. J. and W. W. Gieskes (1989), Late quaternary changes in mediterranean intermediate water density and formation rate. Paleoceanography and Paleoclimatology 4, 531–545.

Rohling, E. J., T. R. Cane, S. Cooke, M. Sprovieri, I. Bouloubassi, K. C. Emeis, R. Schiebel, D. Kroon, F. J. Jorissen, A. Lorre and A. E. Kemp (2002), African monsoon variability during the previous interglacial maximum. Earth and Planetary Science Letters 202, 61–75.

Rohling, E. J., M. Sprovieri, T. Cane, J. S. Casford, S. Cooke, I. Bouloubassi, K. C. Emeis, R. Schiebel, M. Rogerson, A. Hayes, F. J. Jorissen and D. Kroon (2004), Reconstructing past planktic foraminiferal habitats using stable isotope data: A case history for mediterranean sapropel s5. Marine Micropaleontology 50, 89–123.

Rohling, E. J., E. C. Hopmans and J. S. S. Damsté (2006), Water column dynamics during the last interglacial anoxic event in the mediterranean (sapropel s5). Paleoceanography 21, 1–8.

Rohling, E. J., G. Marino and K. M. Grant (2015), Mediterranean climate and oceanography, and the periodic development of anoxic events (sapropels). Earth-Science Reviews 143, 62–97. URL `http://dx.doi.org/10.1016/j.earscirev.2015.01.008`.

Romanou, A., G. Tselioudis, C. S. Zerefos, C. A. Clayson, J. A. Curry and A. Andersson (2010), Evaporation-precipitation variability over the mediterranean and the black seas from satellite and reanalysis estimates. Journal of Climate 23, 5268–5287.

Rossignol-Strick, M. (1985), Mediterranean quaternary sapropels, an immediate response of the african monsoon to variation of insolation. Palaeogeography, Palaeoclimatology, Palaeoecology 49, 237–263.

Rossignol-Strick, M., W. Nesteroff, P. Olive and C. Vergnaud-Grazzini (1982), After the deluge: Mediterranean stagnation and sapropel formation. Nature 295, 105–110.

Ruzmaikin, A., J. Feynman and Y. L. Yung (2006), Is solar variability reflected in the nile river? Journal of Geophysical Research Atmospheres 111, 1–8.

Ryan, W. B., W. C. Pitman, C. O. Major, K. Shimkus, V. Moskalenko, G. A. Jones, P. Dimitrov, N. Gorür, M. Sakinç and H. Yüce (1997), An abrupt drowning of the black sea shelf. Marine Geology 138, 119–126.

Sampieri, R. H. (2002), Climate Development and History of the North Atlantic Realm. Springer Berlin Heidelberg. URL `http://link.springer.com/10.1007/978-3-662-04965-5`.

Schiffelbein, P. and L. Dorman (1986), Spectral effects of time-depth nonlinearities in deep sea sediment records: A demodulation technique for realigning time and depth scales. Journal of Geophysical Research: Solid Earth 91, 3821–3835.

Schroeder, K., J. Garcìa-Lafuente, S. A. Josey, V. Artale, B. B. Nardelli, A. Carrillo, M. Gačić, G. P. Gasparini, M. Herrmann, P. Lionello, W. Ludwig, C. Millot, E. Özsoy, G. Pisacane, J. C. Sánchez-Garrido, G. Sannino, R. Santoleri, S. Somot, M. Struglia, E. Stanev, I. Taupier-Letage, M. N. Tsimplis, M. Vargas-Yáñez, V. Zervakis and G. Zodiatis (2012), Circulation of the mediterranean sea and its variability. Elsevier.

Schönfeld, J. (2002), A new benthic foraminiferal proxy for near-bottom current velocities in the gulf of cadiz, northeastern atlantic ocean. Deep-Sea Research Part I: Oceanographic Research Papers 49, 1853–1875.

Schönfeld, J. and R. Zahn (2000), Late glacial to holocene history of the mediterranean outflow. evidence from benthic foraminiferal assemblages and stable isotopes at the portuguese margin. Palaeogeography, Palaeoclimatology, Palaeoecology 159, 85–111.

Scott, C. and T. W. Lyons (2012), Contrasting molybdenum cycling and isotopic properties in euxinic versus non-euxinic sediments and sedimentary rocks: Refining the paleoproxies. Chemical Geology 324, 19–27.

Scrivner, A. E., D. Vance and E. J. Rohling (2004), New neodymium isotope data quantify nile involvement in mediterranean anoxic episodes. Geology 32, 565–568.

Sierro, F. J., D. A. Hodell, N. Andersen, L. A. Azibeiro, F. J. Jimenez-Espejo, A. Bahr, J. A. Flores, B. Ausin, M. Rogerson, R. Lozano-Luz, S. M. Lebreiro and F. J. Hernandez-Molina (2020), Mediterranean overflow over the last 250 kyr: Freshwater forcing from the tropics to the ice sheets. Paleoceanography and Paleoclimatology 35, 1–31.

SILSO (2018), Sunspot data. `http://sidc.be/silso/home`, Royal Observatory of Belgium, Brussels, accessed: 01-05-2018.

Simon, H. A. (1954), Spurious correlation: A causal interpretation. Journal of the American statistical Association 49, 467–479.

Slomp, C. P. and P. Van Cappellen (2007), The global marine phosphorus cycle: Sensitivity to oceanic circulation. Biogeosciences 4, 155–171.

Slomp, C. P., J. Thomson and G. J. D. Lange (2002), Enhanced regeneration of phosphorus during formation of the most recent eastern mediterranean sapropel (s1). Geochimica et Cosmochimica Acta 66, 1171–1184.

Song, X. and L. Yu (2017), Air-sea heat flux climatologies in the mediterranean sea: Surface energy balance and its consistency with ocean heat storage. Journal of Geophysical Research: Oceans 122, 4068–4087.

Soulet, G., G. Delaygue, C. Vallet-Coulomb, M. E. Böttcher, C. Sonzogni, G. Lericolais and E. Bard (2010), Glacial hydrologic conditions in the black sea reconstructed using geochemical pore water profiles. Earth and Planetary Science Letters 296, 57–66. URL `http://dx.doi.org/10.1016/j.epsl.2010.04.045`.

Soulet, G., G. Ménot, G. Bayon, F. Rostek, E. Ponzevera, S. Toucanne, G. Lericolais and E. Bard (2013), Abrupt drainage cycles of the fennoscandian ice sheet. Proceedings of the National Academy of Sciences of the United States of America 110, 6682–6687.

Starr, A., I. Hall, S. Barker, T. Rackow, X. Zhang, S. Hemming, H. van der Lubbe, G. Knorr, M. Berke, G. Bigg, A. Cartagena, F. Jiménez-Espejo, X. Gong, J. Gruetzner, N. Lathika, L. LeVay, R. Robinson and M. Ziegler (2020), Antarctic icebergs reorganise ocean circulation during pleistocene glacials. Nature 589.

Steinhilber, F., J. A. Abreu, J. Beer, I. Brunner, M. Christl, H. Fischer, U. Heikkila, P. W. Kubik, M. Mann, K. G. McCracken, H. Miller, H. Miyahara, H. Oerter and F. Wilhelms (2012), 9,400 years of cosmic radiation and solar activity from ice cores and tree rings. Proceedings of the National Academy of Sciences 109, 5967–5971. URL `http://www.pnas.org/cgi/doi/10.1073/pnas.1118965109`.

Stratford, K., R. G. Williams and P. G. Myers (2000), Impact of the circulation on sapropel formation in the eastern mediterranean. Marine Geology 163, 41–63.

Struglia, M. V., A. Mariotti and A. Filograsso (2004), River discharge into the Mediterranean sea: Climatology and aspects of the observed variability. Journal of Climate 17, 4740–4751.

Teodoru, C. R., G. Friedl, J. Friedrich, U. Roehl, M. Sturm and B. Wehrli (2007), Spatial distribution and recent changes in carbon, nitrogen and phosphorus accumulation in sediments of the black sea. Marine chemistry 105, 52–69.

Thomson, J., D. Mercone, G. J. D. Lange and P. J. V. Santvoort (1999), Review of recent advances in the interpretation of eastern mediterranean sapropel s1 from geochemical evidence. Marine Geology 153, 77–89.

Thomson, J., I. W. Croudace and R. G. Rothwell (2006), A geochemical application of the itrax scanner to a sediment core containing eastern mediterranean sapropel units. Geological Society, London, Special Publications 267, 65–77. URL `http://sp.lyellcollection.org/lookup/doi/10.1144/GSL.SP.2006.267.01.05`.

Timmermann, A., H. Gildor, M. Schulz and E. Tziperman (2003), Coherent resonant millennial-scale climate oscillations triggered by massive meltwater pulses. Journal of Climate 16, 2569–2585.

Topper, R. P. and P. T. Meijer (2015), The precessional phase lag of messinian gypsum deposition in mediterranean marginal basins. Palaeogeography, Palaeoclimatology, Palaeoecology 417, 6–16. URL `http://dx.doi.org/10.1016/j.palaeo.2014.10.025`.

Torrence, C. and G. P. Compo (1998), A practical guide to wavelet analysis. Bulletin of the American Meteorological Society 79, 61–78.

Tribovillard, N., T. J. Algeo, T. Lyons and A. Riboulleau (2006), Trace metals as paleoredox and paleoproductivity proxies: an update. Chemical geology 232, 12–32.

Tugrul, S., T. Besiktepe and I. Salihoglu (2002), Nutrient exchange fluxes between the aegean and black seas through the marmara sea. Mediterranean Marine Science 3, 33–42.

Tzedakis, P., M. Crucifix, T. Mitsui and E. W. Wolff (2017), A simple rule to determine which insolation cycles lead to interglacials. Nature 542, 427–432.

Vadsaria, T., G. Ramstein, J.-C. Dutay, L. Li, M. Ayache and C. Richon (2019), Simulating the occurrence of the last sapropel event (s1): Mediterranean basin ocean dynamics simulations using nd isotopic composition modeling. Paleoceanography and Paleoclimatology 34, 237–251.

van Helmond, N. A., R. Hennekam, T. H. Donders, F. P. Bunnik, G. J. de Lange, H. Brinkhuis and F. Sangiorgi (2015), Marine productivity leads organic matter preservation in sapropel s1: Palynological evidence from a core east of the nile river outflow. Quaternary Science Reviews 108, 130–138. URL `http://dx.doi.org/10.1016/j.quascirev.2014.11.014`.

Van Santvoort, P., G. De Lange, J. Thomson, H. Cussen, T. Wilson, M. Krom and K. Ströhle (1996), Active post-depositional oxidation of the most recent sapropel (s1) in sediments of the eastern mediterranean sea. Geochimica et Cosmochimica Acta 60, 4007–4024.

Van Santvoort, P., G. De Lange, C. Langereis, M. Dekkers and M. Paterne (1997), Geochemical and paleomagnetic evidence for the occurrence of “missing” sapropels in eastern mediterranean sediments. Paleoceanography 12, 773–786.

Wang, P. X., B. Wang, H. Cheng, J. Fasullo, Z. Guo, T. Kiefer and Z. Liu (2017), The global monsoon across time scales: Mechanisms and outstanding issues. Earth-Science Reviews 174, 84–121.

Wang, Y., H. Cheng, R. L. Edwards, Y. He, X. Kong, Z. An, J. Wu, M. J. Kelly, C. A. Dykoski and X. Li (2005), The holocene asian monsoon: links to solar changes and north atlantic climate. Science 308, 854–857.

Wang, Y.-J., H. Cheng, R. L. Edwards, Z. An, J. Wu, C.-C. Shen and J. A. Dorale (2001), A high-resolution absolute-dated late pleistocene monsoon record from hulu cave, china. Science 294, 2345–2348.

Wegwerth, A., O. Dellwig, J. Ôme Kaiser, G. Ménot, E. Bard, L. Shumilovskikh, B. Schnetger, I. C. Kleinhanns, M. Wille and H. W. Arz (2014), Meltwater events and the mediterranean reconnection at the saalian-eemian transition in the black sea. Earth and Planetary Science Letters 404, 124–135. URL `http://dx.doi.org/10.1016/j.epsl.2014.07.030`.

WEGWERTH, A., J. KAISER, O. DELLWIG, L. S. SHUMILOVSKIKH, N. R. NOWACZYK and H. W. ARZ (2016), Northern hemisphere climate control on the environmental dynamics in the glacial black sea "lake". Quaternary Science Reviews 135, 41–53.

WELDEAB, S., K. C. EMEIS, C. HEMLEBEN, G. SCHMIEDL and H. SCHULZ (2003), Spatial productivity variations during formation of sapropels s5 and s6 in the mediterranean sea: Evidence from ba contents. Palaeogeography, Palaeoclimatology, Palaeoecology 191, 169–190.

WELTJE, G. J. and R. TJALLINGII (2008), Calibration of xrf core scanners for quantitative geochemical logging of sediment cores: Theory and application. Earth and Planetary Science Letters 274, 423–438.

WESTERHOLD, T., U. RÖHL and J. LASKAR (2012), Time scale controversy: Accurate orbital calibration of the early paleogene. Geochemistry, Geophysics, Geosystems 13, 1–19.

WESTERHOLD, T., U. RÖHL, T. FREDERICHS, S. M. BOHATY and J. C. ZACHOS (2015), Astronomical calibration of the geological timescale: Closing the middle eocene gap. Climate of the Past 11, 1181–1195.

WILKIN, R. T., M. A. ARTHUR and W. E. DEAN (1997), History of water-column anoxia in the black sea indicated by pyrite framboid size distributions. Earth and Planetary Science Letters 148, 517–525.

WU, J., K. PAHNKE, P. BÖNING, L. WU, A. MICHARD and G. J. DE LANGE (2019), Divergent mediterranean seawater circulation during holocene sapropel formation–reconstructed using nd isotopes in fish debris and foraminifera. Earth and Planetary Science Letters 511, 141–153.

WU, P. and K. HAINES (1996), Modeling the dispersal of levantine intermediate water and its role in mediterranean deep water formation. Journal of Geophysical Research C: Oceans 101, 6591–6607.

YAN, H., W. WEI, W. SOON, Z. AN, W. ZHOU, Z. LIU, Y. WANG and R. M. CARTER (2015), Dynamics of the intertropical convergence zone over the western pacific during the little ice age. Nature Geoscience 8, 315–320.

ZAHN, R., M. SARNTHEIN and H. ERLENKEUSER (1987), Benthic isotope evidence for changes of the mediterranean outflow during the late quaternary. Paleoceanography 2, 543–559.

ZERVAKIS, V., D. GEORGOPOULOS, A. P. KARAGEORGIS and A. THEOCHARIS (2004), On the response of the aegean sea to climatic variability: A review. International Journal of Climatology 24, 1845–1858.

ZIEGLER, M., T. JILBERT, G. J. DE LANGE, L. J. LOURENS and G.-J. REICHART (2008), Bromine counts from xrf scanning as an estimate of the marine organic carbon content of sediment cores. Geochemistry, Geophysics, Geosystems 9.

Özsoy, E. and Ümit Ünlüata (1997), Oceanography of the black sea: A review of some recent results. Earth-Science Reviews 42, 231–272. URL `https://www.sciencedirect.com/science/article/pii/S0012825297818594`.

About the author

Figure 6.2 Pieter during an excursion at the famous Gibliscemi section on Sicily, Italy in 2019. The layers in the background show regular alternations that represent the orbital variability discussed in this thesis.

Pieter was born on the 18th of February, 1993 in Valkenswaard, the Netherlands. He graduated from the "Voorbereidend Wetenschappelijk Onderwijs" (VWO, profiles NT and NG) at the Erasmus College, Eindhoven, The Netherlands, in 2011. He obtained a BSc degree in Earth Sciences at Utrecht University, Utrecht, The Netherlands in 2014 and a MSc degree in Earth Science in 2016, with the track Earth, Life an Climate, Also at Utrecht University. During the last year of his master he joined the Royal Netherlands Institute for Sea Research (NIOZ) for an internship and master thesis. In January 2016 he was part of the scientific crew of the RV Pelagia on cruise 64PE406, in the Eastern Mediterranean Sea, from Cyprus to Istanbul. During his time at the NIOZ he acquired programming skills in Matlab and Latex and gained lab experience with stable isotope geochemistry on foraminifera (LA-ICP-MS and solution ICP-MS) and sediment core measurements with an XRF scanner. After his time at the NIOZ, Pieter participated in the International Conference of Paleoceanography in Utrecht (ICP12), where he presented a poster and played an experimental guitar performance at the paleomusicology concert. In 2017 Pieter started a PhD position in Utrecht, which ultimately culminated into this thesis.

In his free time, Pieter makes music on synthesizers, guitar, bass and piano. He designs his own musical electronic circuits, in particular synthesizer modules and guitar effects. He likes active holidays in the mountains. Pieter is a certified chess trainer children at the chess club in Hilversum. He plays synthesizers and guitars in the psychedelic rock band "Gula" with Ilja Fase(bass and vocals), Jan Bleijenberg (guitar and vocals) and Aad Oliehoek (drums). They released their self titled debut album in August 2018 on CD, streaming services and as Digital download, which was well received by the press. They are currently finishing the production of their follow up album.

Peer-reviewed journal publications

- Dirksen, J. P., Meijer, P. (2022). A mechanism for high-frequency variability in sapropels. Marine Geology, 106812.
- Dirksen, J. P., Meijer, P. (2020). "The mechanism of sapropel formation in the Mediterranean Sea: insight from long-duration box model experiments". Climate of the Past, 16(3), 933-952.
- Dirksen, J. P., Hennekam, R., Geerken, E., Reichart, G. J. (2019). "A novel approach using time-depth distortions to assess multicentennial variability in deep- sea oxygen deficiency in the Eastern Mediterranean Sea during sapropel S5". Paleoceanography and Paleoclimatology, 34(5), 774-786.

Conference contributions

Presentations

- Dirksen, J. P., Meijer, P. (2020). "The mechanism of sapropel formation in the Mediterranean Sea: Insight from long duration box-model experiments" (EGU, online)
- Dirksen, J. P., Pit, S. M., Slomp, C.P., Meijer, P. (2019). "Transient model analysis of salinity and oxygen dynamics in the Holocene Black Sea ". (NAC, Utrecht, NL).
- Dirksen, J. P., Meijer, P. (2018). "Model analysis of sapropel formation". (NAC, Veldhoven, NL).

Posters

- Dirksen, J. P., Meijer, P. (2020). “Transient box model analysis of sapropel formation in the Mediterranean Sea” (NAC, Utrecht, NL).

- Dirksen, J. P., Meijer, P. (2019). “Transient box model analysis of sapropel formation in the Mediterranean Sea” (ICP13, Sydney, AU).

- Dirksen, J. P., Hennekam, R., Geerken, E., Reichart, G. J. (2017). “A novel approach to asses multcentennial variability in deep-sea oxygen deficiency in the Eastern Mediterranean Sea during sapropel S5”. (RCMNS, Athens, GR).

- J.P. Dirksen, E. Geerken, K. M. Grant, L. de Nooijer, E. J. Rohling, G.J. Reichart. (2016). “Application and validation of Na/Ca as a proxy for seawater salinity in the Red Sea and Mediterranean”. (ICP12, Utrecht, NL).

Cover design and photos by Pieter Dirksen.

Back cover: sunset on the Mediterranean Sea on the RV Pelagia, closing this thesis.

Utrecht University
Faculty of Geosciences
Department of Earth Sciences

ISSN 2211-4335